

# Development of drift chambers and physics simulations for the COMPASS experiment

Dissertation  
der Fakultät für Physik  
der Ludwig-Maximilians-Universität  
München

vorgelegt von  
MARTA SANS MERCE  
aus Barcelona, Spanien

Genf, den 17. Juli 2001

1. Gutachter: Prof. Dr. M. Faessler
  2. Gutachter: Prof. Dr. D. Schaile.
- Tag der mündlichen Prüfung: 15.Oktober 2001

## Summary

COMPASS is a fixed target experiment at the CERN Super Proton Synchrotron. COMPASS plans to study the composition and structure of hadrons by using hadron beams and a polarised muon beam. The main physics goal of the experiment is to measure the contributions of quarks and, in particular, of the gluon, to the spin of the nucleon using a polarised muon beam on a polarised target. The hadron programme that could be carried out in the initial stage of the experiment includes the search for glueballs and hybrids as well as a study of the electromagnetic polarizability of different hadrons. In a second stage of the experiment, high statistics studies of the production of charmed baryons and mesons and doubly charmed baryons, as well as their leptonic and semileptonic decays, will be performed.

To carry out these various physics programmes a universal detector was designed. The setup consists of two almost independent spectrometers, one for large and the other one for small angles. Each spectrometer has electromagnetic and hadronic calorimetry, tracking detectors and muon filters. The first spectrometer can also distinguish between charged pions, kaons, protons and antiprotons by means of a Ring Imaging Cherenkov (RICH) detector.

Our group was involved in the construction and tests of one of the large angle tracking detectors, the Tracking Station 2. Tracking Station 2 consists of straw tube drift chambers. The mass production of the chambers takes place in Dubna, Russia. These chambers will be situated between the first spectrometer magnet and the RICH detector. They are designed to cover the acceptance of the RICH detector. The research and development work comprised the investigation of the electrical properties of straws, the selection of the best material, the design of the components of a double layer, aging effects, rate capabilities and the readout of the straw chambers. In tests of prototypes, efficiencies of the order of 99% were measured. Average resolutions of 170  $\mu\text{m}$  for the 6 mm straws and 160  $\mu\text{m}$  for the 10 mm straws have been achieved. The results of the measurements indicate that the requirements of the COMPASS tracking can be satisfied.

In anticipation to the data, Monte Carlo simulations were performed for two special reactions of hadrons, the diffractive dissociation and the Primakoff reaction. Diffractive dissociation is one possible way of producing glueballs and hybrids. The geometrical acceptance for diffractive dissociation and for Primakoff reactions was studied and values of 22% and 65%, respectively, were obtained. A full reconstruction was performed for Primakoff events and results showed a potential accuracy three times higher than that found in previous experiments measuring the electromagnetic polarizability of the  $\pi^-$ . As different beams can be used in COMPASS, it is also possible to measure the electromagnetic polarizability of other hadrons.



## Zusammenfassung

Das COMPASS-Experiment am Super-Proton-Synchrotron des CERN wird mithilfe von polarisierten Myon-Strahlen und Hadron-Strahlen die Struktur der Hadronen erforschen. Der Schwerpunkt liegt dabei auf der Bestimmung der Spin-Strukturfunktionen des Nukleons und auf der Messung der Beiträge von Quarks und Gluonen zum Spin des Nukleons. Dazu werden ein polarisierter Myon-Strahl und ein polarisiertes Target verwendet. Das Hadron-Programm, das vor allem zu Beginn des Experiments durchgeführt werden wird, schließt die Suche nach Gluebällen und Hybridzuständen und das Studium der elektromagnetischen Polarisierbarkeit verschiedener Hadronen ein. In einer zweiten Phase des Experiments werden mit hoher Statistik die Produktion und leptonische und semileptonische Zerfälle von charm-haltigen Baryonen und Mesonen und zweifach charm-haltigen Baryonen untersucht werden.

Für dieses weitgespannte Programm wurde ein universell einsetzbarer Detektor entworfen, der aus zwei weitgehend unabhängigen Spektrometern besteht, die den Bereich kleiner beziehungsweise großer Streuwinkel abdecken. Jedes dieser Spektrometer verfügt über elektromagnetische und hadronische Kalorimeter, Spurdetektoren und Myon-Filter. Das Grosswinkel-Spektrometer kann des weiteren mithilfe eines Ring-Imaging-Cherenkov-Detektors (RICH) auch geladene Pionen, Kaonen, Protonen und Antiprotonen voneinander unterscheiden.

Die COMPASS-Gruppe der LMU München ist hauptverantwortlich für die Konstruktion und Tests von einem der Spurdetektoren, der "Tracking Station 2". Diese besteht aus Strawtube-Driftkammern, die größtenteils in Dubna, Rußland, gefertigt werden. Die Kammern haben die gleiche Akzeptanz wie der RICH-Detektor und werden zwischen diesem und dem ersten Spektrometer-Magneten installiert werden. Die Forschungs- und Entwicklungsarbeit an den Strawtube-Kammern umfaßte die Untersuchung der elektrischen Eigenschaften der Straws, die Auswahl des besten Materials, den Entwurf der Komponenten einer Doppelschicht von Strawtubes, Alterungseffekte, Ratenverträglichkeiten und Readout. In Tests von Prototypen wurden Effizienzen von 99% erreicht. Dabei wurden durchschnittliche Auflösungen von  $170\ \mu\text{m}$  für Straws mit 6 mm Durchmesser und von  $160\ \mu\text{m}$  für Straws mit 10 mm gemessen. Damit werden die an das COMPASS-Tracking gestellten Auflagen erfüllt.

In Erwartung der Daten wurden Monte Carlo-Simulationen für zwei spezielle Reaktionen von Hadronen: die diffraktive Dissoziation und die Primakoff-Reaktion durchgeführt. Diffraktive Dissoziation ist eine Möglichkeit der Erzeugung von Gluebällen und Hybridzuständen. Die Untersuchung der geometrischen Akzeptanz für die diffraktive Dissoziation und die Primakoff-Reaktion ergab Werte von 22% beziehungsweise 65%. Für Primakoff-Ereignisse wurde außerdem eine vollständige Rekonstruktion durchgeführt. Die Ergebnisse dieser Rekonstruktion zeigen, dass der statistische Fehler der elektromagnetischen Polarisierbarkeit des  $\pi^-$  um einen Faktor drei verbessert werden kann, im Vergleich zu früheren Messungen. Da für COMPASS verschiedene hadronische Strahlen benutzt werden können, wird es auch möglich sein, die elektromagnetische Polarisierbarkeit anderer Hadronen zu messen.



# Contents

<b>1</b>	<b>Introduction</b>	<b>3</b>
<b>2</b>	<b>The COMPASS experiment</b>	<b>8</b>
2.1	Physics goals of COMPASS . . . . .	8
2.1.1	Physics with the muon beam . . . . .	8
2.1.2	Physics with hadron beams . . . . .	11
2.2	The experimental setup . . . . .	13
2.2.1	Target region for the muon beam . . . . .	13
2.2.2	Target region for the hadron beams . . . . .	14
2.2.3	The tracking system . . . . .	14
2.2.4	The RICH1 detector . . . . .	15
2.2.5	The calorimeters . . . . .	15
2.2.6	The muon filters . . . . .	16
2.2.7	Triggers . . . . .	16
2.2.8	Read out electronics and DAQ . . . . .	16
<b>3</b>	<b>The tracking station 2</b>	<b>18</b>
3.1	General concepts . . . . .	18
3.1.1	Drift chambers . . . . .	18
3.1.2	Straw tube drift chambers for COMPASS . . . . .	19
3.1.3	Layout of <b>T</b> racking <b>S</b> tation <b>2</b> ( <b>TS2</b> ) . . . . .	20
3.1.4	Materials and components of TS2 . . . . .	23
3.2	R&D . . . . .	26
3.2.1	Gas . . . . .	26
3.2.2	Four straw tubes . . . . .	28
3.2.3	Read out electronics . . . . .	29
3.2.4	Electrical properties of the straws . . . . .	34
3.2.5	Aging . . . . .	35
3.2.6	Rate capability . . . . .	37
3.3	Tests of prototypes . . . . .	41
3.3.1	Design considerations for two prototypes by MSU and JINR . . . . .	42
3.3.2	Laboratory tests . . . . .	42
3.3.3	Test beam measurements . . . . .	43
3.3.4	Analysis and results . . . . .	45
3.3.5	Conclusions of the tests . . . . .	51
3.3.6	Construction of a third prototype . . . . .	51
3.3.7	Full size "prototype" double layer . . . . .	54

3.4	Final design . . . . .	55
3.4.1	Components . . . . .	55
3.4.2	Precision required . . . . .	57
3.4.3	Assembly . . . . .	59
<b>4</b>	<b>Physics simulations</b>	<b>64</b>
4.1	Diffractive dissociation . . . . .	64
4.1.1	General features of diffractive dissociation . . . . .	64
4.1.2	Study of $\pi^- A \rightarrow (\pi^- \eta) A$ in COMPASS . . . . .	66
4.2	Primakoff reaction . . . . .	72
4.2.1	General features of the Primakoff reaction . . . . .	72
4.2.2	The Primakoff cross-section . . . . .	73
4.2.3	Study of $\pi^- Z \rightarrow \pi^- Z \gamma$ in COMPASS . . . . .	73
4.3	Acceptance studies . . . . .	75
4.3.1	COMPASS detector for the initial hadron programme . . . . .	75
4.3.2	Geometrical acceptance . . . . .	78
4.4	Possible measurement of $\pi^-$ polarizability . . . . .	85
4.4.1	Steps previous to the simulation . . . . .	86
4.4.2	Complete simulation . . . . .	88
4.4.3	Selection of events . . . . .	89
4.4.4	Efficiency measurements . . . . .	92
4.4.5	Trigger . . . . .	94
4.4.6	Estimated statistics . . . . .	95
4.4.7	Possible results in COMPASS . . . . .	96
<b>A</b>	<b>List of acronyms</b>	<b>100</b>
<b>B</b>	<b>Kinematics for inelastic diffraction at high energies</b>	<b>101</b>

# Chapter 1

## Introduction

COMPASS is a fixed target experiment at the CERN<sup>1</sup> Super Proton Synchrotron (SPS). The main goal of the experiment is to study the spin structure of nucleons with polarised muon beams (100-200 GeV/c) on polarized nucleon targets. In addition, the production and decay of "heavy" baryons and mesons containing charm quarks and of "exotic" light mesons called "glueballs" and "hybrids", will be investigated with hadron beams (up to 300 GeV/c).

The main physics objective of the muon beam programme is the measurement of  $\Delta G/G$ , the longitudinal gluon polarisation in a longitudinally polarised nucleon. In the sixties, the existence of the quarks in the nucleon was discovered through deep inelastic scattering of leptons on nucleons. After 40 years of these experiments, there is still no clear knowledge of the spin structure of proton and neutron. After the confirmation of the result of the EMC experiment by recent experiments at CERN and SLAC, it is now clearly established that only a small fraction of the spin is carried by the quarks. This result could be explained in different ways. In one model, it is the polarised glue which lowers the quark's contribution to the nucleon spin, whereas in an alternative model negatively polarised strange quarks are responsible. For the measurement of the gluon polarisation  $\Delta G/G$ , COMPASS will use the photon gluon fusion leading to open charm production (see figure 1.1). In such a process, the muon emits a virtual photon which interacts with one gluon from the proton target producing a  $c\bar{c}$  pair. Therefore the detection of high statistics samples of charmed particles is a key feature of the experiment. This imposes the use of very-high intensity muon beams. Two other experiments, HERMES at HERA-DESY and pp2pp at RHIC, Brookhaven, are also aiming to measure  $\Delta G/G$  by means of other reactions.

The detection of charmed particles is not only of great importance for COMPASS's muon programme, but also for its hadron programme. Using hadron beams, it will be possible to study the semi-leptonic decays of charmed-baryons as well as doubly charmed baryons. Semi-leptonic decays of charm-particles will allow tests of Heavy Quark Effective Theory (HQET) calculations since they predict precise rates and form-factors. In order to obtain clean charm samples, one possibility is to require the full or partial reconstruction of an associated D or  $\bar{D}$ -meson. In order to collect large samples of a few  $10^6$  events with reconstructed D-mesons, high intensity beams of up to  $5 \times 10^7$  hadrons/sec are required. The topic of doubly charmed hadrons has not yet been addressed by any currently operating experiment. These particles are constituted by a heavy cc-diquark surrounded by

---

<sup>1</sup>European Organization for Nuclear Research in Geneva

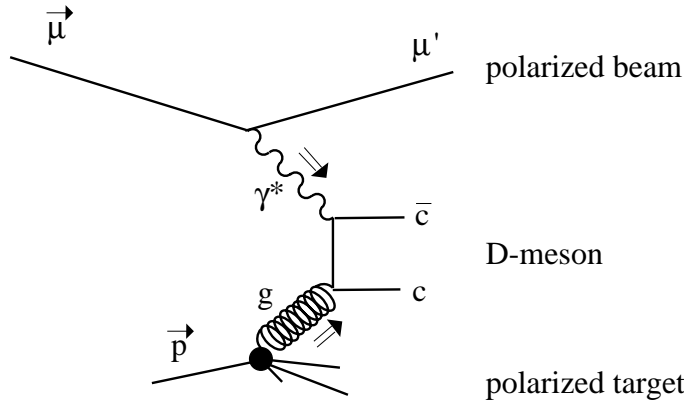


Figure 1.1: The photon-gluon fusion diagram for  $c\bar{c}$  production.

a light quark. Because of the very low cross section and small branching ratios of such systems, a high rate experiment is required. For this purpose, COMPASS will use a proton beam of  $5 \times 10^7$  particles/s. The charm programme will be performed in a second stage of the experiment, since a highly segmented silicon target detector is needed.

Other physics topics will be covered when using the hadron beams. In meson spectroscopy, a key topic is the prediction of the existence of new classes of non- $q\bar{q}$  systems, such as glueballs (states of two or three gluons) and hybrids ( $q\bar{q}g$ ). For many years much effort has been spent in proving the existence of glueballs and hybrids, with the best candidates coming from LEAR<sup>2</sup>. To obtain a gluon rich environment, two production mechanisms are considered: central production and diffractive scattering of mesons by nuclei. As a further topic, the electromagnetic polarizabilities of different hadrons can be studied by the Primakoff reaction, which can be understood as Compton scattering of the incoming hadron with virtual photons in the Coulomb field of a high  $Z$  nucleus.

The COMPASS detector is a modern high rate spectrometer with two almost independent magnetic spectrometer stages (the acronym COMPASS stands for **CO**mmun **MU**on and **P**roton **A**pparatus for **S**tructure and **S**pectroscopy). Despite the different requirements for the various physics topics, a large fraction of the apparatus will be common for all physics programmes. This applies in particular for the detectors situated downstream of the first spectrometer.

The requirement of the various detectors are given by the maximum requirements of the different physics measurements. As high rates are expected (in the order of 100 MHz for the muon beam intensity and 1 MHz for the interaction rate in the hadron beam), the detector materials were chosen with particular care, so as to minimize damage from radiation. These high rates demand high speed detector read out and therefore fast front end electronics, multi-buffering and a large and fast storage of events. This challenging task requires the use of LHC-type technology. The spectrometer consists of a large and a small angle spectrometer stage. The design of the two stages is similar. Each stage includes a beam spectrometer magnet SM1/2, a Cherenkov counter RICH1/2, an electromagnetic calorimeter ECAL1/2, a hadronic calorimeter HCAL1/2 and a muon filter  $\mu$ F1/2 (the large angle spectrometer is indicated by 1, and the small angle spectrometer is indicated by 2). RICH2 and ECAL1 will not be available at the beginning of the COMPASS programme. The RICH1 is designed to distinguish between pions and kaons in a

<sup>2</sup>Low Energy Antiproton Ring at CERN

momentum range from 3 to 65 GeV/c. The electromagnetic calorimeters will be made of lead glass, except for the central region of ECAL2 which will consist of "radiation hard"  $\text{PbWO}_4$ . The first hadronic calorimeter requires a very high resolution while the second one is mainly for triggering purposes. The muon filters are for the identification and detection of the scattered muon in the muon programme and in the hadron programme for the identification and detection of muons from semi-leptonic decays. For the small area tracking, gas microstrip detectors like GEMs (**G**as **E**lectron **M**ultiplier) and micromegas gas detectors will be used together with scintillating fibres. For the hadron programme, silicon detectors will be added before and after the target. For the large area tracking, classical drift chambers and MWPCs (**M**ulti **W**ire **P**roportional **C**hambers) will be used. Classic wire drift chambers will be situated between the target and the first spectrometer magnet. After the first spectrometer magnet and before the RICH1 detector, a set of straw drift chambers called Tracking Station 2 (TS2) will be placed. MWPCs are situated all along the apparatus.

The responsibility for the coordination of the development, design, tests and operation of TS2 was given to our group. Two groups in COMPASS, JINR-Dubna and Moscow State University, have had the experience in building straw drift chambers. Each of these two institutes built a prototype. Tests were performed at CERN to determine the properties of the two chamber prototypes with 6 and 10 mm straw diameters. Efficiencies of 99% for both straw diameters and average resolutions of 160  $\mu\text{m}$  and 170  $\mu\text{m}$ , for the 10 and 6 mm diameter straws respectively, were obtained. In general it was found that the straw chambers will fulfil the requirements of high efficiency and high resolution for the COMPASS large area tracking detectors. A third prototype was constructed to test different ideas on the design and construction of a large straw chamber.

The Warsaw Technical University and Freiburg University were also involved in the project, developing the mother board and the front end read out card. The read out system for these detectors was also studied in the different tests performed with the prototypes. Extensive Research and Development (R&D) was carried out by Munich, Warsaw Technical University and Freiburg University. In particular these teams determined the electrical properties of different types of straws, the materials best suited for the components of the chambers, the aging effects and the rate capabilities of a double layer. Other tests were also performed to determine the working conditions of the chambers. After all the tests and R&D had been performed, the design of the final chambers could be determined. A double layer, made following the design of a final chamber, was delivered at CERN in October 2000. Further tests were performed with this double layer to check the uniformity of the efficiency and resolution for different straws. This information indicates the uniformity of calibration for the final chambers. To determine the internal precision of a double layer, an X-ray setup was constructed by our group. Using an X-ray source and a CCD camera, the precision of every wire with respect to the rest can be determined. The assembly method for the final chambers was mainly developed by JINR-Dubna. TS2 will consist of 18 double layers distributed as follows: 6 double layers with vertical straws to measure the horizontal coordinate, 6 with horizontal straws to measure the vertical coordinate and 6 with inclined straws to distinguish the real tracks from the ghost tracks. The chambers have an area of  $3250 \times 2720 \text{ mm}^2$  so as to cover the acceptance of the RICH1 detector. A double layer is made by two layers of straw tubes, with each layer shifted by half a diameter with respect to the other so as to cover the less efficient regions of the straw and to resolve most of the left-right ambiguity in a single straw. Two different

straw diameters will be used. The inner region of the chamber will be constituted of 6 mm diameter straws to measure the high rates close to the beam. The outer regions of the chambers will be constituted of 10 mm straws.

In parallel to the work on TS2, our group was involved in the preparation of an "initial physics programme" using hadron beams. Single diffractive dissociation is a process where one particle scatters elastically but the second particle scatters inelastically. The particle exchanged is called Pomeron. The nature of the Pomeron is not yet known but it is likely to be a gluonic object as only momentum and angular momentum is exchanged. Thus diffractive dissociation has been chosen to provide a gluon rich environment favourable to produce glueballs and hybrids. A suitable simple reaction for an initial reduced setup is the following diffractive reaction:  $\pi^- p \rightarrow p \pi^- \eta$ , where the  $\eta$  then decays into two gammas, and the intermediate resonance  $X$  is the object of interest (see figure 1.2).

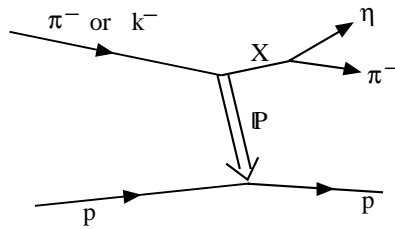


Figure 1.2: Single diffractive dissociation of the projectile.

To generate this kind of events a special event generator was developed according to a theoretical model. The geometrical acceptance of the diffractive events in the COMPASS detector was studied. Events having in the final state one  $p$ , one  $\pi^-$ , and 2  $\gamma$  are selected. The characteristic kinematics for the diffractive process is, in this case, an isolated slow proton in the target fragmentation region and a four momentum transfer squared  $t$  not larger than  $1 \text{ GeV}^2$ . An event is accepted when the  $\pi^-$  is detected in at least one of the tracking detectors in each of at least two of the zones of the spectrometer (between the target and the first spectrometer magnet, between the first spectrometer magnet and the second one, and between the second one and the electromagnetic calorimeter) and the two gammas are detected in the electromagnetic calorimeter located 32 m from the target. From the produced events, 22% of the events were accepted.

The same studies were performed for the Primakoff reaction, where the incoming particle ( $\pi^-$  in our case) scatters in the Coulomb field of a nucleus via a virtual photon. A  $\pi^-$  and a real  $\gamma$  are emitted as a result (see figure 1.3).

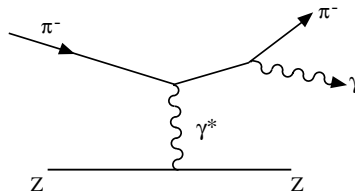


Figure 1.3: Primakoff reaction.

The differential cross section differs from that of the Coulomb scattering of a point like particle because of the electromagnetic polarizability of the  $\pi^-$ . An existing event

generator was used to provide the particles in the desired final state with the characteristic kinematics of the Primakoff events. A very low four momentum transfer squared  $t$ , typically smaller than  $0.02 \text{ GeV}^2$ , is characteristic for the Primakoff reaction. The requirements for the acceptance of these events are similar to the ones of diffractive events, the only difference being that only one gamma is in the final state. From the produced Primakoff events, 65% were accepted. This acceptance is larger than in the diffractive process because only one gamma is present in the final state.

The geometrical acceptance is not enough to determine whether it is possible to measure such a physics reaction in COMPASS. To determine the feasibility of the Primakoff measurement, the probability of the reconstruction of such an event should be determined. The first requirement to select the event is that only two particles are in the final state, a  $\pi^-$  and a  $\gamma$ . The sum of the energies of the two particles should be the energy of the beam. Another requirement is on the value of the four momentum transfer squared  $t$  ( $t < 0.02 \text{ GeV}^2$ ). Once the event is selected, the efficiency distribution is measured as a function of  $t$ . The result that the efficiency does not depend strongly on  $t$ , indicates that cutting on  $t$  will not introduce any bias in the results. The conclusion is that COMPASS can measure the  $\pi^-$  polarizability with three times higher precision than the previous Serpukhov experiment. Profiting from the fact that different beam particles can be used in COMPASS the polarizabilities of all these particles can be studied.

This thesis is divided in three parts. The first chapter of this thesis describes in more detail the physics goals of COMPASS, its detector as well as the trigger and read out electronics used. In the second chapter an overview of the design considerations of TS2 and the research and development work performed is given. The last chapter describes the simulation studies performed to check the feasibility of two of the reactions of the "initial hadron physics programmes" in COMPASS.

# Chapter 2

## The COMPASS experiment

COMPASS, which stands for **CO**mmun **MU**on and **PR**oton **AP**paratus for **ST**ructure and **SP**ectroscopy, is a fixed target experiment at the CERN SPS. Its goal is to investigate hadron structure and hadron spectroscopy by using either muon or hadron beams. Using polarized muons on a polarized target, the open charm production will allow the determination of the gluon polarization inside the nucleon and help to understand the spin structure of the nucleon. The main objective of the initial hadron programme is the search for exotic states, glueballs in particular. The merging of the hadron and muon programmes which were in the beginning separate projects, came from the fact that both aimed at the detection of charmed mesons. Thus the same detector could be used for both programmes. These physics programmes will be carried out with a new two-stage magnetic spectrometer, with calorimetry in both stages and particle identification in the first stage. COMPASS is capable of withstanding beam intensities up to  $2 \cdot 10^8$  particles/spill. Dedicated triggers and fast read out complement the performance of the spectrometer.

### 2.1 Physics goals of COMPASS

#### 2.1.1 Physics with the muon beam

##### The gluon polarization

The gluons carry 50% of the linear momentum of a nucleon, but how much of the angular momentum they carry is unclear. A series of experiments in the recent years confirms the originally surprising findings of the EMC collaboration that the spin of the nucleon is not entirely due to the quark spins [3].

In general terms, one writes the spin equation for the proton (or neutron) as:

$$\frac{1}{2} = \frac{1}{2}\Delta\Sigma + \Delta G + \langle L_z \rangle \quad (2.1)$$

where  $\Delta\Sigma = \Delta u + \Delta d + \Delta s$  is the contribution of the quark spins,  $\Delta G$  is the contribution of the gluons, and  $\langle L_z \rangle$  is a possible contribution from the orbital angular momentum of the gluons and quarks.

$\Delta u$ ,  $\Delta d$  or  $\Delta s$  can be written in the usual notation as:

$$\Delta q_f = \int_0^1 \{(q_f(x)^{\uparrow\uparrow} + \bar{q}_f(x)^{\uparrow\uparrow}) - (q_f(x)^{\downarrow\uparrow} + \bar{q}_f(x)^{\downarrow\uparrow})\} \cdot dx = \int_0^1 \Delta q_f(x) \cdot dx \quad (2.2)$$

where  $q_f(x)^{\uparrow\uparrow}$  ( $\bar{q}_f(x)^{\uparrow\uparrow}$ ) and  $q_f(x)^{\downarrow\uparrow}$  ( $\bar{q}_f(x)^{\downarrow\uparrow}$ ) are the distribution functions of quarks (antiquarks) of flavour  $f$  with spin parallel and antiparallel to the nucleon spin.  $x$  is called the Bjorken  $x$  and can be interpreted as the fraction of momentum carried by the quark.

In the simple quark model, the three valence quarks are in an S-state, so  $\langle L_z \rangle = 0$ , and the spin sum-rule (equation 2.1) is satisfied by  $\Delta\Sigma = 1$ .

Since the EMC discovery [4], it is known that this picture does not correspond to reality since the contribution of the quarks to the spin of the nucleon is much smaller. From the result found by the EMC collaboration ( $\Delta\Sigma = .19 \pm 0.07$ ) [61], the idea arose that a large fraction of the proton spin is carried by the gluons.

To measure the polarized gluon distribution  $\Delta G$ , the photon-gluon fusion process leading to open charm production will be used (Fig. 2.1).

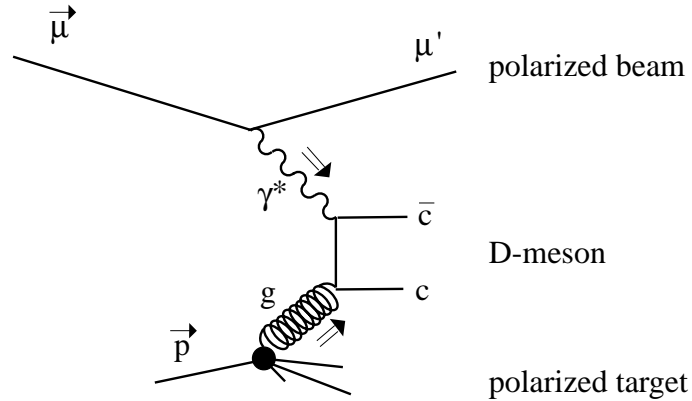


Figure 2.1: The photon-gluon fusion diagram for  $c\bar{c}$  production.

$\Delta G/G$  will be determined from a measurement of the cross-section asymmetry in the inclusive production of charmed particles in DIS (deep inelastic scattering) of longitudinally polarized muons on longitudinally polarized proton and deuteron targets. The measurement is based on the reconstruction of D-mesons from their hadronic decay products. The experiment will measure the spin dependent asymmetry:

$$A^{exp} = \frac{N_{c\bar{c}}^{\downarrow\uparrow} - N_{c\bar{c}}^{\uparrow\uparrow}}{N_{c\bar{c}}^{\downarrow\uparrow} + N_{c\bar{c}}^{\uparrow\uparrow}} = P_B \cdot P_T \cdot f \cdot A_{\mu N}^{c\bar{c}}(y) \quad (2.3)$$

$N_{c\bar{c}}$  is the number of charm production events with antiparallel ( $\downarrow\uparrow$ ) and parallel ( $\uparrow\uparrow$ ) longitudinal polarization of the muon and the target nucleon.  $P_B$  and  $P_T$  are the beam and target polarizations and  $f$  is the fraction of polarizable nucleons in the target material. The asymmetry  $A_{\mu N}$  is related to the virtual-photon asymmetry  $A_{\gamma N}$  by the depolarization  $D$  of the virtual photon with respect to the muon

$$A_{\mu N}^{c\bar{c}} = D \cdot A_{\gamma N}^{c\bar{c}} \quad (2.4)$$

The depolarization  $D$  of the virtual photon with respect to the muon can be expressed as:

$$D(y) = \frac{[1 - (1 - y)^2]}{[1 + (1 - y)^2]} \quad (2.5)$$

where  $y$  is the fraction of the muon energy taken by the photon.

The virtual photon asymmetry  $A_{\gamma N}$  can be expressed as:

$$A_{\gamma N}^{c\bar{c}}(E, y) = \frac{\Delta\sigma^{\gamma N \rightarrow c\bar{c}}}{\sigma^{\gamma N \rightarrow c\bar{c}}} = \frac{\int_{4 \cdot m_c^2}^{2 \cdot M_N \cdot E \cdot y} ds \cdot \Delta\sigma_{\gamma g}(s) \cdot \Delta G(\eta, s)}{\int_{4 \cdot m_c^2}^{2 \cdot M_N \cdot E \cdot y} ds \cdot \sigma_{\gamma g}(s) \cdot G(\eta, s)} \quad (2.6)$$

where  $E$  is the muon energy and  $y = \nu/E$ , with  $\nu$  being the photon energy.  $\sigma$  is the cross-section of the process  $\gamma g \rightarrow c\bar{c}$  and  $\Delta\sigma = \sigma_{\gamma g}^{\uparrow\uparrow} - \sigma_{\gamma g}^{\uparrow\downarrow}$  is the difference of the cross-sections from the reaction channel  $\gamma g \rightarrow c\bar{c}$  from parallel and antiparallel photon and gluon spins respectively.  $s = (q + k)^2$  is the invariant mass of the photon-gluon system,  $q$  and  $k$  the photon and gluon 4-momenta and  $\eta = \frac{s}{2 \cdot M_N \cdot E \cdot y}$  the gluon momentum fraction.  $G^{\uparrow\uparrow}(\eta, s)$  is the differential probability that a gluon with the same polarization (or opposite polarization  $G^{\uparrow\downarrow}(\eta, s)$ ) as the nucleon carries a momentum fraction  $\eta$ .  $\Delta G(\eta, s)$  is the difference of these differential probabilities,  $\Delta G(\eta, s) = G^{\uparrow\uparrow}(\eta, s) - G^{\uparrow\downarrow}(\eta, s)$ . From the formula 2.6 it can be seen how the virtual photon asymmetry is linked to the gluon distributions  $\Delta G$  and  $G$ .

Another way to measure  $\Delta G/G$  can be considered [7]. A signature for the photon gluon fusion could be the production of light  $q\bar{q}$  pairs with high transverse momentum, high  $p_T$ . The measurement will be done by looking for two correlated high- $p_T$  hadrons,  $h_1$  and  $h_2$ , in the forward hemisphere with  $p_T(h_{1/2})$  larger than a threshold. A threshold of 1.0 – 1.5 GeV/c is found to be sufficient to discard the lowest order diagram for deep inelastic scattering of  $\gamma^*$  nucleon, the virtual photon absorption, and to have a signature of the photon-gluon process with a background from gluon radiation processes.

The diagram in this case is given in figure 2.2.

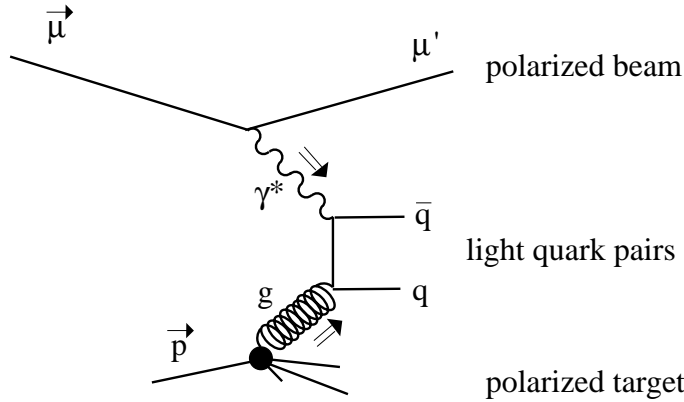


Figure 2.2: The photon-gluon fusion diagram for  $q\bar{q}$  production.

### The strange quark content of the nucleon

The existence of strange quark-antiquark pairs in the nucleon as seen by deep inelastic lepton-nucleon scattering could be explained in the framework of the polarized intrinsic strangeness model [10]. COMPASS will provide the unique opportunity to determine if the proton contains a sizeable amount of  $s\bar{s}$  quarks polarized opposite to the nucleon spin. To do so, the longitudinal polarization of  $\Lambda$  and  $\bar{\Lambda}$  baryons produced in a deep-inelastic scattering process has to be measured.

The intrinsic strangeness model is used to make predictions for the  $\Lambda$  polarization in the target fragmentation region in deep-inelastic  $\mu$  nucleon and  $e$  nucleon collisions [9]. As for the previous process (the gluon polarization model) the polarized  $\mu$  or  $e$  beam emits a virtual photon with non-zero longitudinal polarization. This strikes one quark (antiquark) polarization state inside the nucleon. In this model, the fragment left behind will still have some memory of the spin that was removed. This may be transferred to the final state in the target fragmentation region.

For example (see figure 2.3.a), a positively polarized  $u$ -quark with respect to the polarization of the nucleon, would leave behind a negatively polarized  $s\bar{s}$  pair (in the scope of the intrinsic strangeness model). This would lead to a negative polarization of the  $\Lambda$  produced in the target fragmentation region [5]. All polarizations are considered negative or positive with respect to the nucleon polarization. For the polarized-gluon model, if the strange quark in the  $\Lambda$  is produced from a polarized gluon, assuming the gluon has the same polarization as the proton (which agrees with what is expected), a positive polarization of the  $\Lambda$ 's with respect to the nucleon would be observed (Fig. 2.3.b).

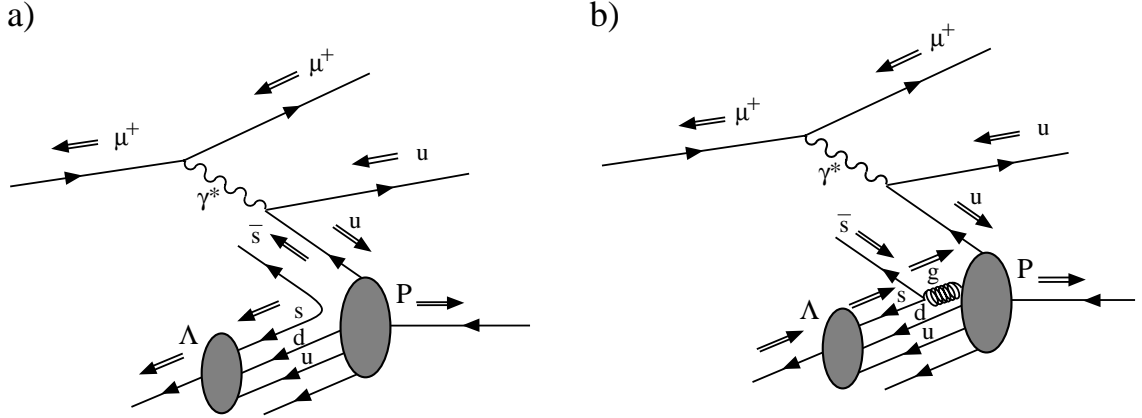


Figure 2.3:  $\Lambda$  polarization arising from a) polarized strange quarks, b) polarized gluons. The thicker arrows represent the spins of the particles.

### 2.1.2 Physics with hadron beams

#### Studies of charmed hadrons

Hadroproduction of charmed particles can be subdivided into two different subprocesses, the production of charmed quarks, and their hadronisation into charmed particles. The cross-section for the production of charmed quarks can be estimated in perturbative QCD. The hadronisation of the charm quarks into charmed particles is responsible for the production of the different types of charmed particles and their kinematical distributions.

Semi-leptonic decay widths of charmed particles will allow tests of HQET (Heavy Quark Effective Theory) calculations since they predict precise rates and form factors.

Doubly charmed baryons have never been observed so far. Their structure is unique: a heavy  $cc$  diquark together with a light quark. The very low production cross-section for these doubly charmed baryons requires an extremely high-rate experiment. COMPASS will use up to  $5 \cdot 10^7$  protons per second [1].

### Primakoff Physics

COMPASS plans to measure the scattering of beam particles from a high- $Z$  nucleus accompanied by the emission of photons ( $\text{hadron} + Z \rightarrow \text{hadron} + Z + \gamma$ ), see figure 2.4. The incoming hadron undergoes Compton scattering from a virtual photon in the Coulomb field of the nucleus, and the final  $\gamma$  and the hadron are detected in coincidence.

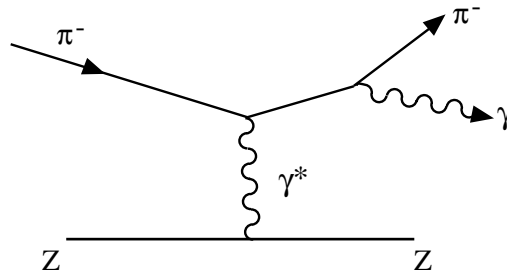


Figure 2.4: Pion radiative scattering in the Coulomb field of a nucleus

The cross-section for Compton scattering on composite systems like mesons has to be modified relative to that for point-like particles to account for their internal structure. These additional terms depend on the magnetic and electric polarizabilities which are precisely predicted for pions by Chiral Perturbation Theory. Low statistics data have yielded a value about three times larger than these theoretical predictions and clarification by a precise measurement is necessary. Only upper limits exist so far for the kaon polarizabilities.

### Search for exotics

Quantum Chromodynamics (QCD), the theory of the strong interactions, has been tested and confirmed by many experiments. However, one of the striking predictions of QCD is the existence of bound states of gluons, called glueballs ( $gg$ ,  $ggg$ ). Other types of hadronic matter in which gluons contribute to the overall quantum numbers, called hybrids ( $q\bar{q}g$ ), could also exist. The models predict the low lying exotic states [5] in the mass range from 1 GeV to 3 GeV. However, few experiments with reasonable acceptance have provided data with good statistics in the mass range from 2 GeV to 3 GeV. A candidate for the scalar glueball ground state  $0^{++}$  is the  $f_0$  at 1500 MeV/c first observed by the Crystal Barrel experiment [6] at LEAR, CERN. According to predictions, the other glueball states should have a mass well above 2 GeV. The COMPASS experiment will not have the limitation for the mass of the glueball of 2.4 GeV and plans to study light meson spectroscopy in the gluon-rich proton-proton central production and in diffractive pion and kaon scattering. What was learned from previous experiments is that the identification of glueballs

requires high-statistics data samples, reconstruction of final states containing both neutral and charged particles, observation of the same meson in many different channels and production of mesons in different reactions. The COMPASS detector is ideally suited to satisfy all of the above mentioned requirements.

## 2.2 The experimental setup

The COMPASS apparatus is a two-stage magnetic spectrometer (see fig. 2.5) to obtain a good momentum resolution from a few 100 MeV/c up to 150 GeV/c. Both stages will be equipped with hadronic and electromagnetic calorimeters. In the near future, the electromagnetic calorimeter of the first stage will not be available. The first stage will have a RICH1 detector for particle identification, but for the near future no RICH2 detector is foreseen in the second stage. Each of the spectrometer stages is equipped with high-precision tracking devices. For the large area tracking, the common detectors for the hadron and muon programme are the following: planar drift chambers (DC) between the target and the first spectrometer magnet, straw drift chambers behind the first magnet and MWPCs further downstream. For the small area tracking GEM detectors are used. Micromegas located between the target and the first magnet will be used in the muon programme. For the hadron programme, two silicon stations will be placed before the target and two after the target. An extra silicon station will be situated downstream of the first magnet. Scintillating fibre detectors are employed as fast beam detectors for timing and/or triggering in both programmes.

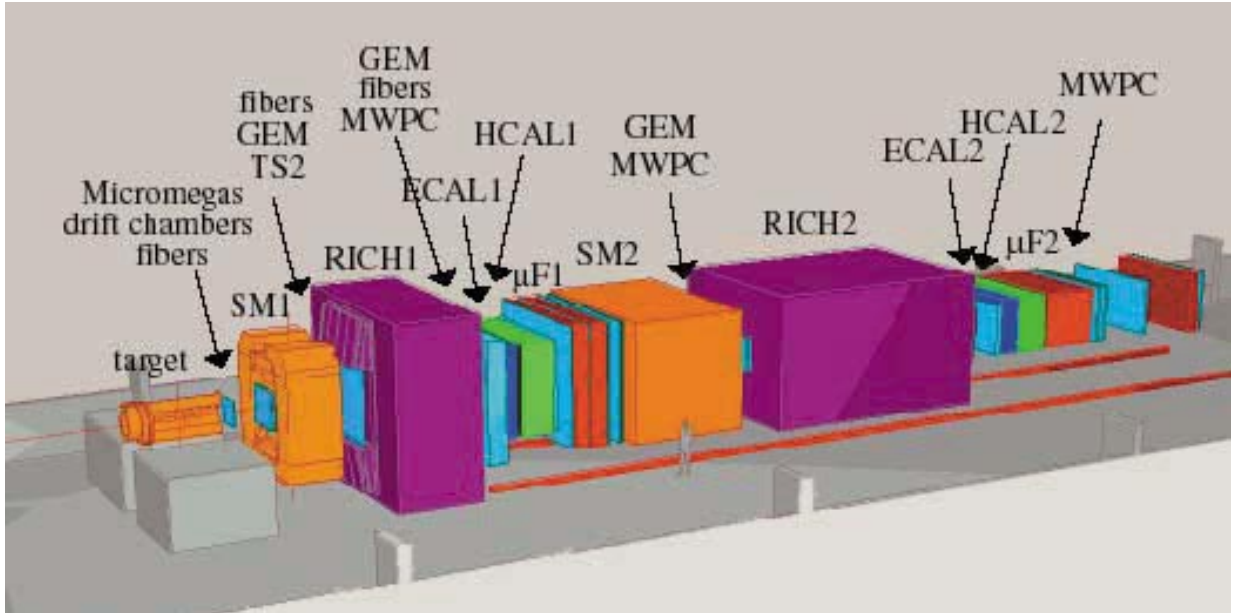


Figure 2.5: Proposal setup for the muon programme.

### 2.2.1 Target region for the muon beam

The required muon intensity is  $2 \cdot 10^8$  muons/spill for energies from 90 to 200 GeV with high longitudinal polarization. The momentum of each incoming muon is measured at the

Beam Momentum Station (BMS), which consists of four scintillator hodoscopes before and after the last dipole magnet bending the muons into the experimental hall.

Beam hodoscope telescopes will be located upstream and downstream of the polarized target. These hodoscopes should operate at a rate of  $15\text{MHz}/\text{cm}^2$  in the beam centre. For an unambiguous correlation between the information of the muon beam momentum measurement and the momentum measurement of the scattered muon, a time resolution of better than 1 ns is required. Scintillating fibre hodoscopes of 0.5 mm diameter fibres were chosen due to their high spatial and time resolution (see also section 2.2.3).

The polarized target system of the old SMC experiment, which allows for two oppositely polarized target cells, 60 cm long each, will be used. To obtain the desired hadron acceptance of  $\pm 200$  mrad, a superconducting magnet about 60 cm in diameter will be used. The magnet can provide a solenoidal field as well as a dipole field so that the target polarization can be oriented either longitudinally or transversely to the beam direction. Two different target materials will be used:  $\text{NH}_3$  as a proton target, polarized 85% and  ${}^6\text{LiD}$  as a deuteron target, polarized 50%.

### 2.2.2 Target region for the hadron beams

For the different measurements in the hadron programme, different beam particles are used. For Primakoff scattering a negative hadron beam, mainly pions with some kaon and antiproton contamination, at 280 GeV is used at  $5 \cdot 10^6$  particles per second. For central production and for the charm programme a proton beam of  $5 \cdot 10^7$  particles per second is used. When the hadron beam is used, tagging is needed to determine which species of particle is present in the mixed beam. This tagging has to be performed using fast Cherenkov counters. For this purpose a system of CEDARs [62] (CErenkov Differential counters with Achromatic Ring focus) will be used. The system has an adjustable diaphragm so that only Cherenkov angles within a small range are selected, thus allowing particles of a preselected type to be identified.

The charm target will consist of a thin copper plate closely followed by trigger counters and an array of silicon microstrip detectors. This setup allows the full reconstruction of a charm decay by measuring also a track segment of the charm hadron itself, if it was charged. This target will not be available in the initial setup. For the central production measurement, a liquid hydrogen target will be used with a recoil proton detector. The recoil proton detector consists of two rings of scintillating counters surrounding the target. For the Primakoff measurement a very high Z target, like lead, is needed. It is important to measure the angle between the incoming pion (beam) and the scattered pion. For this purpose, a set of silicon microstrip detectors are planned to be situated in the following manner: two stations in front of the target and two stations after the target. Silicon microstrip detectors were chosen because of their high spatial resolution, on the order of  $10 \mu\text{m}$ , and their capability to withstand a very high flux.

### 2.2.3 The tracking system

Very different tracking detectors will be used in COMPASS to match the expected particle flux in the various locations along the spectrometer. For the small area tracking, near the beam, where high location accuracy is needed and the particle flux is large, micromegas (for the muon programme), silicons (for the hadron programme and some for the muon

programme) and GEMs will be used. Some prototypes of micromegas and GEMs were already tested, and the spatial resolution obtained was  $50\ \mu\text{m}$  for the micromegas [8] and  $40\ \mu\text{m}$  for the GEMs [3]. The beam region itself will be covered by scintillating fiber (SciFi) hodoscopes. Fibers of different diameters are used, ranging from 0.5 mm to 1 mm. The results obtained in some tests [3] showed that they have a detection efficiency of 97% and a time resolution of better than 400 ps. For large area tracking, planar drift chambers with a small drift space (3-5 mm) will be installed between the target and the first magnet. After the first magnet there will be straw tube chambers and further downstream MWPCs. A prototype of a planar drift chamber obtained satisfactory results during tests. The resolution obtained is around  $150\ \mu\text{m}$ , and the gas mixture will be based on Argon/Ethane/ $\text{CF}_4$ . Three straw drift chamber prototypes were also tested, but this will be explained in the chapter concerning the straw chambers. The MWPCs are already available - some refurbishing will be necessary to use them in COMPASS. They have 2 mm pitch and the largest has an active area of  $1520 \times 1200\ \text{mm}^2$ .

### 2.2.4 The RICH1 detector

A clean sample of charmed mesons, which is important for the muon and the hadron programme in COMPASS, can only be obtained by unambiguously identifying pion and kaon tracks. The RICH1 has to separate  $\pi$  and K with momenta ranging from a few GeV/c up to  $\sim 60\ \text{GeV}/c$  in the entire acceptance of the large angle spectrometer, at the foreseen rates and multiplicities. Another requirement for the RICH1 detector is that it should minimise the amount of material introduced which could effect the hadron programme in COMPASS.

### 2.2.5 The calorimeters

#### The electromagnetic calorimeters

The electromagnetic calorimeter 2 will be the only electromagnetic calorimeter in the initial setup. To reconstruct the final states, which include single photons and photons from hadron decays, it is very important to have a very good photon detection efficiency. In COMPASS, the photon energy ranges from some tens of MeV to 100 GeV. It is then mandatory to have a good reconstruction of photon momentum. In case of high multiplicity events, an unambiguous photon detection is necessary and therefore the electromagnetic calorimeter should provide a good two photon separation. Since the calorimeter is operating at high rates, it should have a very fast response. A cellular lead-glass electromagnetic calorimeter with photomultiplier read out is the detector which fulfils the above requirements.

#### The hadron calorimeters

The most essential task for the first hadron calorimeter will be the detection of neutrons from the decays of charmed baryons and triggering based on this. Due to the relatively low energy of the detected particles, the position resolution is more important than the energy resolution in this calorimeter. It will consist of 25 mm thick Fe and 5 mm thick "sandwiches" of plastic scintillators. The main task of the second hadron calorimeter will

be to obtain a very good energy resolution. To provide the best possible energy resolution, the calorimeter will consist of layers of 16 mm Pb and 4 mm scintillators.

### 2.2.6 The muon filters

A large muon identifier is needed in the muon programme and in the hadron programme for muons from semileptonic decays. This detector will take advantage of the higher penetration abilities of muons compared to hadrons and will be placed behind the hadron calorimeters at each of the two stages of the spectrometer. Two different detectors will be used for these two muon filters. The first muon wall will be located upstream of the second magnet. It will consist of 1 m of iron followed by a gaseous detector made of Plastic Iarocci Tubes (PITs). The PITs will work in proportional mode to allow high rate capabilities. The second muon wall will consist of two stations. Each station will have a 1 m thick iron absorber followed by several layers of 3 cm diameter stainless steel drift tubes. Both stations will be 30 cm apart. Since drift tubes cannot follow the higher rates near the beam axis, proportional chambers will be used in that region.

### 2.2.7 Triggers

The trigger concept for the muon programme is based on the energy loss of the scattered muons. Two pairs of scintillator counter hodoscopes located about 35 and 50 m from the target and a fast matrix coincidence define in the plane scattering angle versus the total momentum the useful kinematics for the  $\Delta G/G$  measurement.

A trigger for the Primakoff reaction can be obtained by the coincidence of the energy deposition in the second electromagnetic calorimeter above the threshold with the requirement to have charged particles in the corresponding acceptance. This trigger is relatively simple and well suited for the class of Primakoff reactions, which include a measurement of the electromagnetic polarizability and of chiral anomalies. However, additional studies will be devoted to develop a more general trigger scheme, based on a beam killer and target veto counters, which could efficiently work as a minimum bias for Primakoff and diffractive type of reactions.

Since the central production (excluding simple diffractive processes) and the charm programme are not included in the initial programme of COMPASS, the trigger will not be described here.

### 2.2.8 Read out electronics and DAQ

In order to cope with the particles fluxes, the event size, and the trigger rate, a major effort has been dedicated to design front-end electronics with the shortest possible dead-time. New TDC and ADC chips were designed especially for COMPASS.

For the read out system, a modern concept involving highly specialized integrated circuits will be used. The heart of the read out system is the CATCH (Compass data Accumulation, Transfer and Control Hardware) VME module [63]. The data is sorted in the CATCH according to the event number and then is combined into sub-events. A VME interface will control and initialize the detector-mounted front-end electronics through the COMPASS detector control system (DCS, slow control).

COMPASS is designed to cope with a trigger rate of  $10^5$  Hz, and to store  $10^4$  events/sec, with a typical size of 30kB each, for a total data size of 300 TB/year. The data will be sent via an optical link from the hall directly to the Computer center for Central Data Recording (CDR). The CDR and the data crunching will be performed in a dedicated Compass Computing Farm (CCF). The CCF is a farm with a few servers to cope with the data rate and 100 to 200 PCs, CPU clients. All the PCs are "commercial" PCs running Linux as operating system. The data servers receive all the data and store them on their local disk. They are also responsible for the conversion of the data into Objectivity data base format, and the combination of the files. The CPU clients read the data from the data servers and perform preliminary analysis and tracking. In a second stage they save the results to a DST (**D**ata **S**ummary **T**ape). A Hierarchical Storage Manager (HSM) system uses the CERN central tape service. The HSM's task is to save the event data (in Objectivity format), the analysed DST, and -in the startup of the experiment- also the raw data files.

In the November 1999 tests [64], a sustained rate of 35 MB/s was achieved for the operations of transfer, conversion into Objectivity and HSM storage.

Figure 2.6 shows the scheme of the data flow on the COMPASS data acquisition.

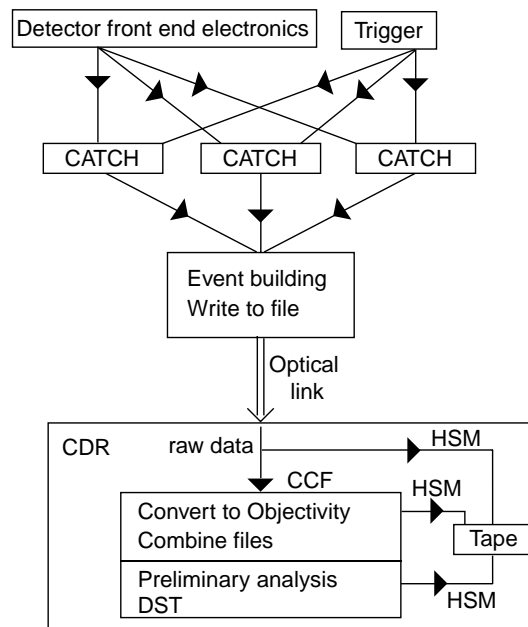


Figure 2.6: COMPASS data acquisition scheme.

# Chapter 3

## The tracking station 2

### 3.1 General concepts

#### 3.1.1 Drift chambers

When a charged particle passes through the chamber, it ionizes the medium creating a discrete number of primary electron-ion pairs [54]. The electrons resulting from the primary ionization will drift towards the anode. The ions will drift towards the cathode. For the straw chambers in COMPASS, the anode will be a wire and the cathode a thin conductive tube, the straw wall, that surrounds the wire. Close to the wire, the electrons will be accelerated due to the high electrical field. In a cylindrical counter, the field is given by [43]:

$$E(r) = \frac{C \cdot V_0}{2 \cdot \pi \cdot \epsilon} \cdot \frac{1}{r} \quad (3.1)$$

where  $C$  is the capacitance per unit of length,  $V_0$  the applied voltage,  $\epsilon$  the electric permittivity of the gas and  $r$  the distance to the wire. Near the wire, for fields of the order 200000 V/cm, or higher, the electrons get enough energy to further ionize the medium and create secondary electron-ion pairs. At this point the avalanche occurs very quickly and the signal is generated.

The straw drift chambers in COMPASS will be operated in the proportional mode. In this regime the amplitude of the signal is proportional to the number of primary ions produced. The proportionality factor is called gain.

The electrons are collected very quickly while the ions slowly drift towards the cathode. The current pulse signal on the electrodes is formed by induction due to the movement of the ions and electrons as they drift towards the cathode and anode, rather than by the collection of charges itself [43]. The signal is amplified and from the amplifier the signal is passed to a discriminator and from there to the TDC. The drift time information can be converted to distance  $r$  from the place of primary ionization to the wire by the drift velocity. The drift velocity is different for every gas. The aim is to obtain a constant drift velocity. This is not trivial due to the change of the electrical field with the distance to the wire (see equation 3.1). The dependence of  $r$  on the drift time is called the  $r(t)$  relation.

Small drift cell structures have been used in many applications in high energy physics. The straw drift tube array is one way to produce such a structure. The tube structure has some important advantages as shown in section 3.1.2.

The properties of some of the straw detectors in the world are summarised in table 3.1. Their working conditions are summarized in table 3.2 (at the end of this chapter).

### 3.1.2 Straw tube drift chambers for COMPASS

In 1997 a decision had to be made for the type of detector that will be used for the large area tracking in COMPASS. Different choices were considered. The preferred solution was to use straw tube drift chambers. The main reasons for this choice were the following:

- Very high resolution is needed in a large area.
- The straw chambers are as light as the Honeycomb or the classical drift chamber.
- When having a radial symmetry for the electrical field, the resolution is equal for tracks of different angles.
- The resolution could improve when using pressure. This could be done in a straw chamber, even though it will not be the case for the COMPASS chambers.
- In case of breakdown of one channel, only one channel is lost since it can be disconnected easily without affecting other channels.
- The rates in the area covered by the chamber will be different in different regions of the chamber. Using modular tubes, the size of the tubes can be adjusted to cope with the rates and to minimize the occupancy.
- In the COMPASS PROPOSAL [1] Honeycomb chambers were chosen since they were proposed by NIKHEF. For three different reasons the Honeycomb project was turned down and it was decided to use straw chambers. The first reason was that the NIKHEF group left COMPASS. The second reason was that in HERA-B the Honeycomb gave some problems with no obvious solution. The third reason was that in COMPASS there were two groups with experience in building straw drift chambers, one from Moscow State University and another group from the Joint Institute for Nuclear Research (JINR) in Dubna.

The requirements to be fulfilled by the straw drift chambers in COMPASS will now be exposed.

The fiducial area of **Tracking Station 2** (TS2) was determined by the acceptance of the front window of the RICH1. The size of the front window of the RICH1 detector was supposed to cover the acceptance of the first spectrometer magnet (SM1), 400 mrad vertical and 500 mrad horizontal [1]. TS2 should be confined in the space left between the SM1 and the RICH1, approximately 1 m. For tracking purposes 4 to 6 space points are required between the SM1 and the RICH1. This implies that TS2 should have 12 to 18 double layers, 4 to 6 double layers per coordinate. Therefore, the thickness of a double layer should not exceed 40 mm. The limitation on the thickness of a double layer introduced a difficulty on the chamber design. Building stable aluminium frames for a chamber of an area  $3250 \times 2720 \text{ mm}^2$  was not an easy task. The chamber frame will be nevertheless extended in the directions perpendicular to the beam. This will provide stability to the chamber and space for alignment marks and suspension holes.

Concerning the material, it was stated (see the COMPASS proposal [1]) that the thickness of TS2 should not exceed 12% radiation lengths. As it will be shown later (see table 3.4) the material introduced by the TS2 agrees with this limitation.

To carry out the  $\Delta G$  measurement in COMPASS, the mass resolution for the D meson should stay as low as possible ( $\pi K$  decay in the muon programme). A value below 10 MeV/ $c^2$  is obtained in the simulation [2] when a spatial resolution of 100  $\mu\text{m}$  is achieved in the straw chambers. It was also assumed that the error in the alignment should not be larger than the value for the resolution. For testing the spatial resolution two prototypes of straw tubes were built and tested. The tests of the prototypes will be explained in section 3.3. The alignment will be done by two successive methods. First, alignment marks will be located on the chamber to allow the geometeters to align the chambers optically. A second method using straight tracks will be employed to refine the alignment.

### 3.1.3 Layout of Tracking Station 2 (TS2)

The large area tracking station 2 (TS2) is situated between the spectrometer SM1 and RICH1 (see figure 3.1). It is one of the main parts of the COMPASS Large Area Spectrometer (**LAS**).

TS2 is made of straw drift tubes. It consists of 3 modules. Every module contains 2 sub-modules. A sub-module has 3 chambers or double layers. A double layer consists of two layers of straws oriented in the same direction. It is constructed in such a way that the second layer is shifted by half a diameter with respect to the first one. The double layer is useful to avoid left/right ambiguities. When a particle traverses a single straw, it is not known whether it passed through the left or the right side of the wire since the only information kept is the drift time to the wire. The drift time in a straw will be the same for all positions on a circle inside the straw. To eliminate this ambiguity a second layer is added shifted by one radius with respect to the first one. In this second layer, two straws cover the straw in the first layer. One covers the right side of the straw and the other the left side. It will be possible to distinguish the cases where the particle passed through the left side or the right side of the wire of the straw in the first layer, considering which straw in the second layer had a hit. TS2 will have four kinds of double layers, with vertical, horizontal and inclined wires. The angle of the inclined double layers will be  $\pm 10$  degrees with respect to the vertical wires. The inclined double layers are identical to those with vertical but rotated by the corresponding angle. To minimise dead corners, both vertical and inclined double layers will have larger surface than the horizontal double layers. The X double layer measures the x-coordinate with vertical wires. The Y double layer measures the y-coordinate with horizontal wires. The U double layer is inclined +10 degrees and the V double layer -10 degrees with respect to the vertical axis. With only one track horizontal and vertical double layers of straws will be sufficient to determine a space point for the track. With two or more tracks, an inclined double layer is needed to be able to separate the real tracks from the ghost ones. When two vertical and two horizontal neighbouring wires get a hit, it is not possible to distinguish between the two possible track candidates. In figure 3.2, not only a and d, but also c and b could be the points belonging to the track. To decide between these possibilities, the information on the drift times of the inclined wires is needed. Having small drift times will mean that points a and d correspond to the hits of the real tracks, thus indicating that points b and c are ghost hits. The minimum inclination needed for the inclined double layers to

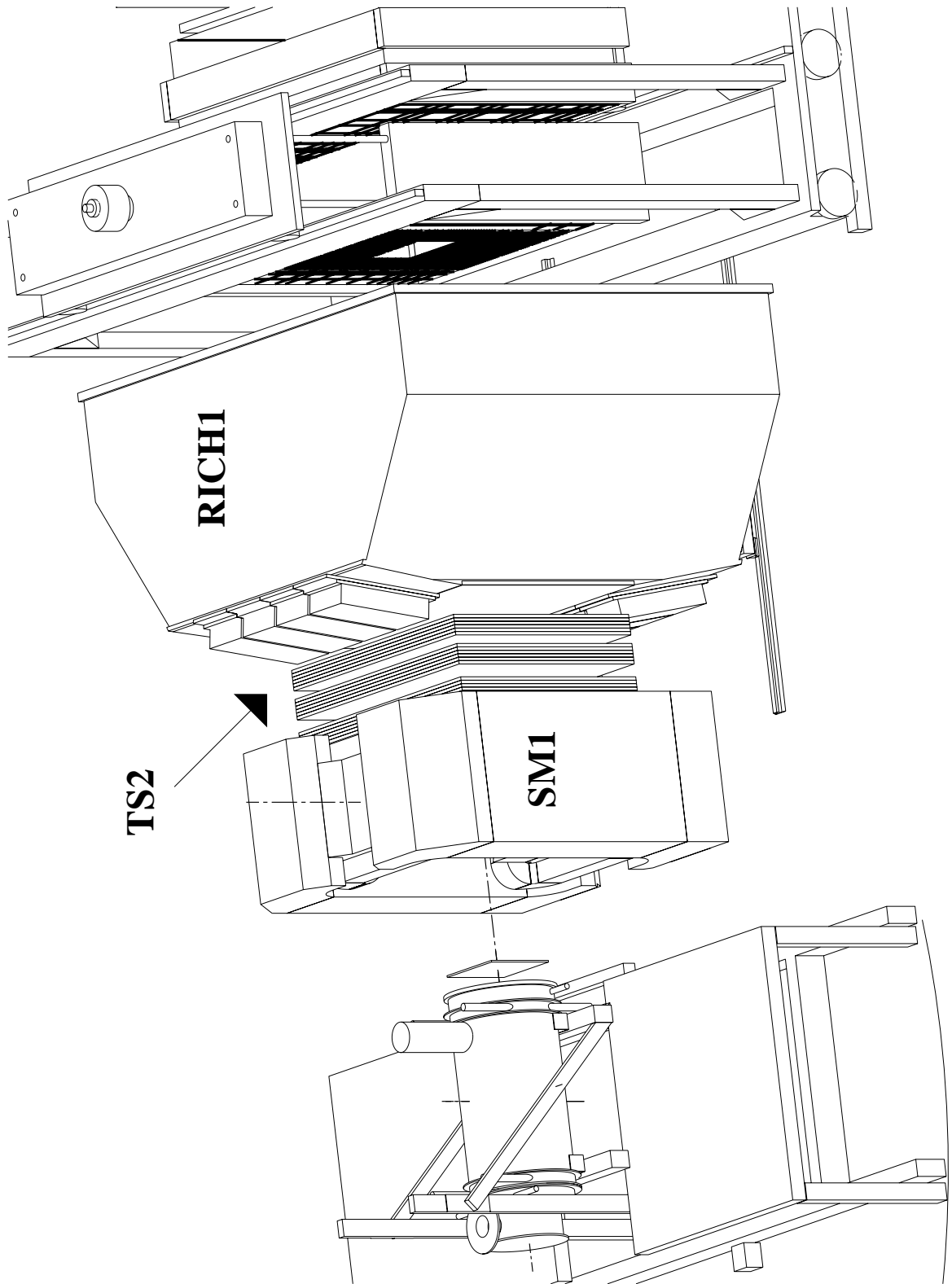


Figure 3.1: Tracking station 2 situated between SM1 and RICH1.

distinguish the real tracks from the ghost tracks is of two degrees. This was calculated assuming 6 mm straws with 200  $\mu\text{m}$  resolution.

The angle of inclination was studied and results showed [11] that the efficiency of

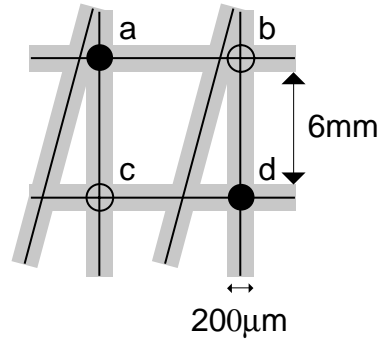


Figure 3.2: *a* and *d* are the real hits. *b* and *c* are not real hits. The black lines represent the measured coordinates and the grey areas correspond to the resolution of the straws.

reconstruction only varies by 2% for an angle in the range 5-25 degrees. A compromise of 10 degrees will be good enough to minimize the dead corners due to the chamber rotation. When having small angles, the horizontal coordinate is measured with better precision, and favour the measurement of the momentum of the particles, since the magnetic field deflects them in the horizontal plane.

Figure 3.3 shows an schematic layout of TS2.

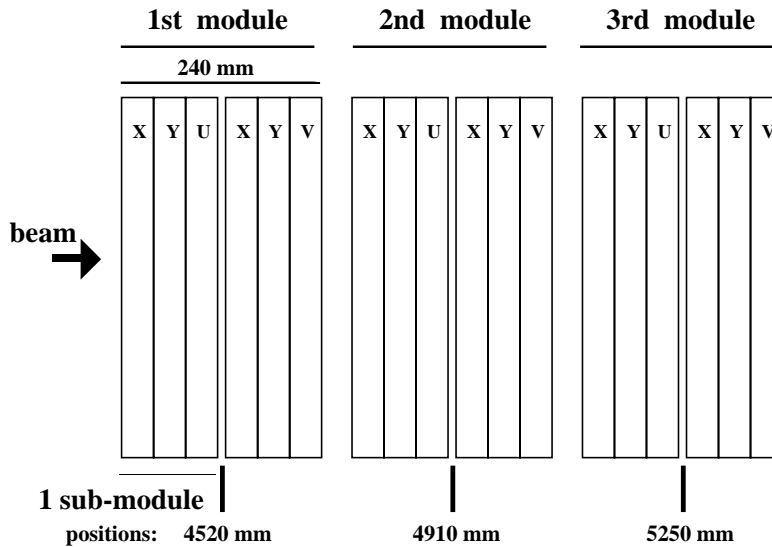


Figure 3.3: Schematic layout of the tracking station 2. The positions of the different modules along the COMPASS detector are indicated.

Every double layer consists of an inner region with straws of 6.14 mm in diameter and an outer region with straws of 9.65 mm in diameter. The following figure 3.4 shows the layout of a horizontal double layer.

Due to the very high rates expected in COMPASS (flux in the beam centre of 15 MHz/cm<sup>2</sup> [1]) and to avoid aging problems the chambers had to be insensitive in the beam area. One possibility was to introduce an insulating material between the anode and the cathode to inhibit the signals from this area. The disadvantage of this option was the introduction of passive material, causing multiple scattering and secondary interactions. Thus this option was discarded. A second proposed solution was to have a hole (see figure 3.45) in the centre of the chamber. The straws will be cut in their middle leaving

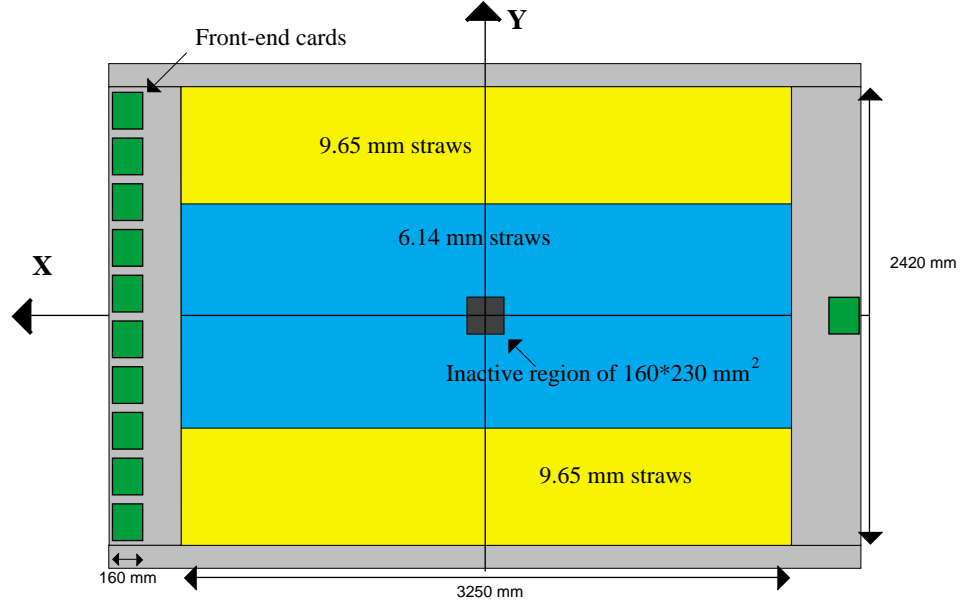


Figure 3.4: Horizontal straws, Y-plane.

the beam region free of material. The size of the hole was determined by the area covered by the small area tracking detectors, in particular by the GEMs. The active size of the GEMs is  $30 \times 30 \text{ cm}^2$ . Since the straws in the beam region are cut in two parts, the number of channels will be doubled in this area thus an extra read out electronic card is needed. In each front end card, 64 channels can be connected. The hole will match the size of the 64 channels, 32 in each layer, which also corresponds approximately to the size covered by the GEMs. The hole size is  $126 \times 220 \text{ mm}^2$ . The size of the insensitive area ( $160 \times 230 \text{ mm}^2$ ) was determined by the fact that some mechanical and electronic components should be mounted to the straws.

In table 3.3 a more detailed description of the parameters of the straws and frames is given.

<i>Parameters per double layer</i>	<i>Y double layer</i>	<i>X double layer</i>	<i>U/V double layer</i>
Orientation of the wires	Horizontal	Vertical	Inclined
Length of the straws [mm]	3658	3208	3208
Number of 9.65 mm diameter straws	256	384	384
Number of 6.14 mm diameter straws	384	448	448
Total number of straws	640	832	832
Inner area of the frame in [ $\text{mm}^2$ ]	$3250 \times 2442$	$3250 \times 2720$	$3250 \times 2720$
Active area of the chamber in [ $\text{mm}^2$ ]	$3250 \times 2420$	$3234 \times 2720$	$3234 \times 2720$

Table 3.3: Parameters of the double layers.

### 3.1.4 Materials and components of TS2

In this section, the reasons that led to the choice of materials for TS2 and the reasons for this choice are presented.

TS2, as all the other detectors in COMPASS, should be constructed with the minimum possible amount of material, to minimize the multiple scattering and the secondary interactions in the detector. Secondary interactions increase the background making it difficult to separate between track candidates. When minimizing the material in the detector the secondary interactions will be minimized. The multiple scattering will contribute to the  $D^0$  mass resolution.

The material contributes to the multiple scattering in the following way (for small angles [38]):

$$\theta_0 = \frac{13.6 \text{ MeV}}{\beta \cdot c \cdot p} \cdot z \cdot \sqrt{\frac{x}{X_0}} \cdot [1 + 0.038 \cdot \ln \frac{x}{X_0}] \quad (3.2)$$

where  $\theta_0$  is the scattering angle.  $p$ ,  $\beta \cdot c$ , and  $z$  are the momentum, velocity and charge number of the incident particle.  $\frac{x}{X_0}$  is the thickness of the scattering medium, measured in radiation lengths.

The mass of the  $D^0$  meson can be expressed as follows:

$$m_{D^0}^2 = m_\pi^2 + m_K^2 + 2E_\pi E_K - 2p_\pi p_K \cos \theta \quad (3.3)$$

where  $m_\pi$  and  $m_K$  are the masses of the pion and kaon, respectively into which  $D^0$  has decayed.  $p_\pi$ ,  $E_\pi$  and  $p_K$ ,  $E_K$  are the momenta and energies of the pion and kaon and  $\theta$  is the angle between them. For high energy particles the energy can be approximated by the momentum. Considering this approximation the mass resolution of the  $D^0$  can be expressed as follows:

$$\Delta(m_{D^0}^2) = 2m_{D^0}\Delta m_{D^0} = 2 \cdot \sqrt{(1 - \cos \theta)^2 \cdot (p_\pi^2(\Delta p_K)^2 + p_K^2(\Delta p_\pi)^2) + p_\pi^2 p_K^2 \sin^2 \theta (\Delta \theta)^2} \quad (3.4)$$

where  $\Delta p_K$  and  $\Delta p_\pi$  is the momentum resolution of the kaon and pion, respectively.  $\Delta m_{D^0}$  is the mass resolution of the  $D^0$ . The multiple scattering contributes to the  $\Delta \theta$ , thus following equation (3.2) to the  $D^0$  mass resolution. The other contribution to  $\Delta \theta$  comes from the error in the measurement of the angle between the  $p_K$  and the  $p_\pi$ .

An extensive R&D was performed in collaboration with our colleagues from the COMPASS group of Warsaw University of Technology to select the material for the straws. The R&D will be described in section 3.2.

The straw material represents one of the major contributions to the mass of TS2 (as shown in table 3.4 at the end of this chapter). Kapton was chosen as basic material for the straw cathode because of its good mechanical properties, high temperature capability and resistance to radiation damage. A highly conductive cathode is required to reduce the attenuation of electrical pulses as they travel along the straw, from the point of ionization to the electronics. The high conductivity also plays an important role in reducing the coupling from one straw to the next. Different possibilities for the straw cathode were discussed. A first option was the use of aluminium coated Kapton. This was dropped, since after a certain amount of current had flowed in a straw, a tendency develops to draw a large amount of current in a presence of a radiation source [21] [22]. A second

option was to coat the cathode with copper. This choice was discarded because of the price of copper. A third possibility was to coat the straws with carbon. This was already used for the first prototype constructed in Dubna (see section 3.3). Even though the conductivity of the straws seemed to be sufficient, this option was not convenient because of the wiring process used in which the spacers (see figure 3.43) glued to the wire were pulled through the straw, scratching away part of the carbon layer. Some zones of the prototype straws lost their conductivity since only pure Kapton was left as cathode. After several tests, it was decided that the cathode will be constituted of Kapton XC, a polyimide loaded with carbon to make it conductive. Aluminized mylar on both sides was chosen for the outer layer of the straws. In this case, two conductive layers are present which facilitates the signal transmission. The mylar is a good material for reducing the gas diffusion through the straws. The diffusion through mylar is three times smaller than for kapton. The aluminum reduces the noise and the coupling between straws. This straw wall construction, never used before, was successfully tested. The results of these tests are described in section 3.2.

For the first submodule, pure Kapton aluminized only on the inside surface will be used instead of mylar. Due to the short time scale, this decision was taken because some tests had to be done to prove the gluing properties of mylar. Kapton and mylar were both possible candidates. After the gluing tests, the decision of using aluminized mylar for the missing five submodules was taken.

For the wire material, gold plated tungsten with rhenium was the best choice. Gold and tungsten are recommended [12] for gas mixtures containing  $\text{CO}_2$  and  $\text{CF}_4$ , to be used in TS2. The wire containing Rhenium increases the value for the breaking point, which allows a higher mechanical tension that reduces the gravitational sagging of the wire inside the straw (see eq. 3.11). The values for the breaking point for both cases are:  $3100 \text{ N/mm}^2$  and  $3500 \text{ N/mm}^2$  for the wire without and with Rhenium respectively. The elastic limit is 85% to 90% of the breaking point.

Wire supports, called spacers, are situated inside the straws every 60 cm to keep the gravitational sag and offset of the wire small. At the end of each straw end-plugs are used to keep the wire in the centre of the straw. For the spacers and end-plugs different materials were proposed. PVC was one choice. It was discarded for its difficulty to glue to other materials and for its tendency to initiate aging [12]. Finally a polycarbonate material was chosen for spacers and end-plugs. Different geometries of spacers and end-plugs were proposed and tested during the R&D phase. The final description can be found in section 3.4.

Different materials were considered to provide the chambers with a stable frame. A carbon fibre frame was considered for its thermal stability. It is however expensive and difficult to machine and this option was thus abandoned. The only possibility was to use aluminium. The biggest problem with aluminium is its expansion with temperature. The expansion coefficient  $\kappa$  is defined by:  $\Delta L = \kappa L \Delta T$  where  $\Delta T$  is the local and time variations of the temperature,  $L$  the length of the object studied and  $\Delta L$  the variations in length. For the aluminium  $\kappa$  has the value of  $25 \times 10^{-6}/K$ . For an average length of 3 m and an average change of temperature of 15 degrees, the frame length will change by 1.1 mm. This change will directly influence the resolution expected for these detectors. To solve this problem a temperature stabilised tent will cover these chambers. The same tent was needed for the RICH1 detector since a change in temperature will mean a change of the index of refraction. The tent will provide a constant and uniform temperature with a

$\Delta T$  of at most 1 degree.

The amount of material introduced by the TS2 with all its elements was calculated. The table 3.4 summarises the results. The numbers are computed as average over all the surface of the chamber. The physical hole is not taken into account. For the physical hole some extra material is placed in the centre of the chamber to reinforce the area. Reinforcement is needed since the straws are cut in two parts. The detailed description of the physical hole can be found in section 3.4.

<i>Elements of a double layer</i>	<i>Composition of the elements</i>	$X/X_0$ [%]	$X/\lambda_{abs}$ [%]
Straws	Kapton + glue + Aluminized mylar	0.141	0.096
Wire	Gold-plated tungsten	$6.85 \cdot 10^{-3}$	$4.2 \cdot 10^{-4}$
Spacers	Polycarbonate	$2.63 \cdot 10^{-3}$	$1.83 \cdot 10^{-3}$
Glue (35% of the straw mass)	Epoxy	0.07	0.05
Gas	$Ar/CF_4/CO_2$	$8.19 \cdot 10^{-3}$	$4.75 \cdot 10^{-3}$
Total for double layer		0.229	0.153
Total for TS2		4.116	2.754

Table 3.4: Amount of material in radiation and interaction lengths of TS2.  $X$  represents the material thickness,  $X_0$  and  $\lambda_{abs}$  are radiation length and the nuclear absorption length respectively for the specific corresponding materials.

## 3.2 R&D

### 3.2.1 Gas

The gas mixture chosen for the straw chambers of TS2 is  $Ar/CO_2/CF_4$  74:6:20. The main reason for this choice is that a fast gas is needed for the high rate environment in COMPASS. The gas mixture should have an  $r(t)$  relation almost linear, almost independent of the electric field. Since the straw chambers will be subject to a magnetic field, it was desirable that the  $r(t)$  relation does not suffer from modifications in a magnetic field. Simulations for the  $r(t)$  relations were done using the GARFIELD [15] simulation package. The following  $r(t)$  relations were obtained for a 10 mm straw, see figure 3.5.

Simulations showed changes of less than 2 ns between 6 mm straws in a magnetic field of 0.5 Tesla and with zero magnetic field [67]. Measurements of the  $r(t)$  relation in presence of a real magnetic field are still needed. The field of SM1 is a non-uniform field which will make the calibration of the straw chambers difficult.

The gas gain was measured at the Tandem Accelerator in Garching with 26 MeV protons [53]. It was measured for the same gas mixture  $Ar/CF_4/CO_2$ , but for different percentages of the components using a straw of 8 mm diameter. Figure 3.6 shows the results of the measurement.

The gas gain for the 6 mm and the 10 mm straws was computed using GARFIELD [15]. The figure 3.7 shows the gas gain versus the wire potential for 10 mm and 6 mm straws.

The computed and the measured gas gains disagree by a factor approximately two. The measured gas gain for a 8 mm straw at 1900 V corresponds to  $9 \times 10^4$ . For achieving

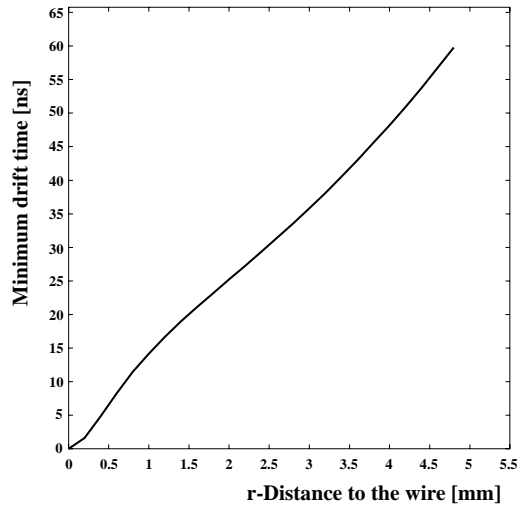


Figure 3.5:  $r(t)$  relation for a 10 mm straw with no magnetic field using Ar/CO<sub>2</sub>/CF<sub>4</sub> 74:6:20 as gas mixture.

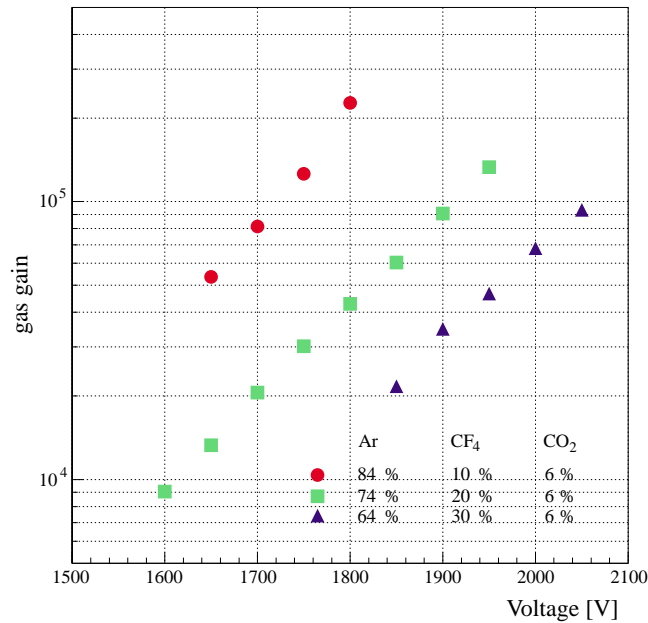


Figure 3.6: Measured gas gain versus wire voltage for an 8 mm diameter straw using the gas mixture Ar/CF<sub>4</sub>/CO<sub>2</sub> at different percentages.

the same gas gain with a 10 mm straw, the high voltage applied must be 1974 V. In figure 3.7, 1974 V for a 10 mm straw corresponds to a simulated gas gain of  $5 \times 10^4$ . Thus, in this case the simulated gas gain differs from the measured gas gain by a factor 1.8. This is due to the fact that the simulations consider only some of the physical processes involved in the gas gain calculations. Thus a disagreement between the measured and the simulated gas gain was already expected.

A gas system was designed to feed tracking station 2, corresponding to a volume of approximately 2.2 m<sup>3</sup>. Because of the high price of the mixture, a closed gas system is needed where the gas is not lost but recycled. A closed gas system has the disadvantage of the contamination. The contamination comes from the leaks and diffusion through the

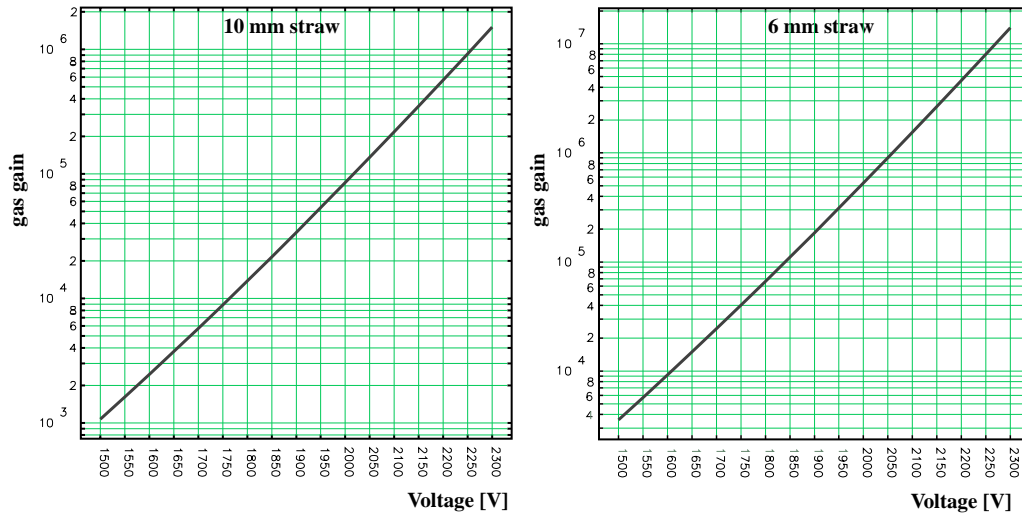


Figure 3.7: Simulated gas gain versus wire voltage for 10 mm and 6 mm straws using the gas mixture Ar/CF<sub>4</sub>/CO<sub>2</sub> (74:20:6).

straw walls. The gas must be cleaned before reinjecting it into the gas volume of TS2. The contamination inside the chamber is mainly due to water vapour, oxygen, nitrogen and CO<sub>2</sub>. The water and oxygen are regulated by removing the excesses using some surfacing processes with copper. The nitrogen and the CO<sub>2</sub> are stabilised by having a permanent leak. After passing the gas through the chamber, the correct mixture is adjusted again. In this way the losses of gas are minimized. One possibility of reducing the contamination is by using a protective gas volume around the straws. Further investigations must be done to understand which gas will be most suitable for this volume in case the protective gas is needed. A disadvantage of the protective gas volume will be the expansion of the foil which encloses the volume when filling it with gas, disturbing the detectors situated close by.

### 3.2.2 Four straw tubes

In February 1998, a small prototype made of 4 straws of 2 m length each was delivered by the “Joint Institute for Nuclear Research” (JINR, Dubna). Tests were performed in a laboratory at CERN to learn about its behaviour.

The prototype contained two different kinds of straws of 1.5 cm in diameter. Two straws had a wall consisting of two layers of carbon coated Kapton on the inside and on the outside, glued together. In between the two layers there was a thin aluminium layer. The total thickness of the straw wall was 70 μm. The other two straws differ on the outer layer. In this case, the outer layer consisted of pure Kapton. The tests were done using an <sup>55</sup>Fe source. The gas mixture used was 50% Ar, 50% CO<sub>2</sub> and the applied high voltage (HV) was 2300 V. The setup is shown in figure 3.8.

The attenuation length was measured by direct observation of the amplitude of the <sup>55</sup>Fe signals. The source was placed at several positions along the straw. The results indicated that the signal was larger on the preamplifier side and smaller at the end of the straws. This is shown in figure 3.9.

A very high noise level was observed when operating the straws. For this reason an aluminium foil was used to shield the straws from the outside noise. The test showed

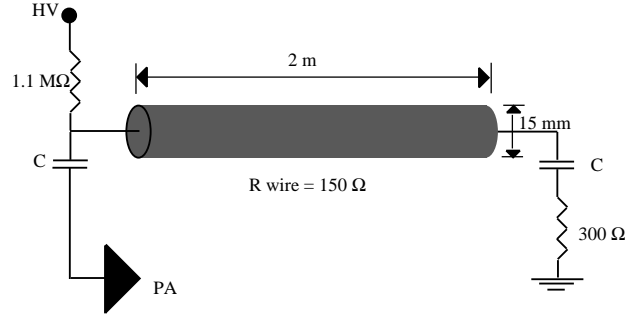


Figure 3.8: Setup for the test of the 4 straws from Dubna.

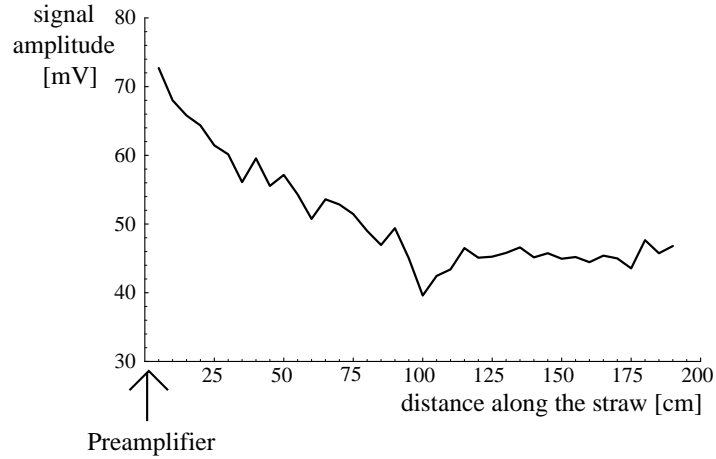


Figure 3.9: Measurement of the attenuation length. At about 100 cm the signal is smaller due to the presence of the spacer.

that the straws could not be operated without the shielding. The main conclusion was that further tests to investigate the noise problems in the straws and the attenuation effect should be performed and further more that the type and position of the different conductive layers forming the straw wall should be carefully studied.

### 3.2.3 Read out electronics

The read out chain consists of the following steps: first the signal is generated in a straw. The signal travels to the end of the straw where the motherboard is situated. The motherboard distributes the high voltage to the straws and acts as an interface to the front end card (FE card). The front end card, plugged into the motherboard, recuperates and amplifies the signal. In our case, the front end card also has a TDC incorporated. This is an advantage since it reduces the amount of cabling needed. Only one outgoing cable must be connected to the global data collector. This read out card was specially designed with the high rates of the COMPASS experiment in mind [66].

#### Signal transmission

When a particle traverses the straw connected to high voltage and filled with gas, it ionizes the gas. As explained in section 3.1.1 the signal is formed by induction due to the

movement of the ions and electrons as they drift towards the cathode and anode. Since the multiplication region is limited to a distance of a few wire radii, the contribution of the electrons to the signal is small compared to the positive ions [43].

The signal created will split into two equal parts travelling towards the tube ends [39]. The propagation along the tube is ruled by the properties of a coaxial transmission line with the characteristic complex impedance dependency on the frequency, as shown in equation 3.5.

$$Z_0(\omega) = \sqrt{\frac{R(\omega) + i \cdot \omega \cdot L}{G(\omega) + i \cdot \omega \cdot C}} \quad (3.5)$$

where  $\omega$  is the frequency,  $Z_0(\omega)$  is the frequency dependent impedance,  $R(\omega)$  and  $G(\omega)$  are the wire resistance and the dielectric conductance respectively, both frequency dependent.  $L$  and  $C$  are the inductance and capacitance respectively. The frequency band of the amplifier that will be used for the read out (see section 3.2.3) is 1-100 MHz. For high frequencies the complex wave impedance can be approximated by:

$$Z_0(\omega) \rightarrow \sqrt{\frac{L}{C}} \quad (3.6)$$

where  $L$  and  $C$  are determined by the tube's geometry. The inductance is given by:

$$L = \frac{\mu \cdot l}{2 \cdot \pi} \cdot \ln \frac{b}{a} \quad (3.7)$$

where  $\mu$  is the magnetic permeability of the medium,  $l$  is the length of the straw,  $b$  its diameter and  $a$  is the diameter of the wire. The capacitance is given by:

$$C = \frac{2 \cdot \pi \cdot \varepsilon \cdot l}{\ln \frac{b}{a}} \quad (3.8)$$

where  $\varepsilon$  is the electric permittivity of the medium.

The impedance versus the frequency in a straw tube of 10 mm diameter was simulated and it is shown in figure 3.10.

For gases the permittivity and permeability constants are approximately those of vacuum, that is,  $\varepsilon \approx \varepsilon_0 = 8.85 \cdot 10^{-12} \text{F/m}$  and  $\mu \approx \mu_0 = 4 \cdot \pi \cdot 10^{-7} \text{H/m}$ .

The end of the straw should be "correctly" terminated according to the tube's wave impedance to avoid reflections of the signal when this reaches the end of the tube.

Thus we can calculate the approximate impedance of the straws considering a wire diameter of 30  $\mu\text{m}$ , and straw diameters of 10 mm and 6 mm. The inductance per unit of length is  $11.6 \cdot 10^{-7} \text{H/m}$  for the 10 mm straw and  $10.6 \cdot 10^{-7} \text{H/m}$  for the 6 mm straw. The capacitance per unit of length is  $9.6 \cdot 10^{-12} \text{F/m}$  for the 10 mm straw and  $10.5 \cdot 10^{-12} \text{F/m}$  for the 6 mm straw. Introducing these values into the equation 3.6, the impedances obtained have a value of approximately 348  $\Omega$  for the 10 mm straw and 318  $\Omega$  for the 6 mm straw.

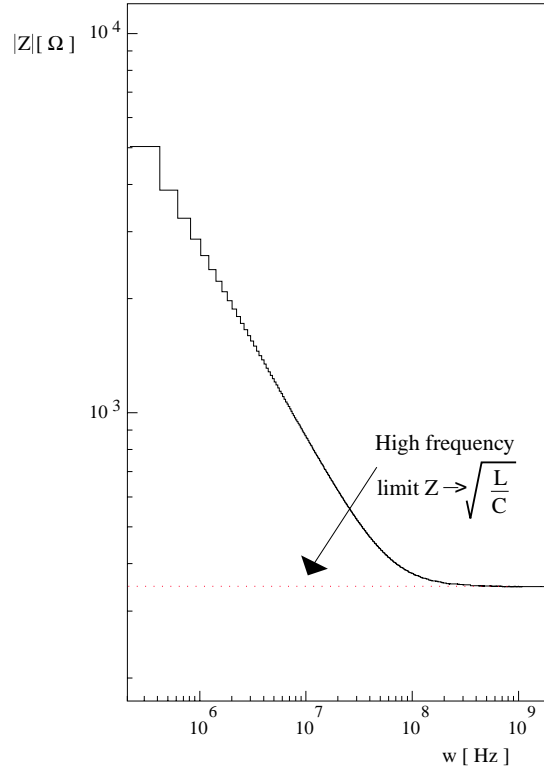


Figure 3.10: Impedance versus frequency for a 10 mm straw. The dashed lines shows the high frequency limit.

## Motherboard

Straws of the same diameter in a layer form blocks of 64. Each block is connected to one front end card via a 64 channel motherboard [55]. The main high voltage (HV) bus of each motherboard (MB) is connected to an individual HV supply channel via a 1 k $\Omega$  resistor. This resistor, together with 1 nF decoupling capacitors connected to the HV bus, create a filter which reduces the noise level. Additionally, the MB channels are divided into eight groups, each of them consisting of eight neighbouring channels. Each group is supplied by the local HV bus, which is connected to the main HV bus via 1 M $\Omega$  resistor. Thus, in case of breakdown of an anode wire producing a short circuit between the straw HV and the ground, only one group of 8 straws will be switched off.

The anodes of the straws under high voltage are coupled to the input of the amplifier/discriminator ASD8B via 82 pF high voltage capacitors and via serial resistors (240  $\Omega$  or 270  $\Omega$ ). This will provide the right impedance matching between the characteristic impedance of the straw (exact impedance 360  $\Omega$  or 390  $\Omega$  depending on the tube diameter) and the input impedance of the ASD8B (120  $\Omega$ ) [13]. The values of the coupling capacitors were chosen based on the theoretical analysis of the impedance matching. They are lower than the ones commonly used in similar circuits (1 to 1.5 nF). Small capacitors have several advantages. One advantage is a better impedance matching. In case of electrical discharge inside the straw, the charge accumulated in the capacitor is significantly smaller. Subsequently there is a decrease of the risk of damaging the amplifier and the anode wire.

The motherboard provides also the possibility of testing the read out system. This

is achieved by injecting a charge directly to the amplifier inputs. The pulse from the computer controlled pulse generator is distributed along the test path (test bus). This is coupled to the amplifier input via small capacitors of about 0.13 pF.

The motherboard contains also a set of 64 diodes BAV99 which provide an ASD8B input protection in case of electrical discharge.

Figure 3.11 shows the circuit diagram for the motherboard [55].

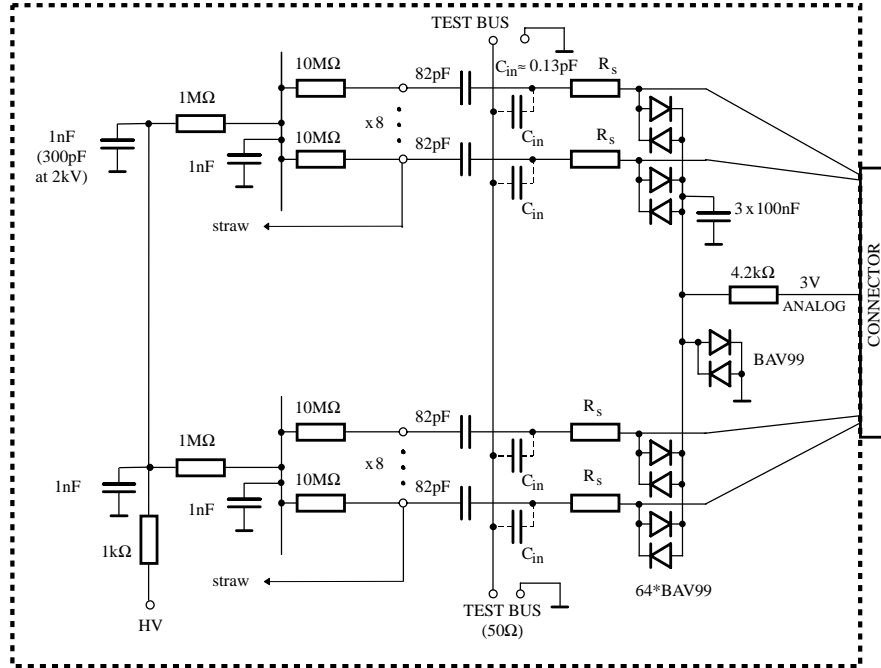


Figure 3.11: Circuit diagram of the motherboard that will be used in the straw chambers of TS2 [55].

### Front end cards

The Front End (FE) card developed by Freiburg [66] provides 64 channels for the straw read out. The main components of the card are the ASD8b preamplifier and the F1 chip. The F1 chip is a high resolution TDC. Its digitization of time is 130 ps. This chip was developed specially by Freiburg to provide a dead time free read out and to guarantee a high speed data recording. There are eight F1 chips on a read out card, each digitizing eight channels, leading to 64 input channels. There are eight ASD8b preamplifiers, one for each F1 chip. The threshold of the preamplifiers is controlled by eight DAC (Digital to Analog Converter). Each DAC can be set individually by means of the F1 chip. This provides the option of setting the threshold for each of the 64 straws individually, very useful tool because every channel can behave differently. The data from the FE card will be transmitted to the CATCH via a serial hotlink protocol. CATCH combines the data of up to 16 FE cards. The straw geographical identity is in the FE card and will be transmitted to the offline, independently of the CATCH and FE card to which it is connected.

A test beam took place in June 1999 to decide the best suited preamplifier for the FE card. Two possibilities were studied, the ASD8b and MAD-IV preamplifiers. The chamber

used was the prototype built in Dubna (the prototype is described in section 3.3). What was compared was the time resolution and the efficiency response of the two different preamplifiers. The main results from that test will be summarised here. More detailed information is given in a COMPASS note [40].

The time resolution was calculated adding up two drift times measured in adjacent straws. This sum is considered a constant, assuming the drift velocity constant and the tracks divergence negligible. This is a valid approximation to get a reasonable comparison between both preamplifiers but not for giving a final result about the resolution of the straws. The width of the distribution of this sum is the convolution of the time resolution of the straws.

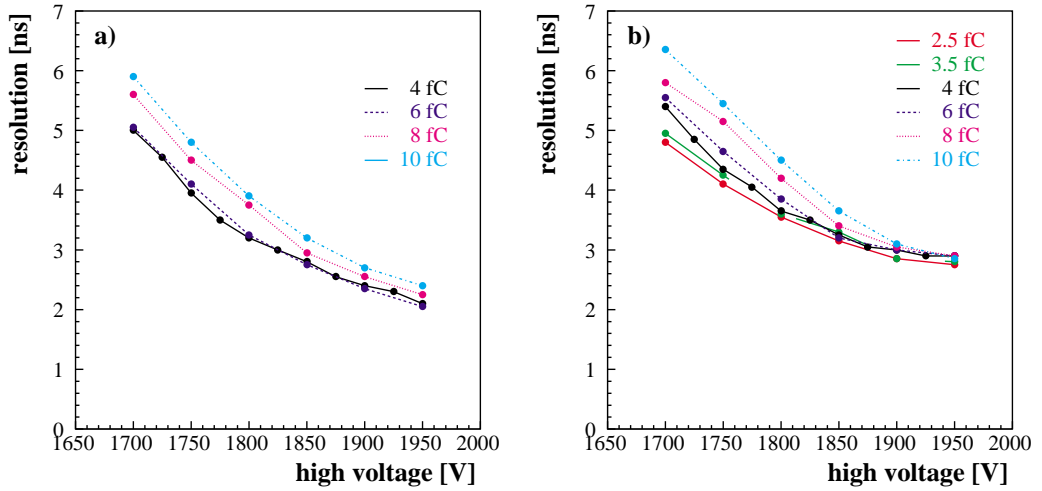


Figure 3.12: Convoluted time resolution of two straws as a function of the high voltage settings and of the different thresholds of the discriminators for the a) ASD8b and b) MADIV.

The resolution when using the MADIV chip seemed to be worse than when using the ASD8b, see figures 3.12. The lowest value for the ASD8b threshold was 4 fC. Lower values were reachable when using the MADIV. Lower values were not reached when using the ASD8b because of interferences between the output signal with the small input signal. Even with higher thresholds a better time resolution was obtained when using the ASD8b.

The efficiency was measured reconstructing tracks with the help of a silicon telescope and projecting them to the straw chamber. The efficiency is defined as the ratio between the hits recorded by the straws divided by the total amount of reconstructed tracks in the telescope.

Figure 3.13 shows the efficiency versus the z position (drift distance) for different gas gains at a fixed threshold: 4 fC. The efficiency near the walls is better for the ASD8b at higher gains than for the MADIV.

The results showed that the ASD8b preamplifier fulfils the experimental requirements better than the MAD-IV preamplifier. However the MAD-IV preamplifier did not show the same strong tendency to oscillate as the ASD8b preamplifier. The main outcome of the test was the decision of equipping the final front end card with the ASD8b preamplifier. The decisive factor was the better time resolution of the ASD8b chip. Another important parameter to be decided on was the operating gain. From the plots, the high voltage which gives better efficiency and resolution for the 10 mm straws is 1950 V. At this voltage even

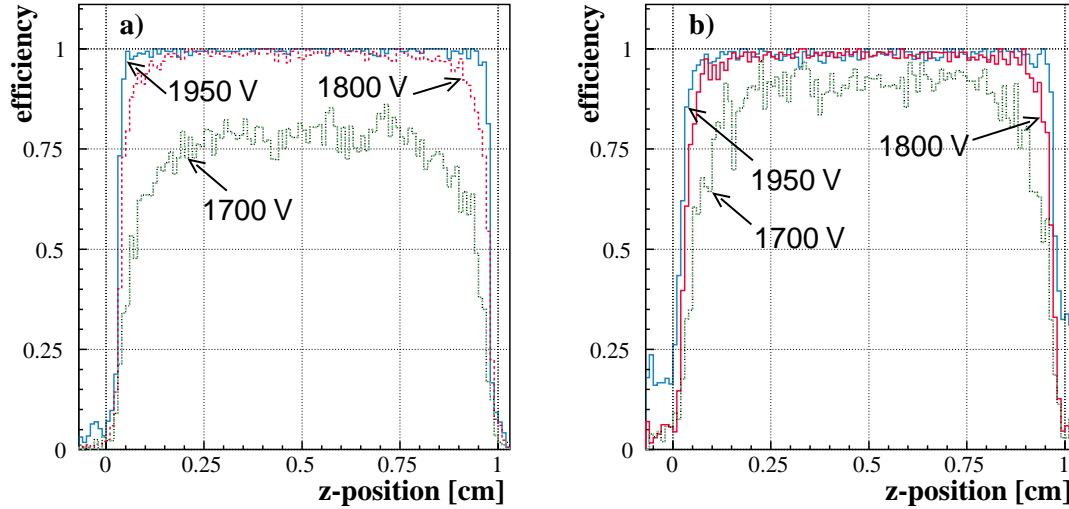


Figure 3.13: Efficiency as function of drift distance  $z$  for the a) ASD8b and b) MADIV, at three different gas gains. (The wire position is at 0.5 cm).

if the threshold of the ASD8b preamplifier chip has to be higher because of noise problems, the resolution (see fig. 3.12.a) and the efficiency (see fig. 3.14) do not change dramatically.

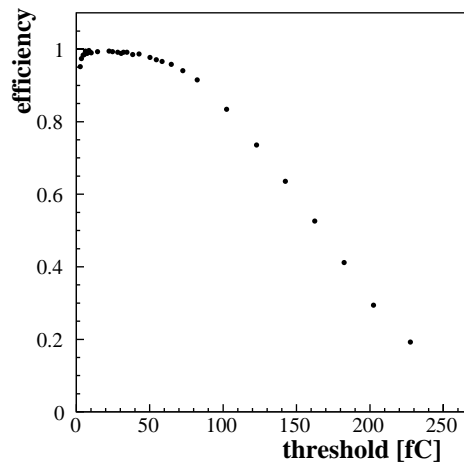


Figure 3.14: Efficiency at a drift distance of  $1 \text{ mm} \leq r \leq 2 \text{ mm}$  measured with the ASD8b at 1950 V.

### 3.2.4 Electrical properties of the straws

The electrical properties of the straws were investigated in collaboration with our colleagues from the Warsaw University of Technology, Poland. Different cathode materials and configurations were studied. The simulations were done by making a model of the signal transmission in a straw tube. The results of these simulations are collected in two COMPASS internal notes [13] [14]. Here we will summarise the most important results.

The straw tubes are usually manufactured by cutting long strips of material and winding them in spiral to get a tube. Since the straws form the cathode of the chamber, they should be conductive on the inside. As a base material Kapton was chosen because of its good mechanical properties and its resistance to high temperatures. The cathode

properties are important only in the frequency range of the preamplifier. In our case using the ASD8b preamplifier, this corresponds to frequencies between 1 to 100 MHz. Different straw wall configurations were tested. Here the most interesting ones are described. The first configuration tested was the one used for the two straw chamber prototypes built in Russia. The straws consisted of coated Kapton, the coating consisting of carbon on the Kapton layer. A second configuration was straws made out of carbon loaded Kapton or Kapton XC with aluminized mylar as outer layer. The Kapton XC contains already the carbon. In both cases, the straws are made of two conductive layers separated by a layer of glue. The result of the simulation showed that the straws consisting of Kapton XC have a better signal transmission compared to the carbon coated straws. The signal transmission depends mostly on the conductivity of the layers of the straw wall. A high conductivity implies a better signal transmission. Figure 3.15 shows the result of this simulation.

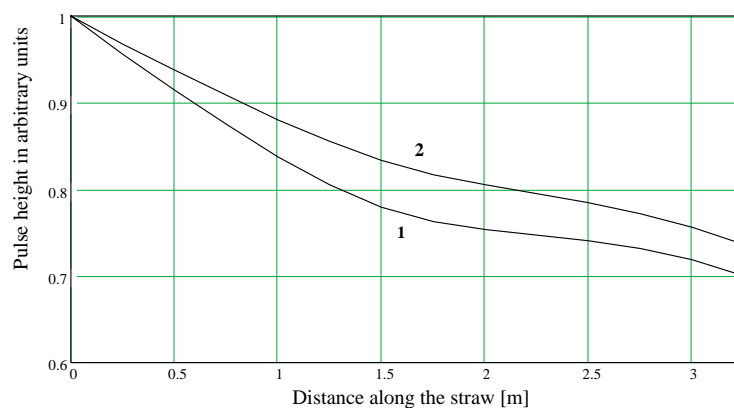


Figure 3.15: Pulse height simulation as a function of the source position along the straw. Diameter of the straw: 6 mm. Number 1 is the straw with carbon coated Kapton, as those used in the prototypes built in JINR and MSU. Number 2 is the straw with Kapton XC with aluminized mylar.

The cross-talk level was also simulated. The straw made of Kapton XC showed also in this case a better behaviour than the carbon coated straw. The cross-talk level was lower for the straws consisting of Kapton XC.

The simulation helped choosing Kapton XC for the straw cathodes. Two tests were performed. First the material was checked for radiation damage (see 3.2.5). A second test about the behaviour of the material on a full size straw was performed. This will be described in section 3.3.

### 3.2.5 Aging

A small prototype was developed at CERN. This prototype was constructed with straws made of Kapton XC with an outer layer of double sided aluminized mylar. The material used corresponds to the final choice for TS2. The diameter of the straws was 8 mm and their length was 60 cm. This length was chosen to avoid the problem of inserting spacers inside the straws. The straws were placed in a high precision aluminium profile. The profile consisted of several u-profiles one next to the other. The size of every u-profile was of 9 mm in the inside. This profile led to a special design of the end-plugs which were made to centre the straw in this u-profile. They had one hole for the pin where the wire

was inserted and crimped. They also had holes for the gas input and output connection. Figure 3.16 shows the design of the endplug.

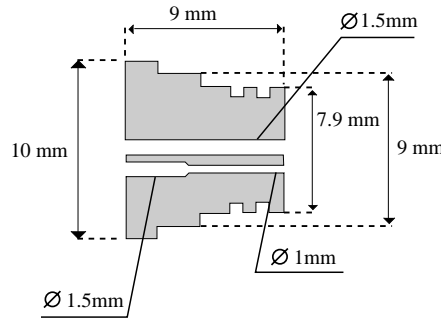


Figure 3.16: Endplug specially designed for a prototype. One hole is for the pin which will centre the wire and the other one, with two different diameters, is for the gas connection.

The gas output of one straw was connected to the gas input of the next straw, they were connected in serie. A hole was made in the centre of the aluminium profile to eliminate the unnecessary material. The aging tests [52] [53] were performed at the Garching Tandem Accelerator with 27 MeV protons using the prototype described. Working with these protons, six to thirty years of COMPASS operation could be simulated in three days (depending on the gas gain chosen), since they will deposit 10 times more energy than minimum ionising particles. During these tests the gas used was Ar/CF<sub>4</sub>/CO<sub>2</sub> (74:20:6). This gas was chosen since it will be the operating gas in the TS2. Charges up to 1 C/m were collected on the anode wire but no significant aging effect was observed. As shown in figure 3.17.a no significant losses were observed in the pulse height for the straws with the COMPASS gas.

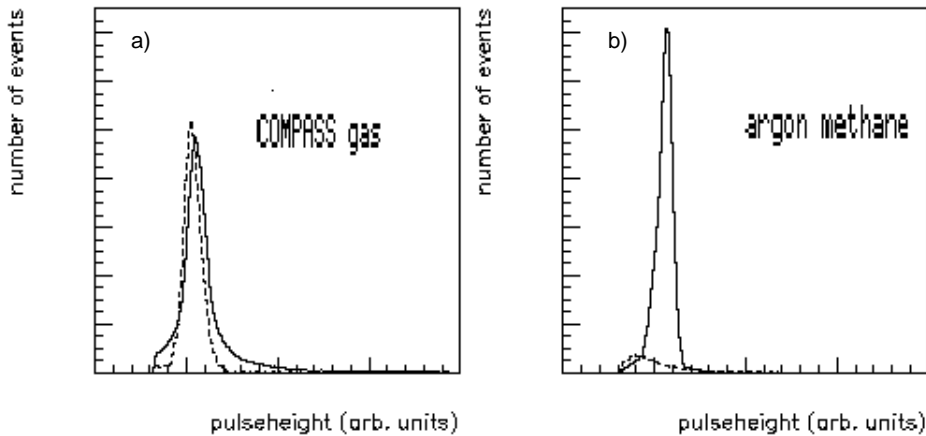


Figure 3.17: Pulseheight spectra before (solid lines) and after (1.1 C/cm, dotted lines) proton irradiation for two different gases a) the COMPASS gas and b) argon methane. The spectra was taken using an <sup>55</sup>Fe source.

To prove that this was a good method to study radiation damages, some sample of straws were filled with another gas, Ar/CH<sub>4</sub> (90:10). This gas is known for causing aging problems. The straws were irradiated under the same conditions as the straws filled with the COMPASS gas. An increase of the electrical current at constant proton flux was

clearly seen. A significant loss of pulse height (see figure 3.17.b) was also observed. This increase in the current was probably due to the creation of an electrical dipole layer on the cathode plane, an effect called the “Malter effect”. After the tests, the straws were opened to check for deposits on the cathode wall or on the wire. In fact, some deposits were found on the wire in the straws irradiated with the gas Ar/CH<sub>4</sub>.

### 3.2.6 Rate capability

A dedicated measurement was performed in September 1999 at the M2 beam line at the SPS at CERN with the same rates as the ones expected in COMPASS. The main goals of the tests were to measure the efficiency and the occupancy as a function of flux rates. The tests were done with a prototype built in Dubna consisting of 6 mm and 10 mm straws. The prototype has an insensitive area in the centre of the chamber for the beam. (The prototype is described in more detail in section 3.3). The setup was as follows: the chamber was situated after SM1, corresponding to its nominal position. Downstream of the straw chamber, a large scintillator was placed horizontally and further downstream two small scintillators were placed forming a cross (vertically and horizontally, see figure 3.18).

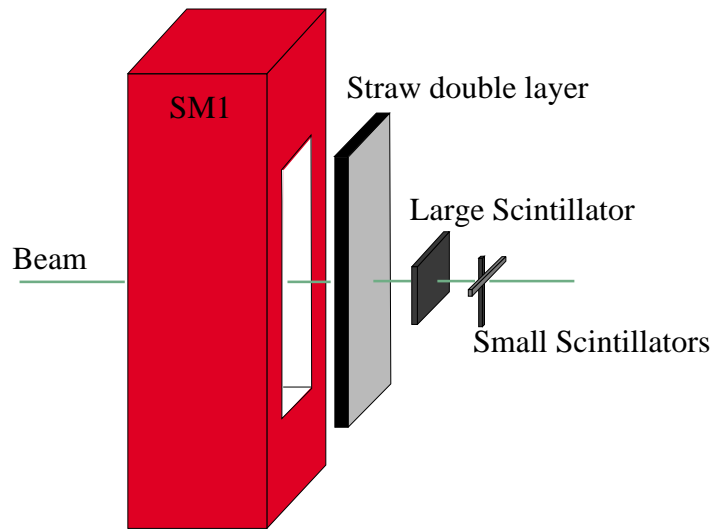


Figure 3.18: Setup for the rate measurements performed in September 1999 at the M2 beam line at the SPS at CERN.

The chamber was running with Ar/CO<sub>2</sub>/CF<sub>4</sub> at a flow of 6 l/h, the total volume of the chamber being 40 l. The straws in the chamber were read out exclusively by scalars. The first measurement’s goal was to obtain the efficiency versus high voltage and its dependence on the rates. The efficiency was obtained using the following method: three straws are chosen, two from one layer and one from the other layer, that were labelled 2, 3 and 4, see figure 3.19.

The efficiency was computed by taking the coincidence between the straw 2 and the straw 3, then the coincidence between the straw 3 and the straw 4. The rates given by these coincidences were added. The result of this addition was divided by the free rate obtained in straw 3. This efficiency was measured for different high voltages. These measurements were repeated for a low ( $2 \cdot 10^7$  particles/spill) and high ( $2 \cdot 10^8$  particles/spill) muon beam intensity, and for a pion beam ( $2.5 \cdot 10^7$  particles/spill). Figure 3.20 shows the

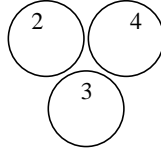


Figure 3.19: Straws configuration for the efficiency measurements.

efficiency measurements with the muon beam for high and low intensity. From the results it can be concluded that no significant drop of the efficiency is visible.

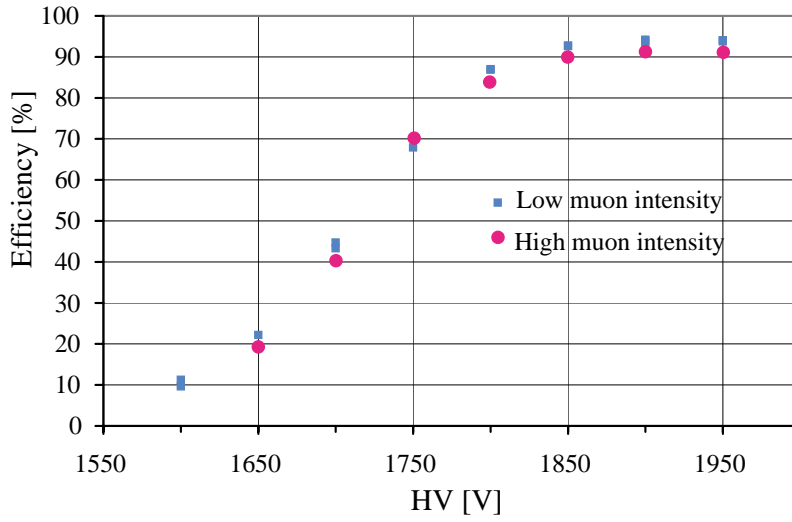


Figure 3.20: Efficiency versus high voltage for high and low intensity muon beam.

Measurements of the rates and measurements of straw chamber characteristics that might be influenced by the rates were performed. To obtain the beam profile it was enough to measure the free rates on the straws.

The normalised rate, obtained as the free rate on a straw divided by the beam intensity (which was provided by a ionization chamber) was measured in the following three different conditions: muon beam with target in/out, muon beam of high/low intensity and muon beam with magnet on/off. A measurement was also performed with a hadron beam.

The figure 3.21.a shows that the rate in the straws is higher when the target is in (the target was 2.6 interaction lengths). The result agrees with the expectation. When the target is in, the hits in the straw chamber correspond to particles from the beam and from the interaction of the beam in the target.

The figure 3.21.b shows that the rate is lower when the magnet is on. The explanation for this effect is the following: when the magnet is on, the particles with low momentum are strongly deflected by the magnet. Therefore, they do not reach the straw chamber. Thus the rate in the chamber will be lower than when the magnet is off.

The same kind of measurements were performed with a hadron beam, of  $\pi^-$  with an energy of 225 GeV. The only parameter which was changed during the measurement was whether the target was in or out (see figure 3.22). The target was made of polyethylene with 10% interaction length.

The tests were performed using 10 mm straws. The main reason for this choice was the easier alignment of the chamber in the beam. The 10 mm are situated at the outer

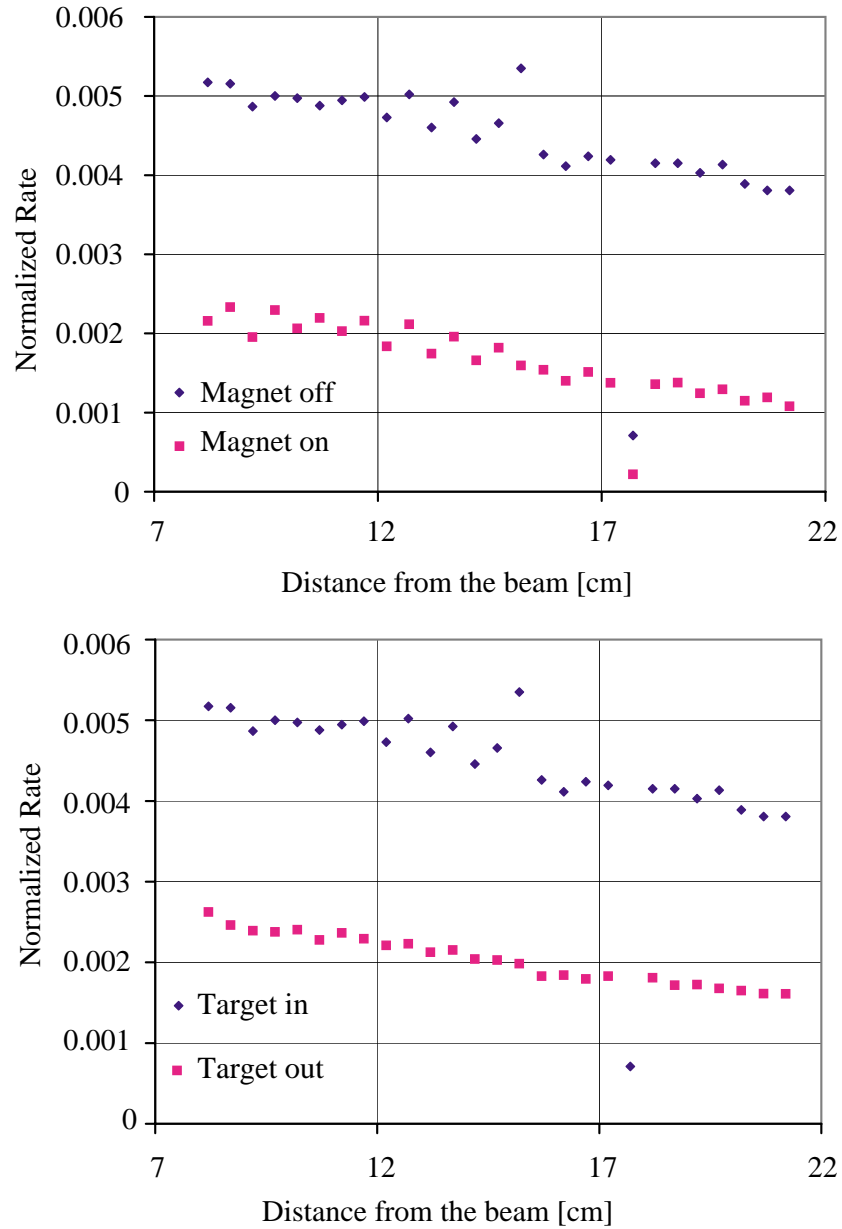


Figure 3.21: The normalized rate i.e., the rate in the straws divided by the beam rate. The figures show the measurement of the normalized rate for a high intensity muon beam in two different cases: a) target in and target out (the SM1 magnet is switched off). b) SM1 magnet is switched off or on (the target is in).

part of the chamber, thus only vertical alignment was needed.

The occupancy is defined as the number of tracks passing through the straws in a time gate corresponding to the drift time of the straw. The maximum occupancy for a 10 mm straw can be calculated as:

$$\begin{aligned}
 \text{Maximum occupancy} &= (\text{maximum measured normalized rate}) \\
 &\quad \times (\text{highest expected beam rate}) \\
 &\quad \times (\text{maximum drift time})
 \end{aligned} \tag{3.9}$$

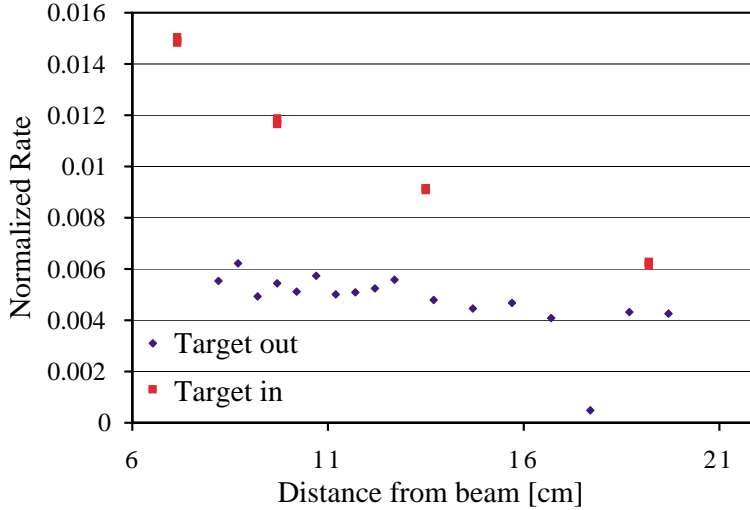


Figure 3.22: The figure shows the measurement of the normalized rate for the hadron beam for two different conditions, when the target is in or out (the SM1 magnet is switched off).

To extract the occupancy for the 6 mm straws from the occupancy measurements for the 10 mm straws, the measurements have to be multiplied by a factor  $(\frac{6}{10})^2$ . The reason for this factor is that the tracks are traversing a straw of a diameter  $\frac{10}{6}$  smaller than the one for the 10 mm straws. The other factor  $\frac{6}{10}$  comes from the fact that the drift time is shorter by this factor for the case of the 6 mm straws. The maximum occupancy for 6 mm straws closest to the beam corresponds to the case where the target is in. The results for this case are:

- for the hadron beam, the maximum occupancy with the magnet off is 2% (Beam: 220 GeV  $\pi^-$ , beam intensity:  $5 \cdot 10^7 \text{ s}^{-1}$ ).
- for the muon beam, the maximum occupancy with the magnet off is 3,6% (Beam: 100 GeV  $\mu$ , beam intensity:  $2 \cdot 10^8 \text{ s}^{-1}$ ).
- for the muon beam, the maximum occupancy with the magnet on is 2% (Beam: 100 GeV  $\mu$ , intensity:  $2 \cdot 10^8 \text{ s}^{-1}$ ).

These results are consistent with the proposal and with Monte Carlo simulations. The Monte Carlo simulations were performed using as event generator called FRITIOF [37]. It is an event generator which simulates the interactions between hadrons and nuclei.

The figure 3.23 shows the  $x$  and  $y$  distribution for particles at the same distance from the target as the straw chamber in COMPASS. As beam particles  $\pi^-$  were chosen.

The occupancy is computed dividing the entries for an  $x$  or  $y$  position by the total amount of generated events, and multiplying this quantity by the beam intensity, the interaction length of the target material (to simulate the number of interactions that will occur in the target) and the drift time. In figure 3.24, the different values for the occupancy are computed for different distances to the beam centre. A value of 2.2% occupancy is obtained for the straw nearest to the beam, considering that there will be a physical hole for the beam. This value agrees with the 2% occupancy measured in M2 for the hadron beam.

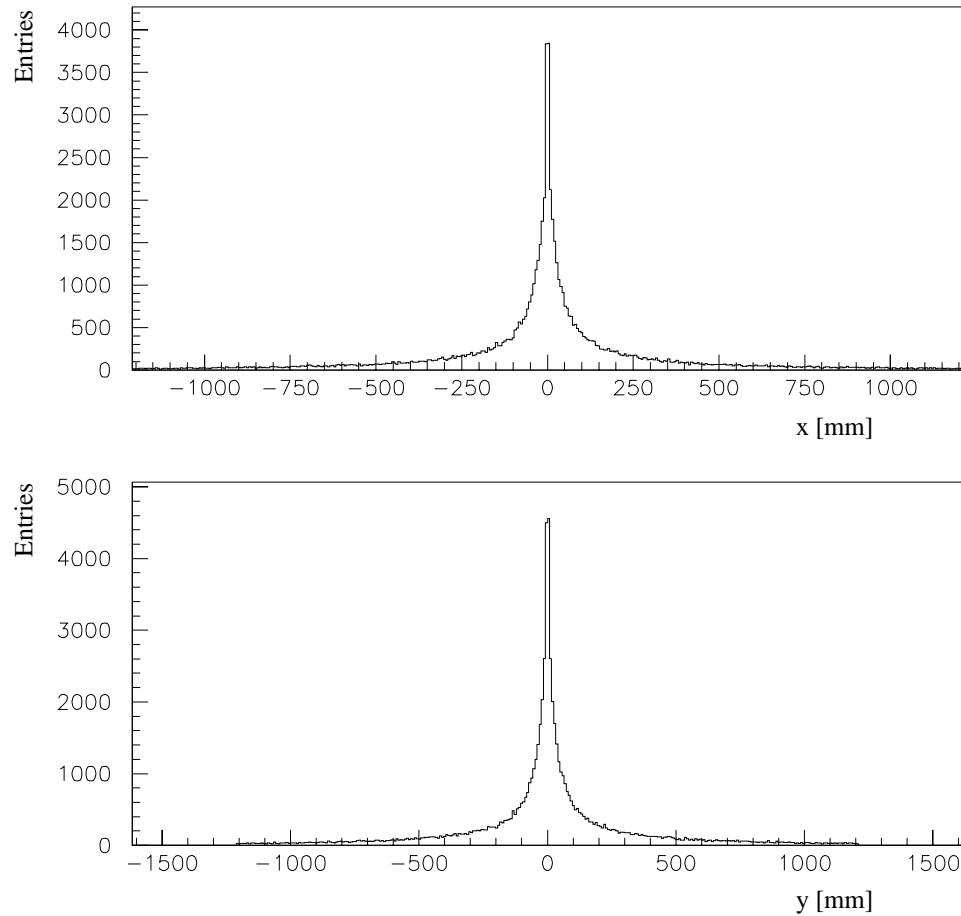


Figure 3.23: Simulated particle distributions in a chamber plane in the  $x$ -direction and in the  $y$ -direction.

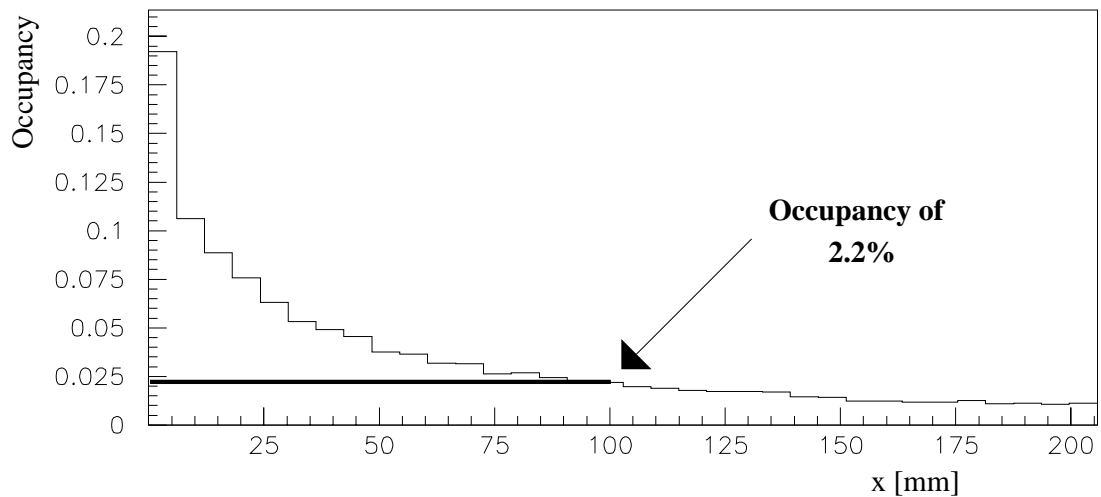


Figure 3.24: Simulated occupancy at different distances to the beam centre. The value of 2.2% is obtained for 100 mm which will be the distance at which will be situated the straw from the beam centre.

### 3.3 Tests of prototypes

In 1998 two prototypes of straw tube drift chambers were constructed and tested in order to measure efficiency and resolution [41]. The tests were performed at the X5 beam line

at CERN. One prototype was designed and constructed at Moscow State University and the second one was designed and constructed in JINR at Dubna. The prototypes differ in size and in their conceptual design.

### 3.3.1 Design considerations for two prototypes by MSU and JINR

Both prototypes consist of 2 layers of straws (one double layer). Each layer consists of one inner region with 6 mm diameter straws and one outer region with 10 mm diameter straws. The straws are made from a  $2 \times 25 \mu\text{m}$  coated Kapton film. The coating itself consists of an aluminium layer with carbon. Therefore the straws are conductive inside and outside.

The Moscow prototype is about  $60 \times 80 \text{ cm}^2$  and contains  $2 \times 16$  channels of the 10 mm straws and  $2 \times 96$  channels of the 6 mm straws. The prototype has 2 gas volumes. The first gas volume is the inlet and outlet for the straws themselves. The second one, which protects the straws from the outside atmosphere, is made by placing a mylar foil around the straws. Both volumes are filled with the same gas. The frame is constructed to hold the wire tension. The measured wire tension was around 80 g for the Moscow prototype.

The Dubna prototype has an active area of  $240 \times 120 \text{ cm}^2$ . It contains  $2 \times 60$  channels with 10 mm diameter and  $2 \times 96$  channels with 6 mm diameter straws. In this case, the nominal wire tension was 50 g.

In both prototypes plastic element supports were used to maintain the wire position. These spacers have one  $100 \mu\text{m}$  diameter hole in the centre for the wire and 3 holes for the gas flow. The spacers were of different design for both prototypes but the results were similar for both cases.

Both prototypes had an insensitive area in the centre achieved using different methods. Both solutions worked as expected, no signals were registered in this region. The Moscow solution for the blind region consisted in using in this area straws where the inside was non conductive. The Dubna prototype solved the problem by putting a mylar tube inside those straws. The final detector should have a real physical hole for the beam in addition to the insensitive area.

### 3.3.2 Laboratory tests

The wire tension of both prototypes was measured by using a device manufactured by CAEN. It worked as follows: a current was applied to the wire and by using a magnet the wire started to oscillate. The frequency of oscillation is related to the tension by [42]:

$$f_n = \frac{n}{2 \cdot l} \cdot \sqrt{\frac{T}{\rho \cdot A}} \quad (3.10)$$

where  $f_n$  is the frequency of oscillation of the  $n^{\text{th}}$  harmonic,  $T$  is the tension applied to the wire,  $A$  its cross-section,  $\rho$  its density, and  $l$  its length. The results showed for most of the cases small deviations with respect to the nominal wire tension.

Both prototypes were tested with an  $\text{Fe}^{55}$  source. Different channels were tested for different voltages and the current was monitored. The motherboard for the Moscow prototype showed some problems with dark current. After some modifications the chamber

was operating as expected. Some problems to keep the high voltage appear for the Dubna prototype.

The Moscow prototype was checked at CERN for gas leaks while the Dubna prototype was checked at Dubna before shipping it to CERN.

### 3.3.3 Test beam measurements

Both prototypes were tested at the X5 beam line in the west area at CERN. The experimental setup consisted of two overlapping scintillators of  $4 \times 4 \text{ cm}^2$ , a silicon microstrip detector with 3 planes (every plane containing 4 orientations, one vertical, one horizontal, and 2 inclined) and the prototype.

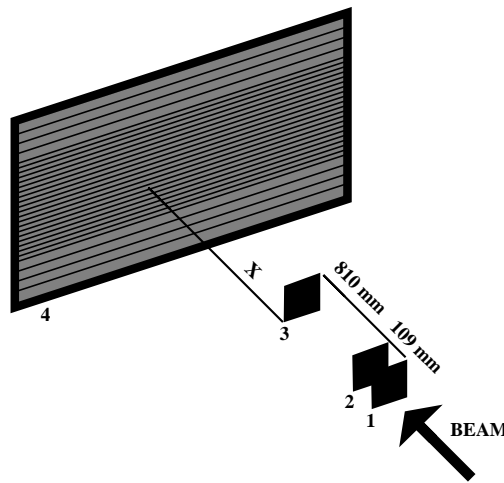


Figure 3.25: Test beam setup. 1, 2, 3 are the different planes of the silicon detector. The distance was 109 mm between 1 to 2 and 810 mm between 2 and 3. 4 is the prototype, and its distance from the silicon plane number 3 was  $X = 901 \text{ mm}$  for the Dubna prototype and  $X = 521 \text{ mm}$  for the Moscow prototype.

The trigger signal was given by a coincidence of the two scintillators. The silicon telescope allows the extrapolation of the track to the chamber with an accuracy of  $10 \mu\text{m}$ . The chamber was mounted on a scanner which allowed its precise movement in the  $x$  and  $y$  directions. Figure 3.26 shows a photo of the Dubna prototype mounted on the scanner.

In May 1998 the Moscow prototype was tested using a gas mixture of  $\text{Ar}/\text{CO}_2/\text{CH}_4$  (74:20:6). Half of the chamber was read out using an “old” preamplifier and discriminator that were not electronically matched to the chamber. The other half of the chamber was read out by a “new” Front End card designed by Freiburg based on the ASD8b chip. In both cases some straws were terminated with a resistor of  $330 \Omega$  and a capacitor of  $1 \text{ nF}$ . Both values were not perfectly matched to the impedance of the straw. The operating HV was 1750 V for the 6 mm straws and 1970 V for the 10 mm straws, leading to a gas gain of  $4 \cdot 10^4$ .

The Dubna prototype was tested in August 1998. Another gas mixture  $\text{Ar}/\text{CF}_4/\text{CO}_2$  (74:20:6) was chosen to get a more linear gas. In this test only the “new” Freiburg Front End was used and all the straws were terminated. Again the electronic matching between the termination and the straw was not ideal:  $330 \Omega$  for the resistor and  $1 \text{ nF}$  for the capacitor. The nominal HV at which the straws were operated is 1650 V for the 6 mm

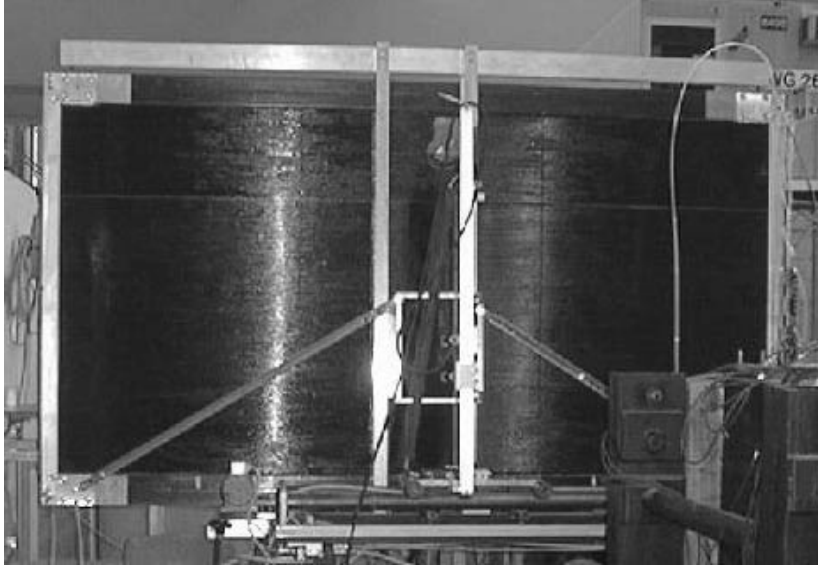


Figure 3.26: Dubna prototype mounted on the scanner in the test beam area.

straws and 1800 V for the 10 mm straws. The electronics threshold, which indicates the value at which the preamplifier will react, was set to 800 mV corresponding to 4 fC (25,000 electrons). The value of the threshold has a strong influence on the results. For having the best resolution the threshold should be set to trigger on the first cluster. The first cluster is the one with shortest path to the wire. The number of electrons in a cluster is similar to the Poisson distribution but with higher kurtosis (long tail). The mean value is 3 but 62% of the clusters have one electron, 21% have two electrons and 6% have 3 electrons [69]. For a gas mixture containing Ar and CO<sub>2</sub> the average number of electrons in a cluster is 3 and a primary ionization is produced every 330  $\mu\text{m}$  in average. The chamber was working at a gas gain of  $2 \cdot 10^4$ . To trigger in the first cluster means that this should contain at least 2 electrons. For the mentioned values the probability to trigger in the first cluster is 38%. Nevertheless this probability is strongly decreased due to the losses of charge produced in the avalanche because of charge division and other processes. 4 fC threshold was the lowest achievable in the test beam area due to noise problems. With lower noise level, the threshold could be reduced and consequently a better resolution could be achieved. In order to understand better the electrical properties of the straws the group from the Warsaw University of Technology developed a simple model described in a COMPASS internal note [13]. Some of the results are:

- the straw cathode is transparent in the frequency range of the ASD8b chip, 1 MHz-100 MHz, therefore the signal seems to travel between the wire and an external ground,
- the termination plays an important role.

The main read out electronic consisted of TDCs with 50 ps time resolution. The DAQ system recorded the TDC values and the hits on the silicon telescope to tape.

### 3.3.4 Analysis and results

The analysis was focused on determining the resolution of the prototypes, the efficiency and the dead area caused by the spacers. Some conclusions about the working conditions of these detectors could also be retrieved from these tests. A silicon telescope was chosen to measure the resolution of the drift chamber because of its good spatial resolution, better than  $10\ \mu\text{m}$ .

Two informations are used for the analysis; the TDC drift time and the hits in the silicon telescope. A valid hit in the straws results in a TDC drift time below 100 ns. All other values are considered as overflows. The silicon telescope gives the vertical and the horizontal positions of the hits. The vertical position is defined across the straws and the horizontal position along the straws (see figure 3.27).

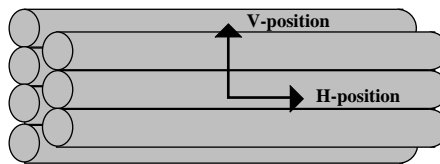


Figure 3.27: Definition of coordinates.

For the track reconstruction at least 7 hits are required in the silicon detectors. To get the position of the hits in the chamber, the track is extrapolated from the silicon telescope to the chamber. The distance from the silicon telescope to the chamber was minimized to reduce the multiple scattering which will cause errors in the extrapolation of the hit position in the chamber.

Experience gained in the first test beam with the Moscow prototype, which was the first prototype delivered, led to improve results in the second beam time. For the Dubna prototype the gas used was changed to have a faster and more linear gas and the electronics was more modern and specially designed for these chambers. Therefore we will report in the following mostly on the results obtained for the Dubna prototype.

## Resolution

To measure the resolution the following method was used. Plotting in a 2 dimensional histogram, the vertical position (calculated from the silicon telescope) as  $x$  axis and the drift time as  $y$  axis, a so called V-plot is obtained. The V shape is caused by the fact that the same drift time could correspond to two different positions in the straw, one on the left side of the wire, the other on the right side of the wire. The crossing of the 2 V legs corresponds to the wire position. The upper parts of the V correspond to the walls of the straw. Figure 3.28 is an example of a V-plot for a 10 mm straw. The V plot corresponds to the  $r(t)$  relation. The  $r(t)$  relation was simulated using the GARFIELD [15] simulation package to check if it corresponds to what is expected for  $\text{Ar}/\text{CO}_2/\text{CF}_4$ . The results of this simulation are shown in figure 3.29. GARFIELD is a simulation program for gaseous detectors.

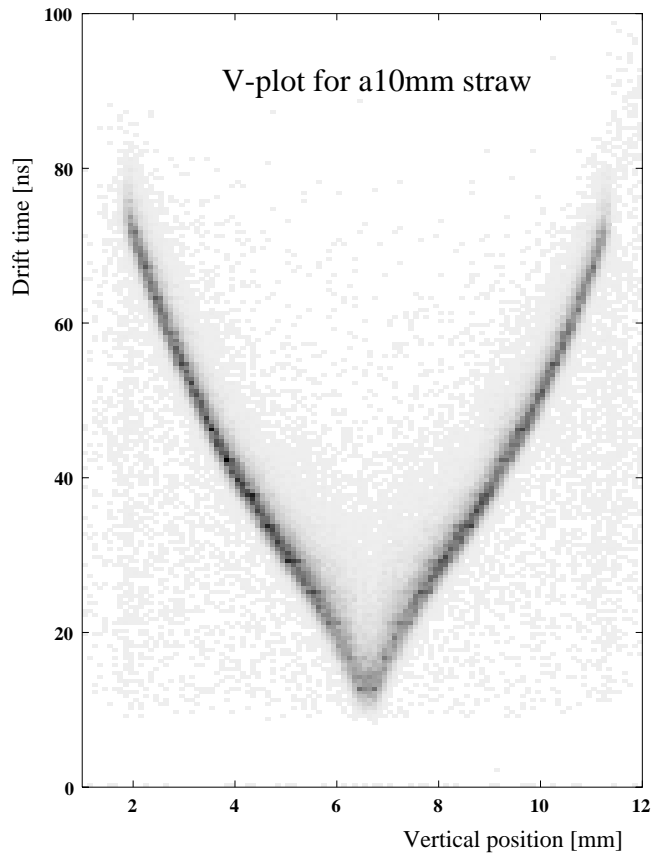


Figure 3.28: V-plot for a 10 mm straw.

The V-plot gives already some information about resolution and gas properties. Some parts of the V legs are broader. In this case the resolution is worse, as will be shown later. The straightness of the V legs indicate the linearity of the gas.

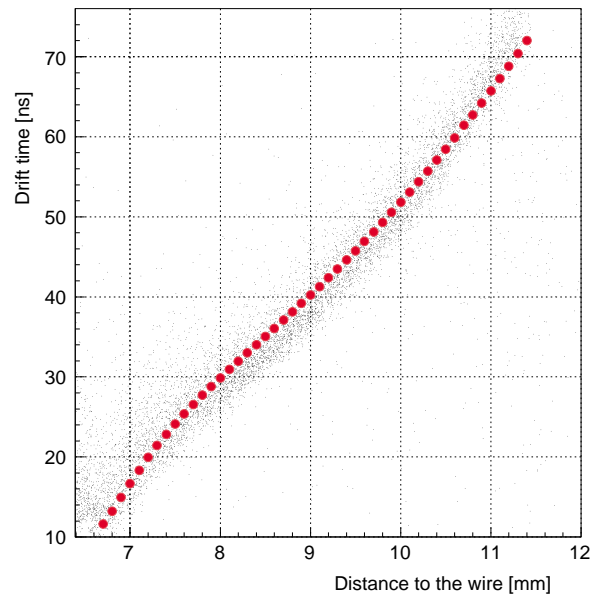


Figure 3.29: One of the V-legs for a 10 mm straw. The dots in gray correspond to the simulated  $r(t)$  relation using the GARFIELD simulation package.

To give quantitative results for the resolution a time window of 0.3 ns was chosen (see figure 3.30), and only one "leg" of the V-plot was considered. The vertical position is plotted as  $x$  axis and the number of events as  $y$  axis. Fitting this plot with a Gaussian, the corresponding sigma is our spatial resolution. The time window was chosen always to be 0.3 ns leading to an intrinsic error for the resolution measurement of  $\sim 20 \mu\text{m}$ .

This method does not give an exact number for the resolution because the Gaussian fit is not always the most suited but nevertheless gives a good approximation.

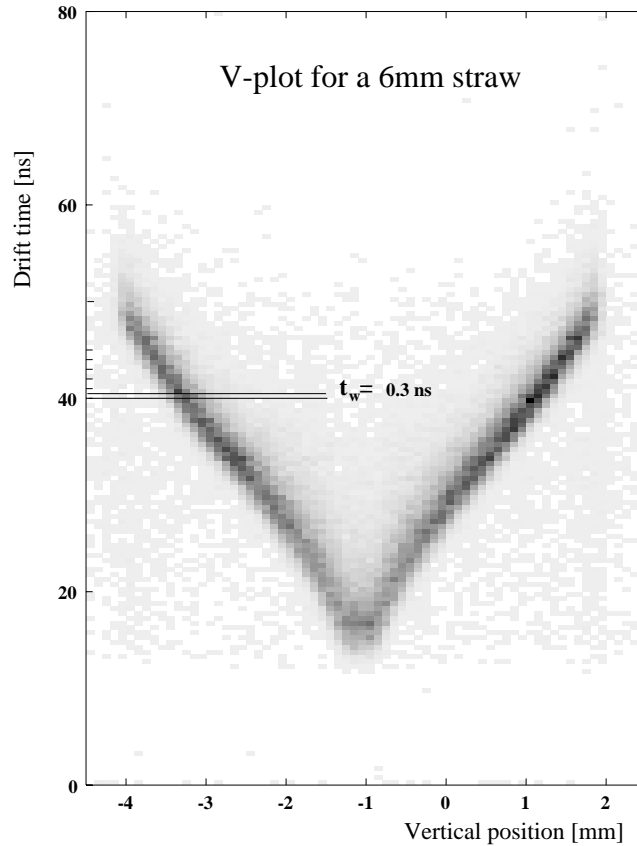


Figure 3.30: V-plot for a 6 mm straw.

The resolution was measured for both 10 mm and 6 mm straws.

The resolution depends on the drift time or distance to the sense wire. Figure 3.31 shows the resolution for a 10 mm straw for 2 different drift times. The resolution is worst for a drift time of 35 ns. There the V leg is the broadest.

The V leg gets thinner and better defined close to the wall. This is a consequence of the resolution dependence on the distribution of ionization products along the path of the particle.

A minimum ionisation path is needed to create enough electron-ion pairs to create a signal from a charged particle traversing the straw. The electron-ion pairs produced will be situated somewhere between points 1 and 3 (see figure 3.32) for a charged particle traversing the straw close to its wall and between points 1' and 3' for a charged particle traversing the straw close to its wire. When the track is close to the wall, the difference between the expected drift distance  $a$  (from position 2 in figure 3.32) and the real drift distance  $b$  (electron ion pair produced at position 1) is small. When the difference between the drift distances is small, the difference between drift times is also small. For tracks

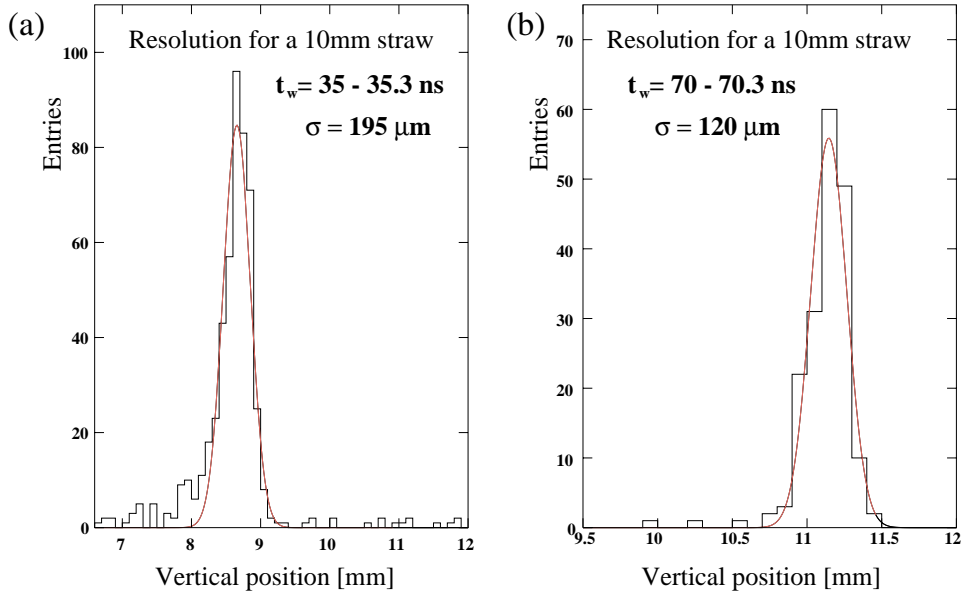


Figure 3.31: Resolution for a 10 mm straw for a time window of (a) 35-35.3 ns (b) 70-70.3 ns.

close to the wire, this difference (between a' and b') becomes larger. This implies that the resolution for a track passing close to the wire will be worse than this for a track close to the wall.

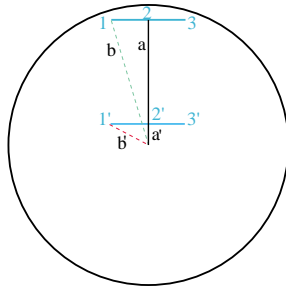


Figure 3.32: Ionisation path needed to produce enough electron ion pairs for the signal development, close the wire (from point 1 to point 3) or close to the wall (from point 1' to point 3') (see text).

Figure 3.33 shows the resolution for a 6 mm straw for 2 different time windows, one near the wire, and the other one far away.

The values of the different resolutions for different drift distances to the wire were measured and are plotted [53] in figure 3.34. The plot also shows the values of the simulated resolutions using the GARFIELD [15] package. As can be seen the measured results agree nicely with the simulated ones.

The values shown here correspond to the intrinsic resolution of a straw without considering the absolute wire position and the calibration of the chambers.

## Efficiency

The chamber was defined to be efficient when, having 7 hits in the silicon detectors, the straw drift chamber had at least one hit. The efficiency across the straw was given by the

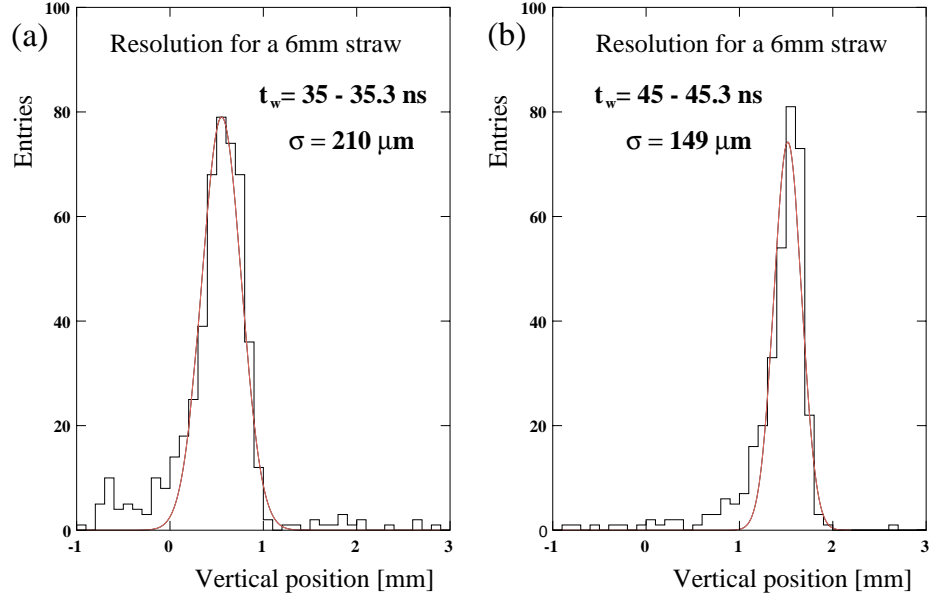


Figure 3.33: Resolution for a 6 mm straw for a time window of (a) 35-35.3 ns (b) 45-45.3 ns.

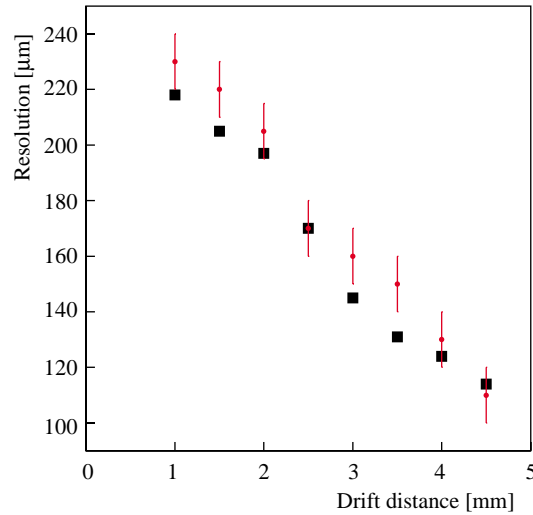


Figure 3.34: Comparison of simulated (squares) and measured resolution (dots) for a 10 mm straw at various drift distances to the wire.

ratio of a valid TDC hit (no overflow) and the beam flux through the straw measured by the silicon detectors. Technically this was achieved by dividing 2 histograms. Histogram number 1 contains the number of events versus vertical position independently of whether there was an overflow or not. Histogram number 2 contains only those events which have a TDC entry without overflow corresponding to a registered hit in the straw. Dividing 2 by 1 the efficiency is obtained.

Very good results were obtained for the efficiencies for both 10 mm and 6 mm straws. Values of 99% were achieved for all measured straws. Figure 3.35 shows the typical efficiencies obtained for a 10 mm and for a 6 mm straw working at the nominal HV (1850 V for the 10 mm and 1650 V for the 6 mm) corresponding to a gas gain of  $2 \cdot 10^4$ .

Near the wall, a particle passing through the straw will create less electron-ion pairs.

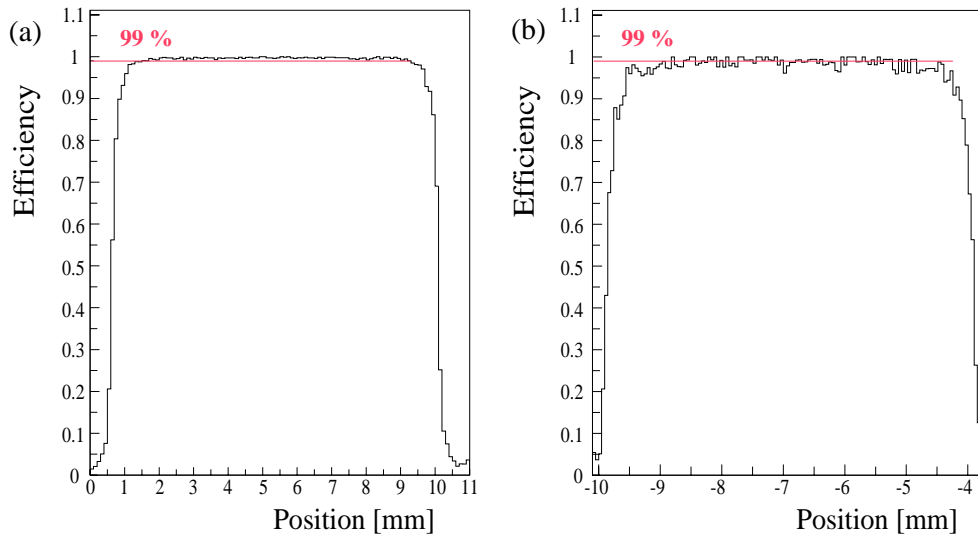


Figure 3.35: (a) Efficiency for a 10 mm straw and (b) Efficiency for a 6 mm straw.

This number could be smaller than the threshold of the electronics is set to. Thus the straw will be considered inefficient, no signal will be recorded. The efficiency near the walls is also affected by the position resolution. Figure 3.36 shows how the efficiency of the 10 mm straws decreases near the wall.

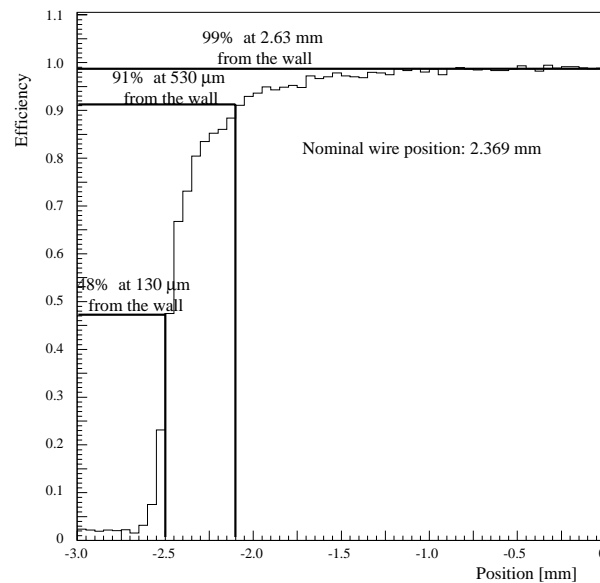


Figure 3.36: Efficiency for a 10 mm straw near the wall.

A minimum ionisation path is needed to create enough electron ion pairs for detecting the signal. For a track passing close to the straw wall, the efficiency of detection is smaller for a 6 mm straw than for a 10 mm straw. This is due to the fact that for smaller diameters the track path is sometimes smaller than this minimum ionisation path. Thus, the number of electron ion pair produced is not enough to detect the signal.

### Effects of the spacers

Spacers are placed inside the straws to keep the wire in place. The spacer is a small piece of non-conductive material with one hole in the middle for the wire of  $100\ \mu\text{m}$  diameter, and other holes allowing the flow of the gas. The diameter of the spacer corresponds to the inner diameter of the straws. The spacer is glued to the wire and then inserted into the straw.

The spacers inside the straws cause a distortion of the electric field leading to an inefficient zone in the straws. This dead zone was analyzed by plotting the efficiency as a function of the hit position along the wire. The spacer causes a drop in the efficiency. The width of the dead area is more or less the diameter of the straws. Figure 3.37 shows an example for a 10 mm straw.

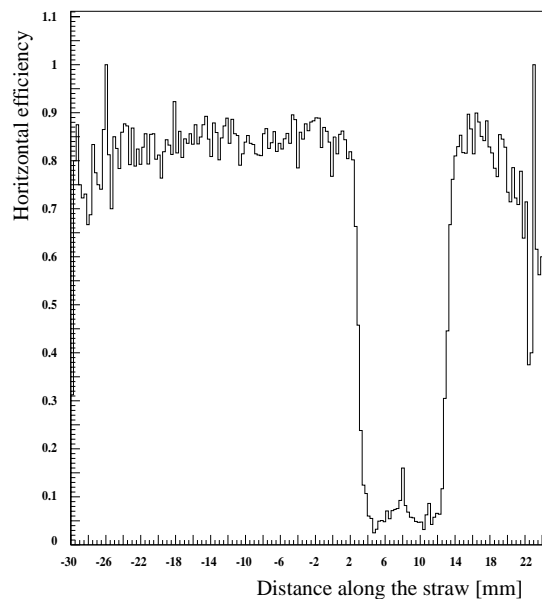


Figure 3.37: Efficiency in the region of the spacer as a function of the hit position along the wire for a 10 mm straw.

### 3.3.5 Conclusions of the tests

With the help of these prototypes it has been demonstrated that the straw detectors can be used as high resolution tracking elements for the COMPASS experiment. Average spatial resolutions of the order of  $150\ \mu\text{m}$  were obtained during the tests. The gas mixture of Ar/CF<sub>4</sub>/CO<sub>2</sub> (74:20:6) provides a fast linear gas for straw chambers. Efficiencies greater than 99 % were achieved. The tests of the prototypes determined the working point for the upcoming chambers, the gas gain, the preamplifiers threshold and the gas mixture at which the chamber has better efficiency and resolution.

### 3.3.6 Construction of a third prototype

A third prototype straw drift chamber was constructed at CERN. The design of the chamber was different from the one of the Dubna and Moscow prototypes. The Dubna design is based on gluing the straws together forming a plane. The plane of straws is glued

to the frame. Some carbon strips are placed on the side of the planes, perpendicular to the straws, to maintain the plane in position avoiding bendings.

The Moscow design differs from the Dubna design. The Moscow prototype used carbon fibre jigs. Holes are machined in them of the size of a straw diameter. The frame held the jigs and the straws were inserted through the holes of the jigs from one side of the frame to the other side. The advantage of this design is that almost no glue is present and every straw is an individual unit. The straws are free from one end and fixed in the other end. In this case, the straw is free to expand when affected by humidity. The frame was made of carbon fibre. The advantage of a carbon fibre frame is the low expansion coefficient compared to that of aluminium.

The design of the prototype constructed at CERN was similar to the Moscow prototype. It was also designed with the idea of using jigs. The horizontal size of the chamber was like the one for the final chambers, 3250 mm. The straws consisted of Kapton XC with a layer of aluminized mylar in the outside. This material corresponds to the one chosen for all TS2, except the one of the first submodule which will have as outer layer planar Kapton. The spacers were provided by our Dubna colleagues, and had the same design as the ones chosen for TS2 (see section 3.4). The sense wire was 30  $\mu\text{m}$  gold plated tungsten with rhenium, identical to that chosen for TS2. The endplugs were produced by a company according to a special design. The design of the endplugs was optimised to introduce as little material as possible. The design of the frame was basically the same as the one planned for the rest of TS2. The frame was constructed at CERN with a precision in assembly of the order of 50  $\mu\text{m}$ . The jigs had to be machined out of aluminium all at the same time to achieve the required precision on the holes position. With the help of an optical level all the jigs were aligned with respect to each other. The spacers were glued to the wires at the right position and then pulled into the straws. The tension applied to the wire was 100 g.

This prototype was constructed for several reasons. The first argument was to test the new straw material. Straws constituted of Kapton XC and aluminized mylar of 3250 mm length were never tested before. Another motivation was to find a different way of building a high precision straw tube drift chamber. This construction was supposed to be faster than the Dubna procedure of building the chambers. Another reason was the pilot run foreseen in COMPASS for July-August 2000. The requirement for the run was the presence of all type of detectors. The chambers in Dubna were not ready at that time and the only possibility was this prototype.

The prototype was installed in the COMPASS hall downstream of the SM1 magnet, corresponding to the nominal position of TS2. It was equipped only with few working channels, since not all were available. These were enough to test the long straws and the chamber performance in real conditions, including the presence of a magnetic field.

The 10 mm straws were studied at two different positions. First they were tested very close to the beam and then at their nominal distance to the beam, 18 cm. Figure 3.38 shows the layout of the straws.

The chamber was equipped with a motherboard identical to the one that will be used in the final straw chambers of TS2. Only a prototype of front end card existed. The prototype was working with the gas mixture chosen for the straw chambers in COMPASS: Ar/CF<sub>4</sub>/CO<sub>2</sub>. The 10 mm straws were operating at 1950 V corresponding to a gain of  $5 \cdot 10^4$ . No high voltage trips were observed. A solution had to be found for a proper grounding of the chamber. The oscillations and noise did not allow the electronics to work

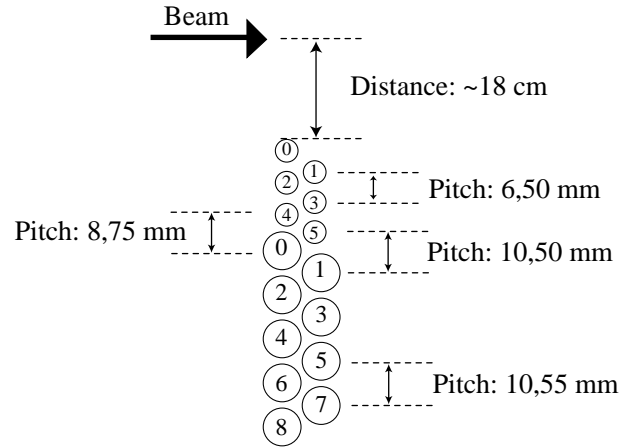


Figure 3.38: Straws layout for the pilot run of COMPASS.

with the expected thresholds. The chamber appeared to be very sensitive to activities in the area, which increased the noise level of the chamber.

The aim of the tests was to learn about the possibility of working with these straws and the whole setup together: straws, motherboards and front end electronics. When running without problems, the beam profile can be seen from the data, as shown in figure 3.39.

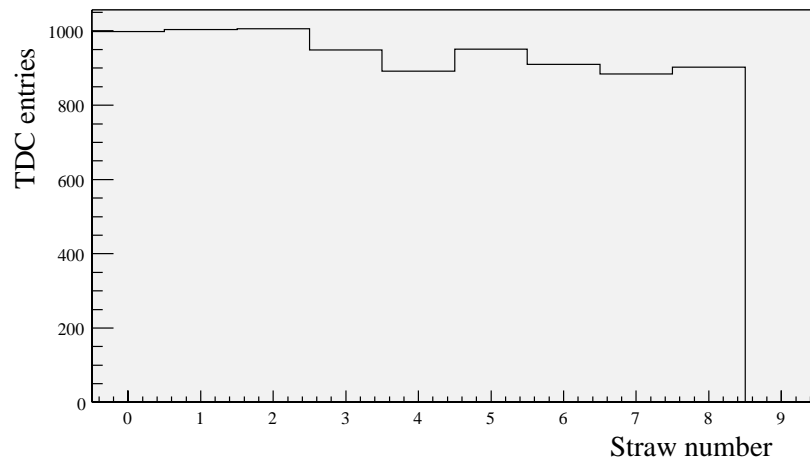


Figure 3.39: Profile of the beam given by the counts in the straws.

The positions of the straws are indicated in figure 3.38. The 10 mm straw closest to the beam, straw number 0, is the straw which has the higher counting rates.

When the chamber was noisy, the straws at the ends (straw number 0 and straws 7 and 8) distorted the beam profile. The noise problems were also seen in the TDC spectra (see figure 3.40).

The threshold for the preamplifier in this case was increased to the value of 1500 mV corresponding to  $\sim 9\text{fC}$ . Lower thresholds for the preamplifier caused some noise problems. Only some runs could be taken with thresholds of 1200 mV corresponding to  $\sim 6\text{fC}$ .

The results of the tests demonstrated that the 3250 mm long straws made of Kapton XC and an outer layer of double sided aluminized mylar work. The full read out chain, motherboard and front end card, worked as expected. The problem of the grounding and noise should be further investigated for the chambers with the final design.

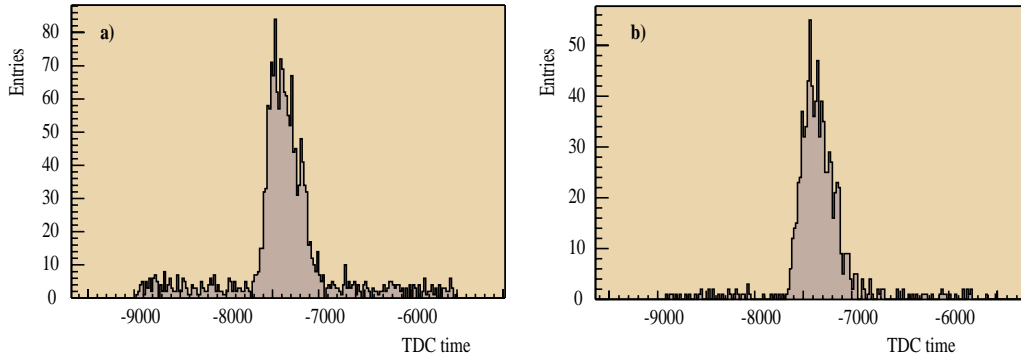


Figure 3.40: TDC spectra for 2 channels a) for a noisy channel and b) for a working channel without problems.

### 3.3.7 Full size "prototype" double layer

The first double layer of TS2 arrived at CERN in November 2000. The design of this double layer is described in section 3.4.3. The chamber was installed in a support frame which was initially constructed for the X-ray facility. The first test performed in the chamber was to check that the chamber could hold the high voltage. A second test with an iron source was performed to verify that the chamber did not suffer any damage during its trip from Dubna to CERN. A more detailed test was performed at the T9 test beam area at the PS at CERN. The setup for the test was the following: two scintillating fibre stations with two different fibre orientations were installed upstream and downstream of the chamber. Very close to the chamber a silicon microstrip detector was mounted. The support structure for the chamber allowed its vertical and horizontal movement. The aim of this test was to study the uniformity of calibration of the chamber. For this purpose, data were taken at several points. The points were strategically distributed in the chamber as shown in figure 3.41. They were chosen for the following reasons: points 1 to 5 (see figure 3.41) to check that the calibration for the 10 mm straws should be the same along the straw and for the different 10 mm straws. For the points from 6 to 10 the same reasons apply but in this case for the 6 mm straws. The points from 11 to 13 were chosen to check the response of a straw in the physical hole region since the straws in this region are shorter, and have a different gas connection than the others.

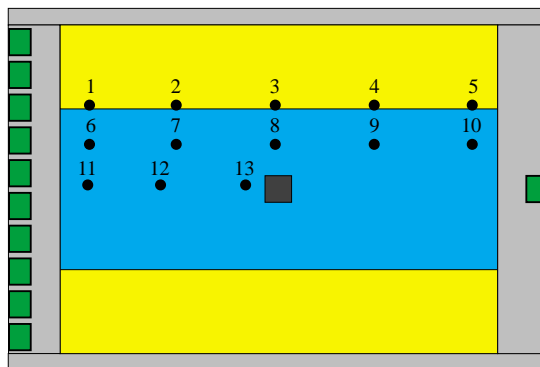


Figure 3.41: Measuring points in the chamber. These points were chosen to study the homogeneity of calibration.

The new read out cards, the ones planned to be used for the TS2, were installed.

Their performance was not as expected. This encouraged our colleagues from Freiburg to modify the final design. The "old" read out cards were finally used. In these cards, the ASD8b chips are installed on the card but not the TDC. The results were obtained using this "old" read out card. Nevertheless some data with the "new" read out card was also taken to be able to analyze the problems.

The chamber was connected to an oxygen sensor to determine the oxygen content inside the chamber.

The chamber was operative over its all surface. The efficiency for the 10 mm straws was 99% or higher. No efficiency drop was observed when measuring along the straws. The efficiency for the 6 mm straws was lower than the one measured for the 10 mm straws. A possible explanation was that a lower gas gain was used for the 6 mm and the 10 mm straws. Resolutions of the order of 220 to 300  $\mu\text{m}$  were obtained for the 6 mm straws and of the order of 240 to 170  $\mu\text{m}$  for the 10 mm straws. These values did not strongly depend on the position of the measurement along the straw. Some exceptions were found for positions close to the read out side. In these cases the resolution was slightly better.

## 3.4 Final design

### 3.4.1 Components

After the R&D, the different components of a double layer were determined. Their design is here presented.

The structure of the straw wall is composed as follows: aluminized mylar (on both sides) as an outer layer + glue + carbon loaded Kapton (or Kapton XC) as inner layer. The total thickness of the wall is 60  $\mu\text{m}$ , 40  $\mu\text{m}$  of Kapton XC + 8  $\mu\text{m}$  glue + 12  $\mu\text{m}$  aluminized mylar. Figure 3.42 shows a layout of the wall cross section.

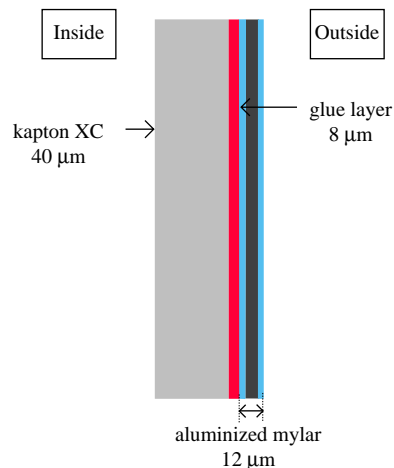


Figure 3.42: Schematic layout of the straw wall.

The spacers are situated inside the straws every 60 cm to keep the gravitational sag and offset of the wire small. For the spacer [68] a hole for the wire 100  $\mu\text{m}$  in diameter is made in the centre. Several other holes are existing for the gas flow (see figure 3.43). The shape of the spacer was designed to minimize the material required.

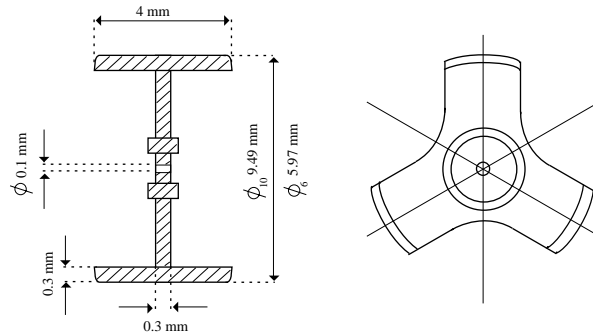


Figure 3.43: Side and front view of a spacer. The dimensions are equal for the 6 mm and the 10 mm straws, except for the dimensions which have a subindex indicating to which straw diameter they belong to.

The end-plug [68] (see figure 3.44) has a hole of 1.5 mm to accommodate a high precision pin. This pin has a hole of  $80 \mu\text{m}$  where the wire will be inserted. After its insertion, the wire will be tensioned and crimped. The wire is thus kept in the centre of the straw. An extra hole is placed in the end-plugs for the gas flow into the straws. The end-plugs provide also the straws with a ground contact. This is achieved by means of a Bronze-Beryllium spring placed around the end-plug touching the cathode.

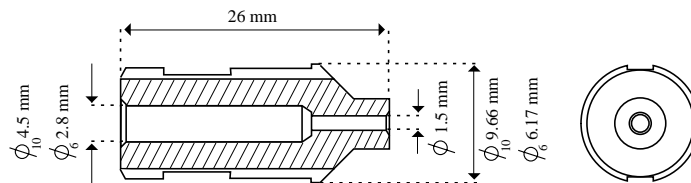


Figure 3.44: Side and front view of an end-plug. All the dimensions are equal for the 6 mm and the 10 mm straws, except for the dimensions which have a subindex which indicates to which straw diameter they belong to.

At the physical hole, every straw will be cut in two parts leaving the central part without material. The end-plug at the side of the physical hole will be slightly different from the rest of the end-plugs. The design is optimized to minimize the amount of material in this region. See figure 3.45 for a sketch of the physical hole.

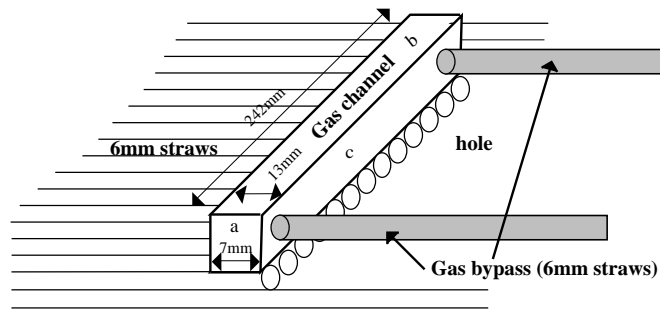


Figure 3.45: Sketch of the physical hole.

The gas is transferred from one part of the straws to the other by a bypass. The by-pass is a 6 mm straw cut to the right length. The straws are connected to a gas channel. This

is made out of stesalit. Its thickness is 1 mm in the long sides except for the side named *b* which is 0.5 mm. The thickness of the shorter sides is 1.5 mm. A small steel tube, with a thickness of 200  $\mu\text{m}$  and a length of 6 mm, leads the gas of the straw to the gas channel.

### 3.4.2 Precision required

A geometrical precision of 200  $\mu\text{m}$  is required for the chambers on TS2. To fulfil this requirement, a high precision in the construction process is needed. The following specifications were requested to ensure the precision of the chambers:

- the sagitta of the wires should be smaller than 50  $\mu\text{m}$  in the wire plane
- the deviation of flatness should be smaller than 200  $\mu\text{m}$
- the error on the wire positioning should be smaller than 50  $\mu\text{m}$  with respect to the alignment marks
- the eccentricity of the wires relative to the straws should be smaller than 50  $\mu\text{m}$ .

To obtain the precision in the wire position a certain tension on the wire should be applied. The tension was chosen to be 100 g. Higher values could cause a loss of elasticity or even the breaking of the wire. A lower wire tension has two drawbacks, the gravitational sagging of the wire and the additional deflection caused by the electrical field. In the ideal case, the sense wire is exactly centred within a perfectly cylindrical cathode. In this case, the system is electrostatically stable. However, the sense wire will never be exactly centered due to positioning error and gravitational sag. For the straw tube cathode, similar problems will be encountered since the straw will be neither perfectly cylindrical nor perfectly straight. The gravitational sag of the wire can be estimated from the following equation:

$$d_g = \frac{L^2 \cdot \rho \cdot g}{8 \cdot T} \quad (3.11)$$

where  $L$  is the length of the wire,  $\rho$  its weight per unit of length.  $g$  is the gravitational acceleration and  $T$  the stretching force or tension applied to the wire.

The deflection caused by the electrical field can be estimated using an approximate formula [21]:

$$d_e = \frac{L^2 \cdot F_e}{8 \cdot T} \quad (3.12)$$

where  $F_e$  is the electrostatic force per unit of length. The electrostatic force per unit of length due to an offset  $\delta$  of the sense wire in the straw tube is given by [21]:

$$F_e = \frac{2 \cdot \pi \cdot \epsilon_0 \cdot V^2 \cdot \delta}{R^2 \cdot (\ln \frac{R}{r})^2} \quad (3.13)$$

where  $V$  is the sense wire potential,  $\delta$  is the initial wire offset from the centre of the straw tube,  $R$  is the radius of the straw tube cathode,  $r$  is the radius of the sense wire and  $\epsilon_0$  is the electric permittivity of the chamber gas.

Using  $F_e$  previously defined, the deflection  $d_e$  can be written as [21]:

$$d_e = \frac{2 \cdot \pi \cdot \epsilon_0 \cdot L^2 \cdot V^2 \cdot (\delta + d_e/2)}{8 \cdot T \cdot R^2 \cdot (\ln \frac{R}{r})^2} \quad (3.14)$$

$d_e/2$  is added to  $\delta$  to take (approximately) into account the additional force due to the wire deflection  $d_e$ .

The deflection due to gravitational sagging in our specific case is  $10.8 \mu\text{m}$  for both 10 and 6 mm straws. It was calculated taking the density for a  $30 \mu\text{m}$  gold plated tungsten wire and multiplying it by its cross section. The tension applied to the wire will be of 1 Newton and the length  $L$  of the wire will be of 80 cm. This distance corresponds to the separation between spacer elements that keep the wire in place.

The sagging due to gravitation is not the only offset of the wire. The spacer has a hole for the wire of  $100 \mu\text{m}$  thus, due to gravitational sag, the wire will not necessarily be placed in the centre of the spacer. It can sit on the edge of the hole of the spacer, after the spacer has been glued to the wire. This will introduce an extra offset of  $35 \mu\text{m}$ . The total offset will be of  $45.8 \mu\text{m}$ . The electrostatic force per unit length can be calculated in our case using the formula 3.13. For a 10 mm straw diameter operating at 1950 V and for the offset just calculated, the force obtained is of  $1.15 \cdot 10^{-5} \text{ N/m}$ . For the 6 mm straw operating at the same gain, (1780 V) the electrical force is of  $3.14 \cdot 10^{-5} \text{ N/m}$ . Finally the deflection of the wire due to electrostatic forces can be computed using the formula 3.12. The result can be compared to the one obtained when using the formula 3.14. The deflection due to the electrical field obtained for a 10 mm straw using the formula 3.12 is in the order of  $1 \mu\text{m}$ . For a 6 mm straw is in the order of  $2.5 \mu\text{m}$ . By using the formula 3.14 the results obtained were approximately the same since the correcting factor of  $d_e/2$  is very small.

The total deflection for the wire of a straw will be the deflection caused by the gravitational sagging plus the deflection due to the electrical field. For a 10 mm straw it will be in the order of  $47 \mu\text{m}$  and for a 6 mm straw  $48 \mu\text{m}$ .

For minimising the errors in precision inside the plane the construction method is as follows: high precision balls are inserted into the straws placed on a high precision table. The balls are used to glue the straws together with no deformation. Once the straws are glued together forming one plane, this is glued to the frame. All this will be explained in more detail in the next section. This process will allow to reach the required resolution for the tracking station 2. A more detail description of the production process will be given in the next section.

To check the precision and position of the wires relative to each others and relative to the frame, an X-ray stand has being produced [51]. It consists of an X-ray source and a CCD camera. The chamber will be mounted on a support structure and it will be X-rayed. The X-ray source and the CCD will be moved by a motor to scan the whole chamber. The wires can be seen in the picture stored in the CCD. The precision of the measurements that can be obtained is approximately  $10 \mu\text{m}$ . The precision in the chamber construction can be checked measuring at the spacer positions the distance between the wires (for 10 and 6 mm straws) and the parallelism of the wires when passing from the 10 mm to the 6 mm. A mapping of the absolute position of the wires can be done by attaching to the

chamber in a precise position a high precision calibrated ruler. All the wire positions with respect to the ruler are stored in the CCD.

### 3.4.3 Assembly

The assembly method plays a very important role for the precision of the chamber, for the speed of the mass production, for the size of the production area and the costs. The errors in precision inside the plane had to be minimized. The method of construction was developed by our Dubna colleagues. Only some critical issues, as the amount of material introduced by the chambers in the COMPASS detector, lead to long discussions on the gluing method. After receiving the first prototype, it was decided that the COMPASS straws should only be glued at few points, not all over its surface. The spacer elements were also discussed. Other details like the gas distribution in the chamber, the end plugs and the physical hole were discussed among the straw group, JINR, MSU, Freiburg University, Warsaw University of Technology and LMU-Munich. A new design to minimize the amount of material introduced by these elements was agreed upon all the institutes involved in the straw project.

The assembly method that is being used is the following:

- A big production area 270 m<sup>2</sup> was constructed in Dubna.
- The straws are manufactured by an English company, Lamina, and shipped to Dubna.
- Once the straws arrive in Dubna their shape and diameter are checked. The straws which do not fulfil the requirements are discarded.
- The selected straws are placed on a high precision table which will provide the necessary precision to the straw plane.
- High precision steel balls are inserted inside the straws with the help of a ball insertion machine. This machine is capable of filling one straw with balls in 60 s.
- With the straws filled with balls, one straw is pushed against the other with the help of a high precision ruler.
- Once enough straws for a single layer are on the table, they are glued together. This will give some stability to the plane. The glue mass is about 35% of the mass of the straws. Figure 3.46 shows the gluing process.
- The physical hole is then cut on the layer and the structure of the hole is glued.
- Once one single layer is finished the procedure starts again for the second layer of the plane.
- The two layers are then put together shifted by half a diameter between them forming the double layer. In between a carbon strip is placed so that the two single layers are not touching each others.
- In parallel, the wires are being prepared in some tables, the spacers are put in position along the wire and they are glued to it.

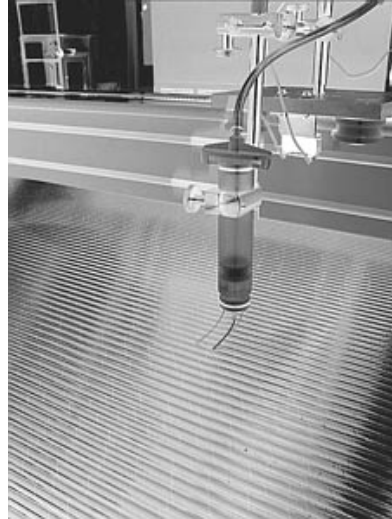


*Figure 3.46: Gluing the plane of straws.*

- After removing the balls from the inside of the straws, the double layer is glued to the frame.
- The process of wiring starts. The double layer is positioned vertically, and from the top the wires, with the spacers, are inserted into the straws by means of a weight attached to the ends of the wires.
- The wires are then crimped on the top, and then crimped with a certain tension on the bottom.
- Once this process is finished, the installation of the periphery can start. That means that the motherboards and front end card are installed.
- The chamber, when finally finished, will be tested at high voltage and for gas tightness. The final test will be to test the straws with a  $\text{Fe}^{55}$  source.
- The chamber will be shipped to CERN where further tests will be done, like the X-ray measurements, wire tension and again some tests with a  $\text{Fe}^{55}$  source will be performed.

After the assembly and before starting the tests, the double layer looks as shown in figure 3.47.

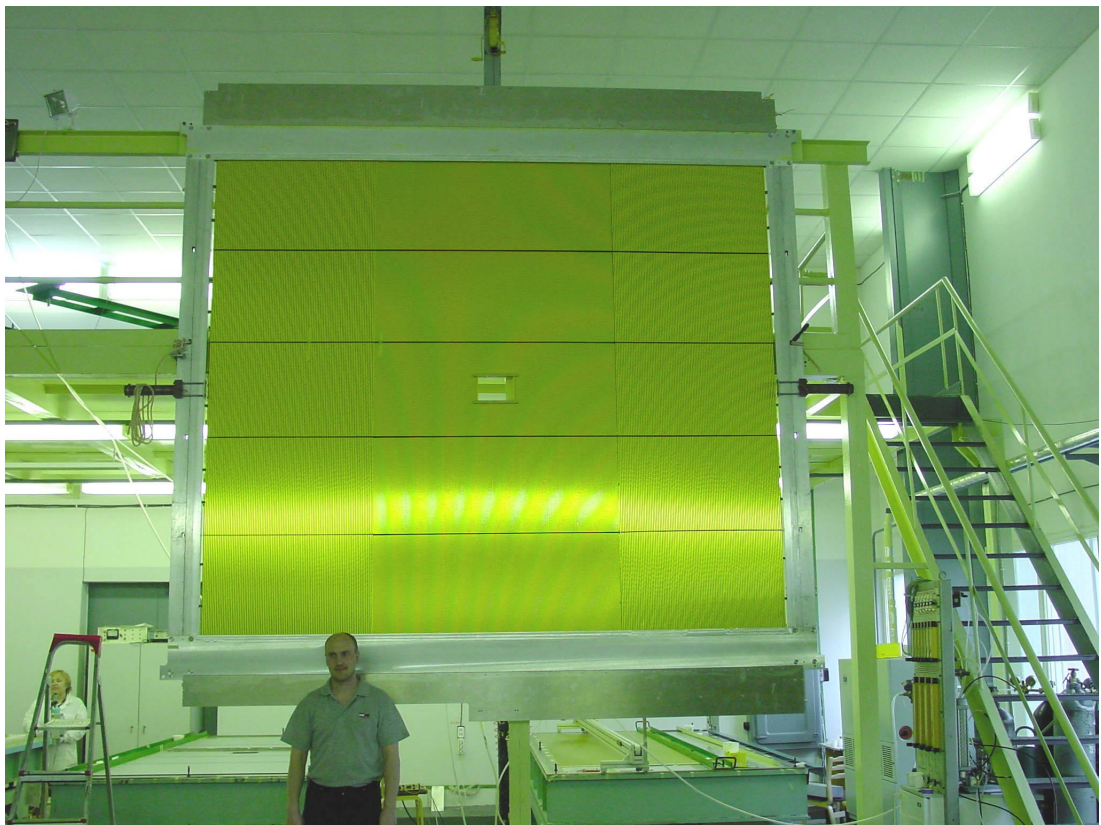


*Figure 3.47: Double layer before the testing.*

<i>Straw detector</i>	<i>Geometry</i>	<i>Number of straws</i>	$\emptyset_s$ [mm]	<i>Length</i> [cm]	<i>Wall material</i>	<i>Total thickness of wall</i> [μm]	<i>Wire material</i>	$\emptyset_w$ [μm]
MARKIII [16]	cylindrical	640	8	400	Al-mylar	100	Au-Ag-W	50
MAC [17]	cylindrical	324	6.9	43.2	Al-mylar	100	Au-Ag-W	30
FINUDA* [18]	cylindrical		10±0.05	200	Al-mylar	30±10	Au-Ag-W	30
FINUDA [19]	cylindrical	2424	15±0.5	255	Al-mylar	30	Au-Ag-W	30
KLOE [20]		26	30	50	Al	500	Cu-Be	100
SSC* [21]	cylindrical	60	4	270	Mylar+Al	150+10	Au-Ag-W	10
SDC [22] [24]	cylindrical	141404	4	400	Cu-Kapton	33		
Jetset [25]	barrel	1400	8	43.6	Al-alloy	60±5	stainless-steel	35
ALEPH [26]	cylindrical	63	10	193	Al-mylar	54		
FPC [27]	rectangular	244	7.98±0.05	92	30±10		stainless-steel	35
TPC [28]	cylindrical		8		Mylar+Al	100+25		
KEDR [29]	cylindrical	306	10	80	Al-mylar	40		
NA31* [30]		32	8	240	Al-mylar	25	Au-Ag-W	30
HRS [31]	cylindrical		7±0.05		Al-mylar	85	Au-Ag-W	20
E760 [32]	cylindrical		5	21	Al-mylar	80	stablohm 875	19
AMY [33]	cylindrical	576	10	57.15	Mylar+Al-polycarbonate	12.5+12.5	Au-Ag-W	
ATLAS [34]	radial		4	55	Kapton+ Al	72	Au-Ag-W	50
CDF [35]	cylindrical	2016	12.7	300	Stainless-steel	200±10	stainless-steel	50
AMPIR* [36]	rectangular	12	6	160	Al-mylar	36	Au-Ag-W-Re	20

Table 3.1: Some of the characteristics of the straw detectors in the world.  $\emptyset_s$  and  $\emptyset_w$  stand for the diameter of the straw and the wire respectively. The \* indicates a prototype.

<i>Straw detector</i>	<i>Gas mixture</i>	<i>Pressure [atm]</i>	<i>Magnetic field[T]</i>	<i>Efficiency [%]</i>	<i>Resolution [<math>\mu\text{m}</math>]</i>	<i>Gas gain or voltage[V]</i>
MARKIII [16]	Ar/C <sub>2</sub> H <sub>6</sub> [50/50]	3	—		49	3900 V
MAC [17]	Ar/CO <sub>2</sub> /CF <sub>4</sub> [49.5/49.5/1]	4			45	3900 V
FINUDA* [18]	C <sub>2</sub> H <sub>6</sub> O [99.8%]	1.02			40	3200 V (10mm) 3500 V (20mm)
FINUDA [19]	Ar/C <sub>2</sub> H <sub>6</sub> ; Ar/CO <sub>2</sub> DME		1.1		100; 150 40	
KLOE [20]	Ar/C <sub>4</sub> H <sub>10</sub> [40/60]	1	—	99	60	4600 V
SSC* [21]	Ar/CF <sub>4</sub> /C <sub>2</sub> H <sub>6</sub> [33/33/33]		—		100	1800 V
SDC [23] [24]	CF <sub>4</sub> /C <sub>4</sub> H <sub>10</sub> [80/20]		2		145	2000 V
Jetset [25]	Ar/CO <sub>2</sub> [50/50]			92	180	10 <sup>5</sup>
ALEPH [26]	Ar/CO <sub>2</sub> /CH <sub>4</sub> [89/10/1]	2		96	180	1425 V
FPC [27]	Ar/CO <sub>2</sub> [50/50]			95	250	10 <sup>5</sup>
TPC [28]	Ar/CO <sub>2</sub>	4			35-50	
KEDR [29]	Ar/CO <sub>2</sub> [50/50] CO <sub>2</sub> /C <sub>4</sub> H <sub>10</sub> ; DME	1 2; 1	0 and 2		50 22; 20	10 <sup>5</sup>
NA31* [30]	Ar/C <sub>2</sub> H <sub>6</sub> [50/50]	2	—		100	2300 V
HRS [31]	Ar/C <sub>2</sub> H <sub>6</sub> [75/25]	1	1.62	92	100	1650 V
E760 [32]	Ar/CO <sub>2</sub> [87.5/12.5]	1	—	99		1-3·10 <sup>5</sup>
AMY [33]	Ar/C <sub>2</sub> H <sub>6</sub> [50/50]	1.45	3	97	80	2 to 4·10 <sup>4</sup>
ATLAS [34]	Xe/CF <sub>4</sub> /CO <sub>2</sub> [70/20/10]	1 to 1.4	0 to 2	87	145	2.5 to 4·10 <sup>5</sup>
CDF [35]			1.5			
AMPIR* [36]	Ar/CO <sub>2</sub> [70/30]	2 to 3		99		

Table 3.2: Some of the properties of the straw detectors in the world. The \* indicates a prototype.

# Chapter 4

## Physics simulations

### 4.1 Diffractive dissociation

An initial hadron programme in COMPASS could take place before all the detectors are installed. This chapter describes Primakoff and diffraction measurements, two of the physics programmes that could be performed in COMPASS at this early stage. Physics simulations concerning the feasibility of such programmes are presented in this thesis. The detector setup was carefully studied. It should be similar for both physics programmes in order to efficiently change in a short time from the hadron to the muon programme.

#### 4.1.1 General features of diffractive dissociation

The general features of diffractive dissociation processes and their cross-sections are described in this section.

Diffractive reactions are [45]:

- Elastic scattering of two particles, a and b:  $a b \rightarrow a b$ . The diagram of this reaction is shown in figure 4.1.I.
- Single inelastic diffraction, or diffractive dissociation, where one particle scatters inelastically taking energy and hadronizing into new particles X:  $a b \rightarrow a X$  or  $a b \rightarrow X b$ . One of the possible cases is shown in figure 4.1.II.
- Double diffractive dissociation, where both vertices are inelastic. Two new hadronic excitations are produced. This case is shown in figure 4.1.III.
- Double Pomeron exchange, where particles are produced in the central region, as shown in figure 4.1.IV.

Diffraction is described by the exchange of a Pomeron. The Pomeron transfers only momentum and angular momentum. No colour or flavour is transferred in this exchange. Inelastic diffraction corresponds to an exchange where the Pomeron-hadron interaction is inelastic at one vertex. The nature of the Pomeron is not clear, but it is likely to be a gluonic object [44] [65]. This gluon rich environment favours the production of glueballs and hybrids. Therefore diffractive dissociation is a possible way to search for glueballs and hybrids. In this thesis, we will concentrate on diffraction dissociation of the projectile. In

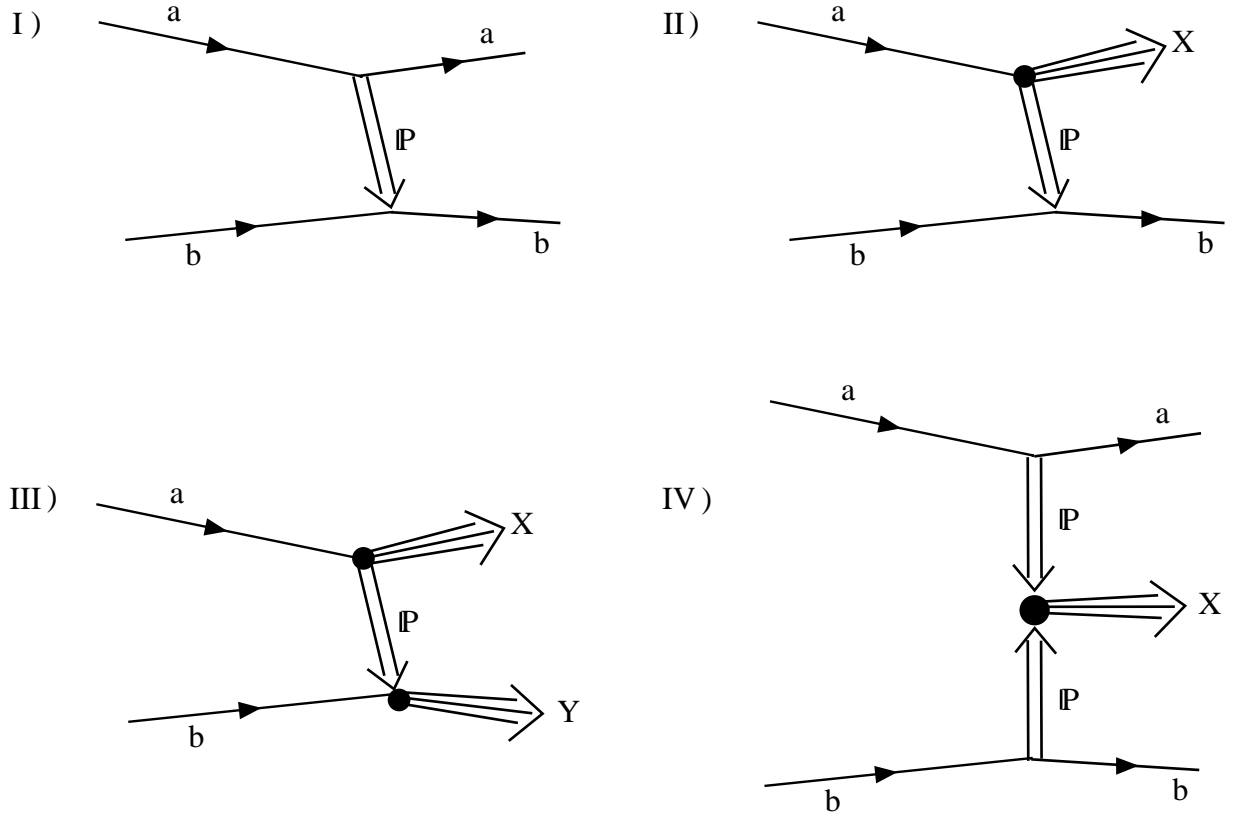


Figure 4.1: I) Elastic scattering, both vertices are elastic. II) Inelastic diffraction. Only one vertex is inelastic, represented in the figure by a black dot. III) Double diffraction. Both vertices are inelastic, represented in the figure by black dots. Two new hadronic excitations,  $X$  and  $Y$ , are produced. IV) Double Pomeron exchange. V) Diffractive dissociation of the projectile.

the case of interest, the inelastic vertex is on the projectile side and the target remains unchanged. This corresponds to the diagram shown in figure 4.1.II. It is also possible that the inelastic vertex is in the target and the elastic on the projectile side. In this case, it is called diffractive dissociation of the target.

From the point of view of kinematics, inelastic diffraction can be treated as a two body reaction if the final system  $X$  is considered as 'one particle'. The kinematics of the process will be studied in the section 4.1.2.

The differential cross-section for diffractive dissociation can be expressed as [44] [46]:

$$\frac{d\sigma}{dt \cdot dM_X^2} \sim e^{-bt} \cdot \frac{1}{M_X^2 - M_0^2} \quad (4.1)$$

where  $t$  is the four momentum transfer squared,  $M_X$  is the mass of the diffractively produced object  $X$  and  $M_0$  is the minimum mass that can be produced. Depending on the beam particle used in COMPASS, the mass  $M_0$  is the mass of the pion  $M_0 = m_{\pi^-}$  or the mass of the kaon,  $M_0 = m_{K^-}$ . The parameter  $b$  has different values for different target materials. For a proton target, the parameter  $b$  equals  $6.5 \text{ GeV}^{-2}$  (see [44]), while for lead,  $b$  equals  $400 \text{ GeV}^{-2}$  (see [2]).

### 4.1.2 Study of $\pi^- A \rightarrow (\pi^- \eta) A$ in COMPASS

In COMPASS several hadron beams are available:  $\pi^-$ ,  $K^-$  or  $p$ . A light material is needed for the target. In the initial hadron programme, a polyethylene target 10 cm in length (12 % of absorption length and 21 % of radiation length) will be used. Later, a liquid hydrogen target will be built.

The reaction of interest is the one shown in figure 4.1.II, where the particle labelled a will be a  $\pi^-$ , the one labelled b will be a proton and the labelled X could be a  $\pi^- \eta$  resonance. The reaction is:  $\pi^- p \rightarrow p X$ , where the diffractively produced system X will decay in  $X \rightarrow \pi^- \eta$  and where the channel of interest of the eta decay is  $\eta \rightarrow \gamma \gamma$ . The reaction of  $\pi^- p \rightarrow p \pi^- \eta$  is chosen primarily because of its simplicity. Another reason is that the Crystal Barrel experiment, at LEAR at CERN, found an exotic  $\pi^- \eta$  resonance, with  $J^{PG} = 1^{--}$ . The specific decay channel for the  $\eta$ :  $\eta \rightarrow \gamma \gamma$  was also chosen for its simplicity.

The beam energy in COMPASS will be 190 GeV. The maximum mass  $M_X$  of the diffractively produced object that can be obtained with this beam energy is  $M_X = \sqrt{s} - m_p$ , where  $\sqrt{s}$  is the centre of mass energy [38] and  $m_p$  is the mass of the proton. This gives a value of 17.96 GeV/c<sup>2</sup> for  $M_X$ . The minimum value for  $M_X$  is given by  $m_{\pi^-} + m_\eta = 0.7$  GeV/c<sup>2</sup>, where  $m_{\pi^-}$  and  $m_\eta$  are the masses of the pion and the eta, respectively.

#### Kinematics for diffractive dissociation

In this section, some kinetic variables for diffractive dissociation of the projectile will be introduced. The variables described correspond to the reaction:  $\pi^- p \rightarrow p X$ , where X decays into  $\pi^-$  and  $\eta$ .

The first kinetic variable,  $t$  the four momentum transfer squared, was mentioned above. It can be calculated for the proton as:

$$t = (\mathbf{p}_{i_p} - \mathbf{p}_{f_p})^2 \quad (4.2)$$

where  $\mathbf{p}_{i_p}$  is the initial four momentum of the proton at rest,  $\mathbf{p}_{i_p} = (m_p, 0, 0, 0)$  and  $\mathbf{p}_{f_p}$  is the final four momentum of the proton target. Its expression is  $\mathbf{p}_{f_p} = (E_p, p_{x_p}, p_{y_p}, p_{z_p})$  where  $p_{x_p}, p_{y_p}$  and  $p_{z_p}$  are the three components of the final momentum of the proton  $\vec{p}_p$  and  $E_p$  its energy. Substituting the values of  $\mathbf{p}_{i_p}$  and  $\mathbf{p}_{f_p}$  in equation (4.2), the following equation is obtained:

$$t = (m_p - \sqrt{p_p^2 + m_p^2})^2 - p_p^2 \quad (4.3)$$

Another interesting kinematic variable is the Feynman  $x_f$ , which is defined as:

$$x_f = \left( \frac{p_z}{p_{max}} \right)_{cm} \quad (4.4)$$

where  $p_z$  is the momentum in the  $z$  direction (the direction of the beam).  $p_{max}$  is the maximum momentum that can be obtained. In the centre of mass system of  $\pi^-$  and  $p$ , the total momentum  $p^{cm}$ , can be expressed as:

$$p^{cm} = \frac{\sqrt{[s - (M_X + m_p)^2] \cdot [s - (M_X - m_p)^2]}}{2 \cdot \sqrt{s}} \quad (4.5)$$

where  $M_X$  is the mass of the diffractively produced object X, and  $s$  is the centre of mass energy squared of the  $\pi^- p$  system. It can be calculated as:

$$s = m_{\pi^-}^2 + m_p^2 + 2 \cdot E_{\pi^-} \cdot m_p \quad (4.6)$$

$p_{max}$  is obtained when the energy available in the centre of mass system is only used as kinetic energy for both interacting particles and not to produce any other object (elastic scattering). It can be expressed as:

$$p_{max} = \frac{\sqrt{[s - (m_{\pi^-} + m_p)^2] \cdot [s - (m_{\pi^-} - m_p)^2]}}{2 \cdot \sqrt{s}} \quad (4.7)$$

After introducing equations (4.5) and (4.7) into equation (4.4) and performing some operations and approximations (for details see appendix B), the mass of the object X can be expressed as:

$$1 - x_f = \frac{M_X^2 - m_{\pi^-}^2}{s} \quad (4.8)$$

### Event generator

One way to test theoretical models is by comparing the real events with the events generated by a computer program with Monte Carlo procedures. The computer program generates the events (event generator) then simulates the interaction of the generated particles with the detectors and the detector response itself. Finally it reconstructs the events with the information given by the detectors.

In this section, we will concentrate on the program that generates the particles. The other two programs will be described in the following sections.

Two event generators were considered, one for non-diffractive interactions and another one for diffractive processes.

FRITIOF [37] is the name of the event generator that can be used for the generation of non-diffractive events. It simulates the interactions between hadrons and nuclei. It was first checked whether this event generator also describes the diffractive events. For this purpose the dependence of the cross-section with the four momentum transfer squared  $t$  was plot. It was found that the dependence of the cross-section with  $t$  in the region of  $t$  corresponding to diffractive processes did not follow the exponential distribution (see equation 4.1). This event generator could in principle only be used to generate all background processes of diffractive dissociation events. FRITIOF was used when simulating the rates in the straw chamber (see section 3.2.6).

For studying diffractively produced events an event generator was developed. The interaction of these events in the COMPASS detector was simulated. The results will

show the possibility of measuring diffractive dissociation in COMPASS. The performance of this event generator is described in the remainder of this section.

The following reaction was simulated:  $\pi^- p \rightarrow p X$ , where  $X \rightarrow \pi^- \eta$ . The p is at rest and the  $\pi^-$  projectile has an energy of 190 GeV. The beam has a 1.5 % momentum resolution and a RMS divergence at the target of  $0.29 \times 0.48 \text{ mrad}^2$  (For a description of the properties of the hadron beam in COMPASS see [47]).

From the expression of the differential cross-section for diffractive dissociation described in earlier sections (in equation 4.1) and considering the expression for Feynman x (see equation 4.6), the differential cross-section can be written as:

$$\frac{d\sigma}{dt \cdot dx_f} \sim e^{-6.5 \cdot t} \cdot \frac{1}{(1 - x_f) \cdot s} \quad (4.9)$$

To simulate the events, the variables  $t$  and  $x_f$  are randomised following the distributions  $e^{-6.5 \cdot t}$  and  $\frac{1}{1-x_f}$  respectively. Figure 4.2 shows the randomisation of the variable  $t$ .

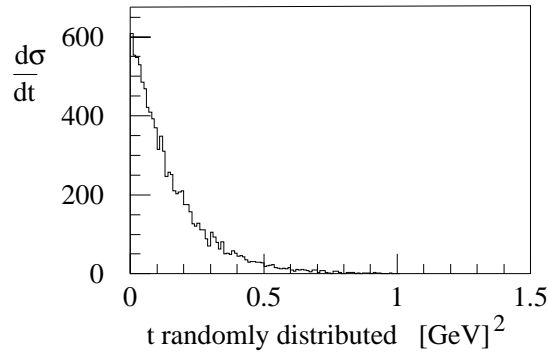


Figure 4.2: Simulated differential cross-section for diffractive dissociation as a function of  $t$ .

The angle  $\varphi$  is uniformly randomised between 0 and  $2\pi$ . The interesting values of  $x_f$  are in the range of:  $0.988 \leq x_f \leq 0.998$ . These values correspond to masses of the X object covering the range:  $0.83 \text{ GeV}/c^2 \leq M_X \leq 2.02 \text{ GeV}/c^2$ . With these variables, the transverse momentum of the proton in the laboratory system can be calculated as:

$$\vec{p}_{\perp p} = x_f \cdot \sqrt{|t|} \cdot (\sin \varphi, \cos \varphi) \quad (4.10)$$

The longitudinal momentum of the proton can not yet be calculated since it depends on the mass of the object X,  $M_X$ .  $M_X$  can be computed via the equation (4.8). Then the transverse momentum of the object can be calculated as:

$$\vec{p}_{\perp X} = \vec{p}_{\perp beam} - \vec{p}_{\perp p} \quad (4.11)$$

where  $\vec{p}_{\perp beam}$  is the transverse momentum of the beam.

Returning to the kinetic variables of the p, in the centre of mass system of the proton and the object X, the momentum of the proton can be calculated using equation (4.5). Then the longitudinal momentum of the proton, supposing that this moves backward in the centre of mass system (the case of interest) is:

$$p_{z_p}^{cm} = -\sqrt{(p^{cm})^2 - p_{\perp p}^2} \quad (4.12)$$

The longitudinal momentum of the proton in the laboratory system can be calculated by making a boost to the laboratory system. This operation leads to:

$$p_{z_p} = \frac{1}{\sqrt{s}} \cdot [(E_{beam} + m_p) \cdot p_{z_p}^{cm} + p_{z_{beam}} \cdot E_p^{cm}] \quad (4.13)$$

where  $E_p^{cm}$  is the energy of the proton in the centre of mass system of the proton and the object X. Here:  $E_p^{cm} = \sqrt{(p_{z_p}^{cm})^2 + p_{\perp p}^2}$ .

At this point all kinematic variables of the proton are determined. The next step is to calculate the missing kinematic variables of the object X. The longitudinal and total momentum of the object X in the laboratory system are:

$$p_{z_X} = p_{z_{beam}} - p_{z_p} \quad (4.14)$$

$$p_X = \sqrt{p_{z_X}^2 + p_{\perp_X}^2} \quad (4.15)$$

So far the system composed of the p and the object X is fully described. The next goal is to study the decay of the object X:  $X \rightarrow \pi^- \eta$ .

The first step is to study the decay of the object X in its centre of mass system. The momentum of the decay products (i.e. the momentum of the  $\eta$  and the momentum of the  $\pi^-$ ) can be calculated again with equation( 4.5), substituting the corresponding variables:

$$p_{products}^{cm} = \frac{\sqrt{[M_X^2 - (m_{\pi^-} + m_{\eta})^2][M_X^2 - (m_{\pi^-} - m_{\eta})^2]}}{2 \cdot M_X} \quad (4.16)$$

The transversal momentum is randomised assuming a standard differential cross-section dependence on the transversal momentum:

$$\frac{d\sigma}{d(p_{\perp})^2} \sim e^{-6 \cdot p_{\perp}} \quad (4.17)$$

Therefore the distribution to randomise  $p_{\perp}$  is:  $2 \cdot p_{\perp} \cdot e^{-6 \cdot p_{\perp}}$ . The events are selected so that the  $p_{\perp}$  is never larger than the total momentum. The angle  $\varphi$  is also randomised between 0 and  $2\pi$  to determine the components of the momentum of the products:  $p_{x_{products}}$  and  $p_{y_{products}}$ .

At this point an assumption was made about which particle moves in which direction in the centre of mass system of the object X. The decision was made to focus on the case where  $\eta$  should travel backward and  $\pi^-$  will travel in the forward direction. The reason for this choice was to consider that the pion has obviously the same quantum numbers and carries the same quarks as the incoming pion. Therefore it is reasonable to think

that it will follow the same direction as the incoming pion. The acceptance for the events where eta travels in the reverse direction in the centre of mass system is larger than in the opposite case. This will be shown in section 4.3.

Considering that the  $\eta$  goes backward in the centre of mass system of the object X, the momentum for  $\pi^-$  is:

$$p_{x_{\pi^-}}^{cm} = p_{\perp} \cdot \sin \varphi \quad (4.18)$$

$$p_{y_{\pi^-}}^{cm} = p_{\perp} \cdot \cos \varphi \quad (4.19)$$

$$p_{z_{\pi^-}}^{cm} = \sqrt{(p_{products}^{cm})^2 - p_{\perp}^2} \quad (4.20)$$

The centre of mass momentum for the  $\eta$  is just the same as for the  $\pi^-$ , but opposite in sign.

Making a Lorentz boost, the momenta for the  $\pi^-$  and the  $\eta$  in the laboratory system can be obtained. The general Lorentz boost formula can be written as:

$$E_i = \gamma \cdot E_i^{cm} + \vec{\eta} \cdot \vec{p}_i^{cm} \quad (4.21)$$

$$\vec{p}_i = \vec{p}_i^{cm} + \vec{\eta} \cdot \frac{E_i^{cm} + E_i}{1 + \gamma} \quad (4.22)$$

where  $i$  is the index which indicates  $\pi^-$  or  $\eta$ .  $E_i^{cm}$  is the energy of the particle  $i$  in the centre of mass system and can be expressed as  $E_i^{cm} = \sqrt{p_i^{cm\ 2} + m_i^2}$ . The expressions for  $\gamma$  and  $\eta$  are:  $\gamma = \frac{E_X}{M_X}$  and  $\vec{\eta} = \frac{\vec{p}_X}{M_X}$ , respectively.

So far, the kinematic variables are computed for a beam with only a  $z$  component, which does not correspond to reality. When introducing in the simulation the realistic hadron beam description for COMPASS, the whole event must be rotated with the beam. First a rotation around the  $y$  axis (of an angle  $\theta$ ) and then the rotation around the  $z$  axis (of an angle  $\varphi$ ) is performed.

From the simulation, all the kinematic information of the events can be retrieved. The momenta in the laboratory system of all 3 particles ( $p$ ,  $\eta$  and  $\pi^-$ ) in the final state are shown in figure 4.3.

Another interesting plot which can be produced with the event generator is the angle  $\theta$  of the outgoing  $\pi^-$  compared to the angle of the incoming  $\pi^-$ . This is shown in figure 4.4.

An interface was written between the event generator and the simulation program COMGEANT [48]. COMGEANT will be used to study both the interaction of the simulated particles with the detectors and the response of the detectors. The geometrical acceptance of the events produced with the event generator will also be studied with COMGEANT. What COMGEANT does exactly will be explained when describing the simulation of the COMPASS detector and the study of the geometrical acceptance for diffractive dissociation events in section 4.3.

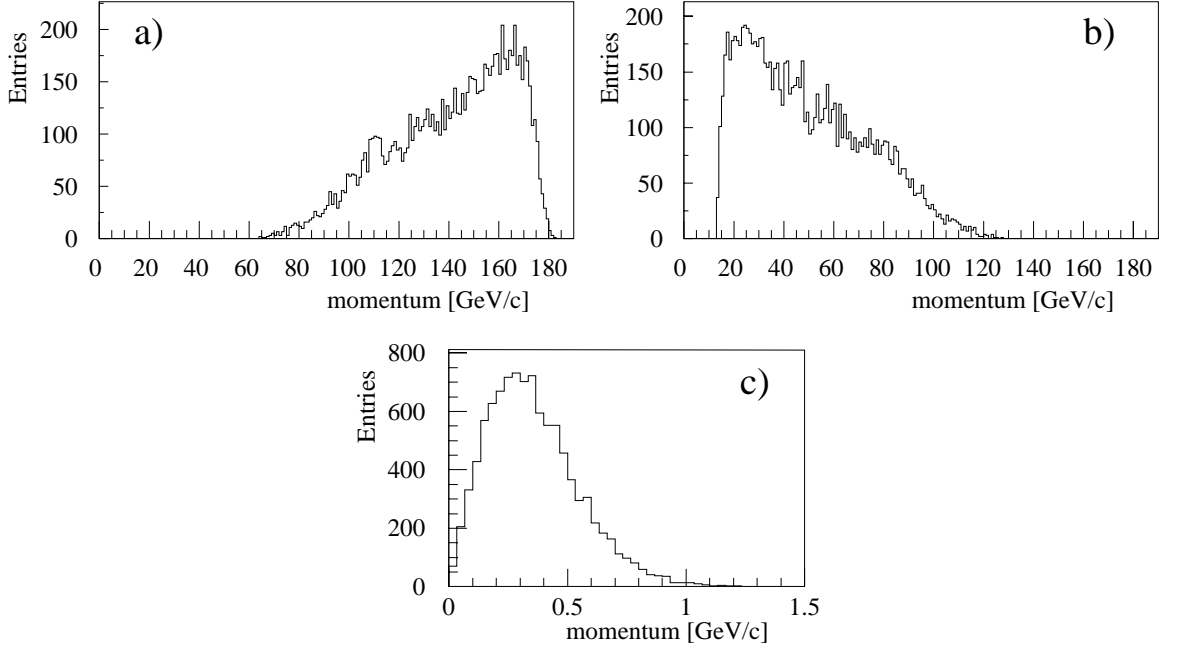


Figure 4.3: Total momentum for a) outgoing  $\pi^-$ , b)  $\eta$  and c) p of diffractive events.

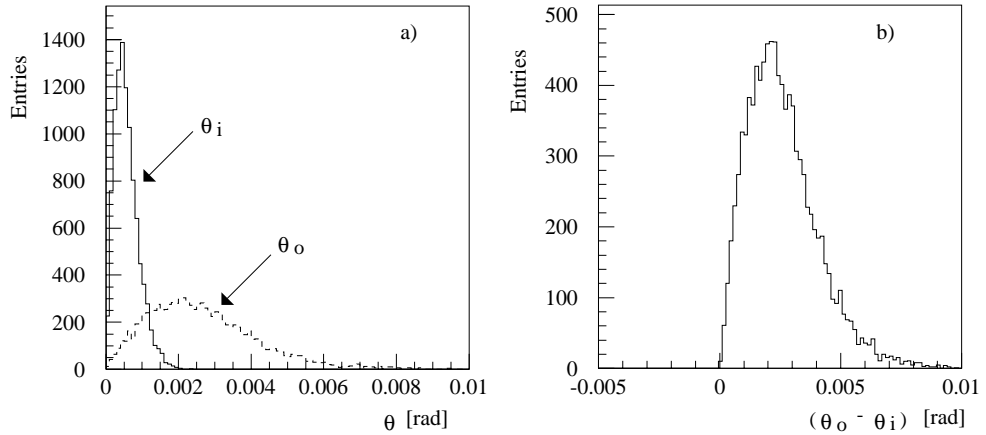


Figure 4.4: Diffractive dissociation: a) polar angles  $\theta_i$  of the incoming  $\pi^-$  and  $\theta_0$  of the outgoing  $\pi^-$ . b) scattering angle  $\theta_0 - \theta_i$  of the outgoing  $\pi^-$ .

## Experimental requirements

The characteristics of the diffractively produced events and the requirements for the COMPASS detector to accept these events are described here.

As shown by the event generator for diffractive dissociation events, the angle of the outgoing  $\pi^-$  is not very large, on the order of 3 mrad. Nevertheless the momenta of the outgoing  $\pi^-$  and the  $\eta$  are quite large, together they carry approximately the momentum of the beam (equal to 190 GeV/c). The momentum transfer to the target proton is very small, less than 1 GeV/c (see figure 4.3).

From the signature of the process, it is clear that the experimental setup should provide tracking detectors for the  $\pi^-$  as well as a photon detector (ECAL2 in the COMPASS detector) for the two gammas from the  $\eta$  decay. For the very slow recoil p a veto box will

be needed around the target. An energy deposition from the proton must be present at large angles in the veto box.

A trigger could be based on the following elements: a veto box, plus two gammas in the ECAL2 acceptance; and one charged particle with an angle corresponding to that of the scattered pion.

In the section concerning the acceptance, the detector that could be used in COMPASS for the hadron programme is described. Nevertheless a more detailed explanation about the trigger and the measurements performed is given in section 4.4.5.

## 4.2 Primakoff reaction

### 4.2.1 General features of the Primakoff reaction

The Primakoff reaction is schematically shown in figure 4.5.

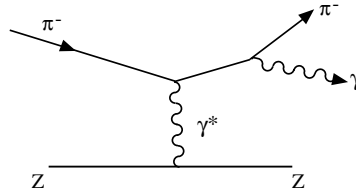


Figure 4.5: Pion radiative scattering in the Coulomb field of a nucleus.

A highly energetic pion scatters in the Coulomb field of a nucleus via a virtual photon emitting a pion and a real photon [49]. Due to the internal structure of the pion, the differential cross-section for this process will differ from the cross-section for Coulomb scattering of a point-like particle. This difference in cross-sections is due to the electromagnetic polarizability of the pion. The electromagnetic polarizability of a particle is given by the electric and magnetic dipole moments induced in the system by an external electromagnetic field [58]. Those quantities are fundamental constants of a particle. Since they determine the particle deformation in external electrical and magnetic fields, they give an idea of its internal structure and dynamics. The first results for the electric and magnetic polarizabilities for the pion ( $\alpha_\pi$  and  $\beta_\pi$  respectively) were obtained at the Serpukhov experiment [59] [60] which found:

$$\beta_\pi = (-7.1 \pm 2.8_{stat} \pm 1.8_{sys}) \cdot 10^{-43} \text{cm}^3 \quad (4.23)$$

$$\alpha_\pi + \beta_\pi = (1.4 \pm 3.1_{stat} \pm 2.5_{sys}) \cdot 10^{-43} \text{cm}^3 \quad (4.24)$$

The estimation of the sum of polarizabilities agrees with the theoretical prediction that  $\alpha_\pi + \beta_\pi \approx 0$ . As it will be shown in chapter 4.4, within the COMPASS experiment the electric and magnetic polarizabilities can be obtained with 10 times more statistics improving the accuracy with respect to the Serpukhov experiment.

### 4.2.2 The Primakoff cross-section

The triple differential cross-section for the Primakoff reaction is given by [57]:

$$\frac{d^3\sigma}{dt ds_1 d\cos\theta} = \frac{\alpha}{\pi} \cdot \frac{Z^2}{s_1 - m_h^2} \cdot \frac{t - t_{min}}{t^2} \cdot |F_A(t)|^2 \cdot \frac{d\sigma_{\gamma h}}{d\cos\theta} \quad (4.25)$$

where  $\alpha$  is the fine structure constant and  $Z$  is the electric charge of the nuclear target.  $t$  is the four momentum transfer squared to the target nucleus and  $s_1$  is the  $\gamma \pi^-$  invariant mass squared in the final state.  $F_A(t)$  is the electromagnetic form factor of the nucleus and  $d\sigma_{\gamma h}/d\cos\theta$  is the differential cross-section for Compton scattering on the projectile hadron. The minimum four-momentum transfer  $t_{min}$  depends on the virtual photon energy  $\omega$  like:

$$-t_{min} = \left( \frac{m_h \cdot \omega}{p_h} \right)^2 \quad (4.26)$$

$p_h$  being the incident hadron momentum in the laboratory and  $m_h$  being the mass of the incident hadron.

In the case where the hadron is a pion, the differential cross-section is given by:

$$\frac{d\sigma_{\gamma\pi}}{d\cos\theta} = \frac{\pi\alpha^2}{m_\pi^2} \cdot \frac{|T|^2}{\left[1 + \frac{\omega}{m_\pi} \cdot (1 - \cos\theta)\right]^2} \quad (4.27)$$

with

$$|T|^2 = (1 + \cos^2\theta) \cdot \left[1 - \frac{2(\alpha_\pi + \beta_\pi)m_\pi}{\alpha} \omega\omega'\right] + \frac{2\beta_\pi m_\pi}{\alpha} (1 - \cos\theta)^2 \omega\omega' \quad (4.28)$$

The real photon energy in the projectile frame  $\omega'$  depends on  $\omega$  according to the Compton relation:

$$\omega' = \frac{\omega}{1 + \frac{\omega}{m_\pi}(1 - \cos\theta)} \quad (4.29)$$

### 4.2.3 Study of $\pi^- Z \rightarrow \pi^- Z \gamma$ in COMPASS

The electromagnetic polarizability of  $\pi^-$ ,  $K^-$  and  $p$  can be studied in COMPASS due to the possibility of using them as beam particles. The values obtained to date for the electromagnetic polarizability of the pion were shown in equations (4.23) and (4.24). For the proton, the values are shown in the following equations:

$$\beta_p = (0.7 \pm 1.6_{stat}) \cdot 10^{-43} \text{cm}^3 \quad (4.30)$$

$$\alpha_p = (10.7 \pm 1.1_{stat}) \cdot 10^{-43} \text{cm}^3 \quad (4.31)$$

For the kaon, only a few experimental limitations have been obtained to date [60]:

$$\alpha_K < 200 \cdot 10^{-43} \text{cm}^3 \quad (4.32)$$

By using  $\mu^-$  as the beam particle, it will be possible to compare the reactions  $\pi^- Z \rightarrow \pi^- Z \gamma$  with those of a point-like particle:  $\mu^- Z \rightarrow \mu^- Z \gamma$ . A 3 mm lead target (1.8 % absorption length, 54 % of interaction length) will be used to provide a high  $Z$  nuclear target. In a second stage, different target materials could be used to check the dependence of the absolute cross-section on  $Z^2$ .

### Event generator

The event generator which was used to study the principal features of the Primakoff reactions was named Polaris [71]. The structure of the event generator is described in detail in reference [57]. This program has also an interface called poltogeant, which will be used to pass the events to COMGEANT. From the program one can retrieve the kinematical information of the events.

The four momentum transfer squared in the Primakoff reaction is defined as:

$$t = [\mathbf{p}_{incoming \pi^-} - (\mathbf{p}_{outgoing \pi^-} + \mathbf{p}_\gamma)]^2 \quad (4.33)$$

where  $\mathbf{p}_{incoming \pi^-}$ ,  $\mathbf{p}_{outgoing \pi^-}$  and  $\mathbf{p}_\gamma$  are the four momenta of the incoming  $\pi^-$ , the outgoing  $\pi^-$  and the gamma respectively. The four momentum transfer squared is shown in figure 4.6. It has a very sharp peak, called Coulomb peak, which is very characteristic for Primakoff processes.

Another interesting kinematic variable is the momentum in the laboratory system of the two particles ( $\pi^-$  and  $\gamma$ ) in the final state, shown in figure 4.6.b and 4.6.c. The sum of these momenta should always in good approximation be equal to the momentum of the beam.

The typical opening angle between the outgoing  $\pi^-$  and  $\gamma$  can be calculated as:  $\theta \sim \frac{m_{\pi^-}}{E_{beam}}$ . For a 180 GeV/c beam, the opening angle is about 0.8 mrad. For a beam of 190 GeV/c, the opening angle will be about 0.73 mrad. This value is the one shown in figure 4.7.

### Experimental requirements

A characteristic feature of the Primakoff reactions is that a very small momentum is transferred to the nuclear target as shown in figure 4.6.a. One of the requirements is that this momentum transfer to the nuclear target should be measured with high accuracy. This means that a good momentum reconstruction of the  $\pi^-$  and  $\gamma$  is needed. For high energies, the  $\pi^-$  and  $\gamma$  will be very forward boosted, with typical opening angles of  $\theta \sim \frac{m_{\pi^-}}{E_{beam}}$ . Tracking detectors will cover the very forward region and the ECAL2 photon detector will be situated at  $\sim 30$  m from the target and will cover  $2.4 \times 1.2 \text{m}^2$ .

The trigger can be similar to the one that will be used in the diffractive dissociation measurements. This will be explained in more detail in section 4.4.5.

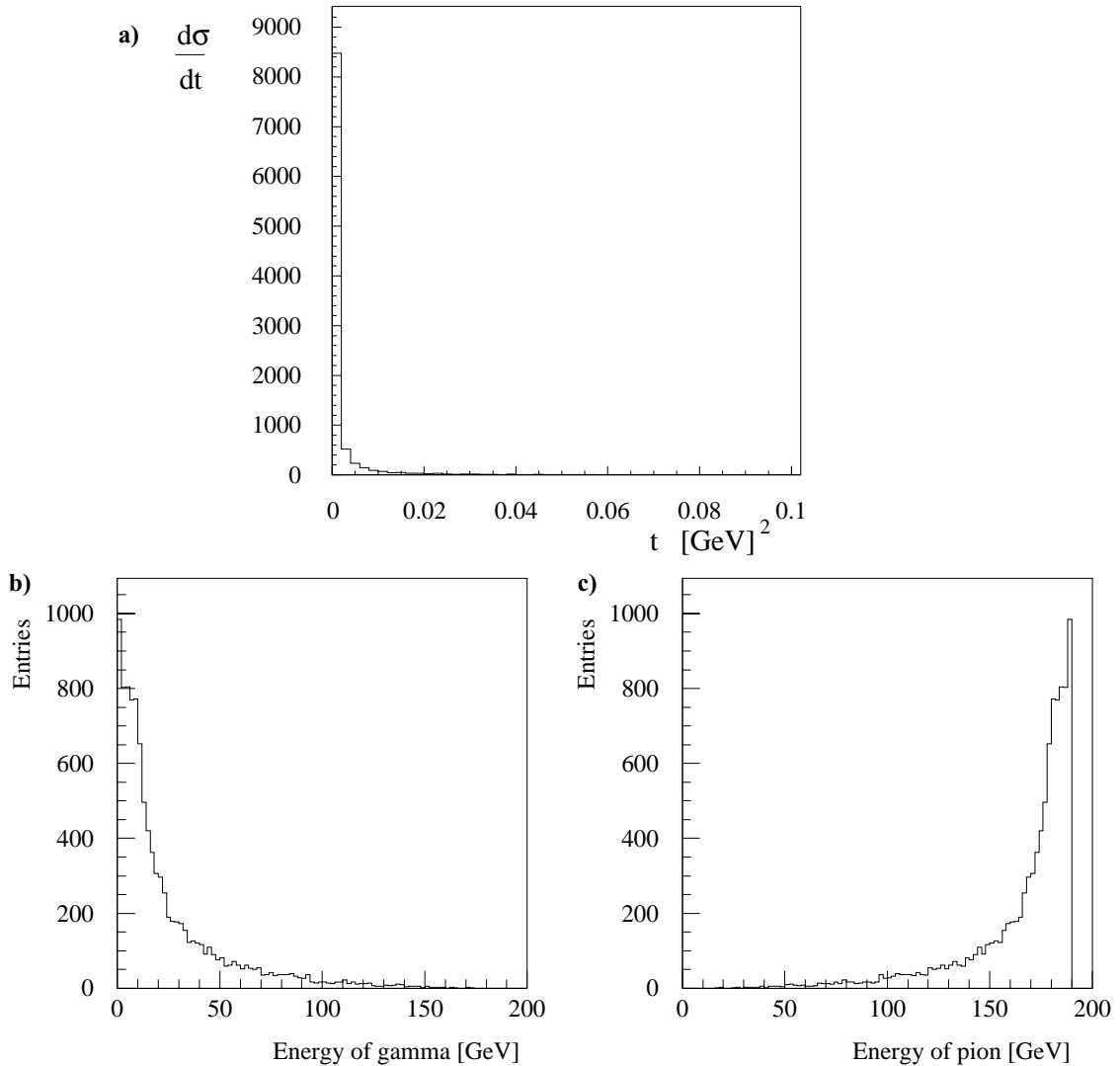


Figure 4.6: Primakoff reaction a) dependence of the cross-section on the four momentum transfer squared  $t$ , b) Energy of the gamma in the final state and c) Momentum of the pion in the final state.

## 4.3 Acceptance studies

### 4.3.1 COMPASS detector for the initial hadron programme

To prove that the COMPASS detector is suited for the Primakoff reaction and diffractive dissociation, a Monte Carlo based simulation was done using COMGEANT. COMGEANT is the interface to the GEANT3.21 [50] software, including the geometrical properties of the COMPASS detector. The GEANT program simulates interactions and decays of particles and resonances in the detector.

The detector for the initial hadron programme in COMPASS should be similar to the detector that will be used for the muon programme in order to reduce the "dead time" when switching between physics programmes. Nevertheless, the detector should be suited for the characteristics of the physics programmes of interest.

In table 4.1, the COMPASS detector is described by defining the positions of all its

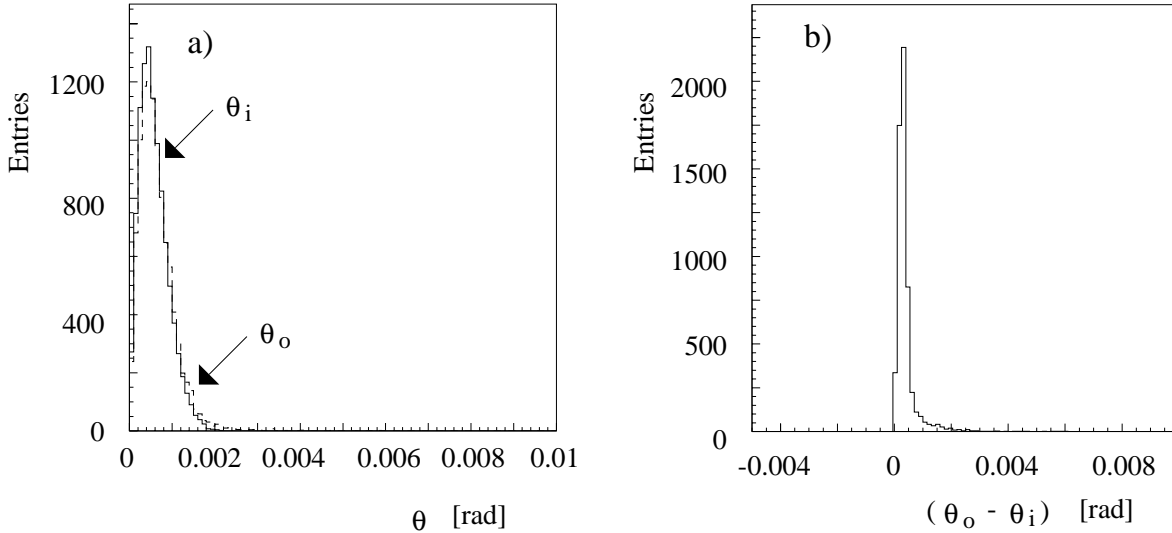


Figure 4.7: Primakoff reaction: a) polar angles  $\theta_i$  of the incoming  $\pi^-$  and  $\theta_o$  of the outgoing  $\pi^-$ . b) scattering angle  $\theta_o - \theta_i$  of the outgoing  $\pi^-$ .

different components. The setup described is the official setup for operations in 2001. The official setup is the result of an agreement of the different detector groups in the COMPASS technical board meeting on the 25th of January 2001.

Some explanation of the different positions for the detectors is given here. The scintillating fibres hodoscopes 1 and 2, placed upstream of the target, should monitor the beam. The purpose of the veto, upstream of the target, is to ensure that the beam spot is not larger than the target itself. Further upstream of the target, two more detectors are present, consisting of two silicon microstrip stations (stations 1 and 2). Each station will have 4 projections: 0, 90, +10 and -10 deg. These two stations have a lever arm of 50 cm, which is necessary to measure the angle of the incoming pion. Two more stations of silicon detectors (stations 3 and 4) will be placed downstream of the target also with 50 cm lever arm. They will measure the angle of the outgoing pion. The angle difference between the incoming and outgoing pion is a very characteristic variable for the Primakoff reaction. The silicon detectors, with a typical spatial resolution of 14  $\mu\text{m}$ , will determine the characteristic angle for the Primakoff reaction with high accuracy, as will be shown later. The silicon stations 3 and 4 will also provide some tracking between the target and the first spectrometer magnet (SM1). The veto box will be situated around the target. It has a hole for the incoming beam and a hole for the outgoing very forward particles. For Primakoff reactions, the recoil momentum of the target is very small, less than 0.02  $\text{GeV}/c^2$  (see 4.6.a). In this case, no track at all should be recorded in the veto box. The events with this signature could come from Primakoff reaction thus they will be analyzed. For diffractive processes, the recoil momentum of the target is also small, less than 1  $\text{GeV}/c^2$  (see 4.2). In this case, the recoil proton should hit the veto at a large angle. Events with one hit in the veto at large angle could be a signature for diffractive events.

For tracking, several track segments are required. The first lies between the target and the first magnet, another track segment is located between both magnets, and a last track segment lies between the second magnet and the electromagnetic calorimeter. For this purpose, different tracking detectors are distributed along the beam line. To cover all of the acceptance, tracking detectors of different sizes are used. The main tracking detectors

<i>Detector name</i>	<i>Location along beam axis [cm]</i>	<i>Lateral displacement [cm]</i>
Scintillating fibre station 1	-800	–
Scintillating fibre station 2	-290	–
Veto 1	-100	–
Silicon microstrip detector 1	-80	–
Silicon microstrip detector 2	-30	–
Veto box	-10 to 10	–
Target	0	–
Silicon microstrip detector 3	30	–
Silicon microstrip detector 4	80	–
Scintillating fibre station 3	164	–
Scintillating fibre station 4	215.5	–
Saclay $\mu\omega$	234.5	–
Saclay DC	250.5	–
SM1	262 to 438	–
Silicon microstrip detector 5	450	–
1st straw submodule	519	–
2nd straw submodule	531	–
Scintillating fibre station 5	555	–
RICH1	560-900	–
GEM 1	913	1
MWPCA*	925	1
ECAL 1	937-1115	–
HCAL 1	1115-1280	–
GEM 2	1301	1.5
Scintillating fibre station 6	1308	1.5
MWPCA 1	1320	1.5
GEM 3	1486	2
MWPCA 2	1500	2
SM2	1530 to 1930	–
MWPCA 3	1980	4.5
Scintillating fibre station 7	2000	4.7
MWPCA 4	2020	5
MWPCA 5	2040	5
GEM 4	2064	5
Scintillating fibre station 8	3150	16
GEM 5	3166	16
MWPCA 6	3180	16.5
ECAL 2	3226 to 3476	16.5

Table 4.1: Location of the components of the COMPASS detector for the initial hadron programme.

for the initial hadron programme are the GEMs, the silicon and the MWPCs. The Saclay  $\mu\Omega$ s, the Saclay DCs and the straw detectors are not very important for tracking in

the hadron programme discussed. In the region where these detectors are situated, the angles of the particles considered are very small. The majority of these particles will pass through the holes or the insensitive regions of these detectors. Due to the present design of the tracking algorithm, at least three orientations are required to consider a detector as tracking detector. The scintillating fibres, only having two orientations (0 and 90 degrees) are not considered as trackers for the moment. The GEM detectors have an insensitive area 50 mm in diameter at the centre. The only detectors that could cover this hole for tracking would have been the scintillating fibres. Since these detectors are not used for tracking, the COMPASS detector has holes for certain particle momenta at certain angles. The gamma detector in COMPASS, the ECAL2, has also a hole for the deflected beam. This hole will cause a loss in acceptance for Primakoff and diffractive events, as it will be shown later in section 4.3.2.

The actual hadron setup finishes after ECAL2 even though other detectors are existing behind ECAL2. These detectors will be used in the muon programme. A detector still missing in the described setup is the scintillator hodoscope that will be used for trigger purposes. This will be situated at the end of the hadron setup, in front of the electromagnetic calorimeter (ECAL2). The acceptance for Primakoff and diffractive processes using these detectors will be shown in the next sections.

## Material budget

Crucial for the physics programmes is the amount of material introduced by the different detectors. Survival probabilities of particles can be studied directly from the COMGEANT Monte Carlo simulations.

A general event generator was developed to generate gammas with random angle  $\varphi$  and different transversal momenta  $p_{\perp}$  following a flat distribution. Studies of the survival probability of these particles in the COMPASS detector were carried out using this general event generator. A gamma detector placed at 30 m from the target, the ECAL2, is responsible for the detection of the gammas from diffractive and Primakoff processes.

Figure 4.8 shows the survival probability for a gamma (integrated over the entire range of longitudinal and transverse momenta). The number of gammas along the detector will be reduced due to the gamma conversions in the different detectors.

The major gamma loss comes from the conversions in the RICH1 detector. The RICH1 detector contains 3.4 m of  $C_4F_{10}$  gas along the beam line, which corresponds to 10.5 % of radiation length. To avoid gamma conversions in this region, a beam pipe has to be installed in the RICH1 detector. This pipe should contain a light gas such as He to reduce the amount of material.

### 4.3.2 Geometrical acceptance

The geometry of the detector proposed for the initial hadron programme had to be optimized. The reconstruction program was not suited for this purpose. Certain unknown quantities, like the reconstruction efficiency, prohibit a clear understanding of the geometrical acceptance of the setup. Two event generators were developed to produce gammas and pions with the corresponding characteristics of those produced in Primakoff or diffractive reactions. Passing these particles into COMGEANT and analysing the output, some conclusions can be drawn concerning the geometrical acceptance of the setup.

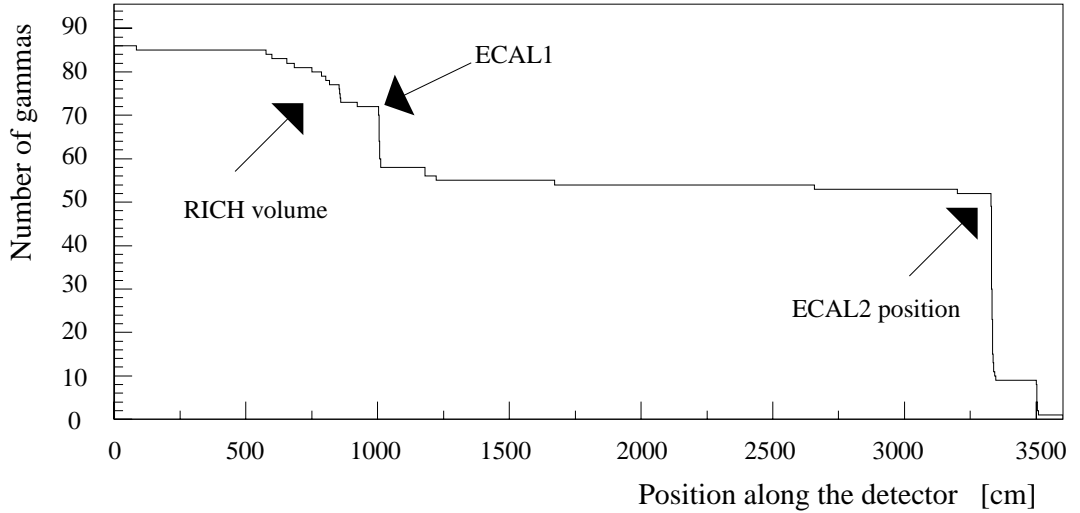


Figure 4.8: Number of gammas at different positions along the detector. In the region of the RICH as well as in the position of the ECAL1, a large amount of gammas is converted. ECAL1 has a large hole, thus only gammas with large angles will be converted there. At the ECAL2 position almost all remaining gammas are converted except for those that escape through the hole of the ECAL2 and those with angles larger than the acceptance of the ECAL2.

### Acceptance for the pions

First, the geometrical acceptance for pions with the characteristics of Primakoff and diffractive pions was studied. For this purpose, an event generator was developed where pions were generated with two particular transversal momenta with values 0.1 GeV/c and 1 GeV/c. These values are close to be the typical values for Primakoff and diffractive reactions. Five different longitudinal momenta were generated, 30 GeV/c, 60 GeV/c, 90 GeV/c, 120 GeV/c and 150 GeV/c to cover most of the momentum range. The angle  $\varphi$  was randomized between 0 and  $2\pi$ . Only two physical processes were permitted in the Monte Carlo simulations: the energy loss by the Bethe-Bloch process and multiple scattering.

The results were analysed as follows: the spatial distributions for the pions were plotted at different positions along the COMPASS detector. To check if the detector situated at a specific place would detect the pions, the geometrical shape of the detectors was drawn on the same plot. The event generator used was just described. The plots were produced for what was called "Primakoff pions" and "diffractive pions". "Primakoff pions" are pions with the kinematics of Primakoff events (transversal momentum of 0.1 GeV/c and longitudinal momenta between 30 GeV/c and 150 GeV/c). "Diffractive pions" are pions with the kinematics of diffractive events (transversal momentum of 1 GeV/c and longitudinal momenta between 30 GeV/c and 150 GeV/c). Figure 4.9.a shows the spatial distributions for Primakoff pions at 46 cm from the target. The different rings correspond to the different longitudinal momenta generated (as explained in the event generator). Figure 4.9.b shows the spatial distributions for diffractive pions at 46 cm from the target. The different rings correspond to the different longitudinal momenta generated (as explained in the event generator). The detector placed there to cover the acceptance is one of the silicon stations. It is situated 30 cm from the target.

As can be observed from figure 4.9, the silicon station 3 covers the total acceptance

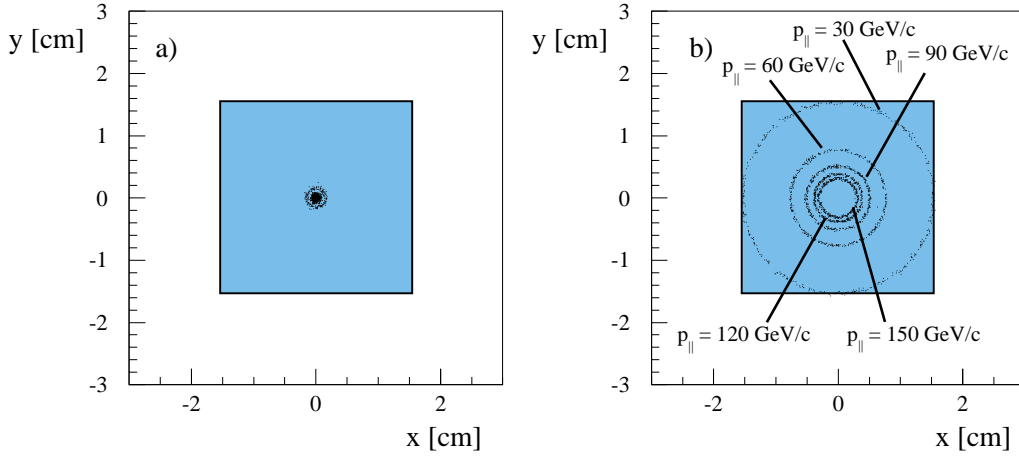


Figure 4.9: Hit distributions at 46 cm from the target for a) Primakoff pions and b) diffractively produced pions. In b) the different longitudinal momenta are indicated. The coloured box refers to the size of the silicon detector.

of the Primakoff and diffractive pions. The different rings correspond to the different longitudinal momentum of the pions. All pions before SM1 will hit the silicon tracker.

The same process can be done for a position 1507 cm from the target (figure 4.10), situated after SM1 and just in front of SM2.

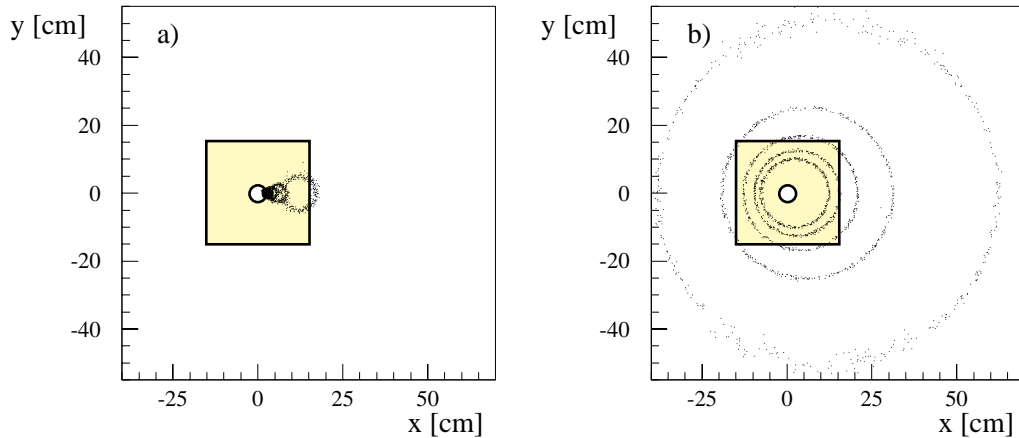


Figure 4.10: Spatial distributions at 1507 cm from the target for a) Primakoff pions and b) diffractively produced pions. The coloured box corresponds to the GEM detector. The insensitive region of the detector is also indicated at the centre. The boundaries of the MWPC are larger than the plot, thus they are not shown.

There are the 3 kinds of detectors close to this position to cover the acceptance. The detectors at this position are the MWPCs, the GEMs covering the insensitive area of the MWPCs and the scintillating fibres covering the insensitive area of the GEMs. In the present tracking algorithm, the scintillating fibres are not considered as tracking detectors. The highly energetic pions from Primakoff are therefore lost since they are inside the insensitive area of the GEMs.

At the position 1987 cm from the target, after SM2, the very low energetic pions produced in the diffractive process do not hit any detector. The momentum of these pions can nevertheless be measured using the SM1 spectrometer. The most energetic pions

produced in Primakoff reactions will pass, also in this case, through the insensitive region of the GEMs as can be seen in figure 4.11.

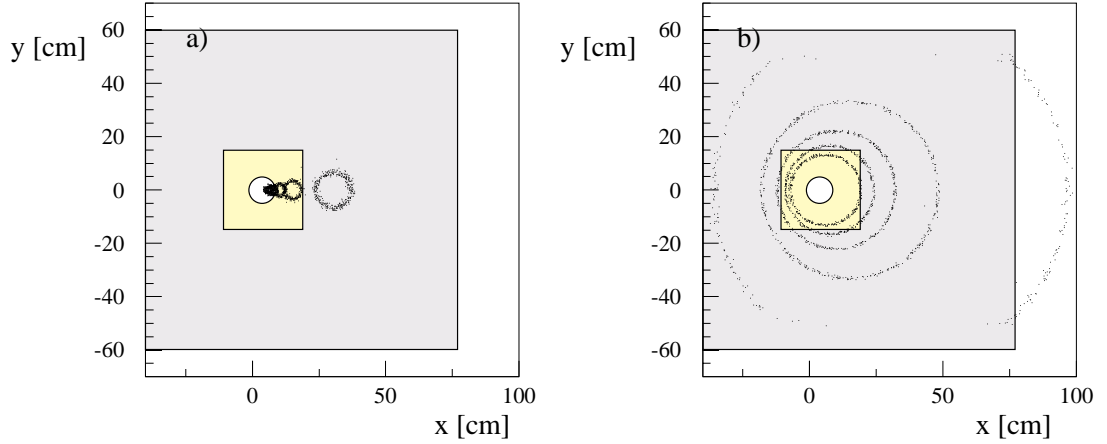


Figure 4.11: Spatial distributions at 1987 cm from the target for a) Primakoff pions and b) diffractively produced pions. The large coloured box corresponds to the MWPCA detector and the small coloured box corresponds to the GEM detector. The insensitive region of the GEM detector is also indicated in its centre, but the insensitive region of the MWPCA is not indicated since that area is covered by the GEM.

In figure 4.11.b, a cut off can be observed for the low energy diffractive pions. The reason for this is the vertical acceptance of SM2. The acceptance of the magnet in the  $y$  direction is about 1 m (from -50 cm to 50 cm). Particles with low momentum strike the wall of the magnet. This effect can also be observed in figure 4.12.b. There the acceptance window of SM2 in the horizontal direction is also visible.

The acceptance before the ECAL2 is plotted in figure 4.12. The low energetic pions belonging to Primakoff reactions are not covered by any tracking detector at this point. Thus the tracking for these pions should be done before reaching ECAL2. This could be achieved with several MWPCs with the necessary lever arm situated after SM2.

### Acceptance for the gammas

The geometrical acceptance for the gammas of Primakoff and diffractive events was studied. As for the case of the pions, this was achieved using an event generator producing gammas with a particular transversal momenta of 0.1 GeV/c. The value corresponds approximately to gammas produced in Primakoff events. In the case of diffraction,  $\eta$  mesons were generated with a fixed transversal momentum of 1 GeV/c. In COMGEANT, the  $\eta$ 's decayed and the decay channel of  $\eta$  into two gammas was selected. The gammas for Primakoff reactions as well as the  $\eta$ 's for diffraction were generated with different longitudinal momenta ranging from 30 GeV/c to 150 GeV/c. The angle  $\varphi$  was randomized between 0 and  $2\pi$ .

The most critical case corresponds to the acceptance of the gammas from the  $\eta$  decay. In this case two gammas have to be detected. 10000  $\eta$ 's with the characteristics mentioned before were generated. Out of these 10000  $\eta$ 's only 3832 decayed in the channel of interest,  $\eta \rightarrow \gamma \gamma$ . In total, 7664 gammas were passed through the detector using the COMGEANT simulation package. Not all of the gammas reached the ECAL2. Some of the gammas were converted before reaching ECAL2 and others passed through the hole of the calorimeter.

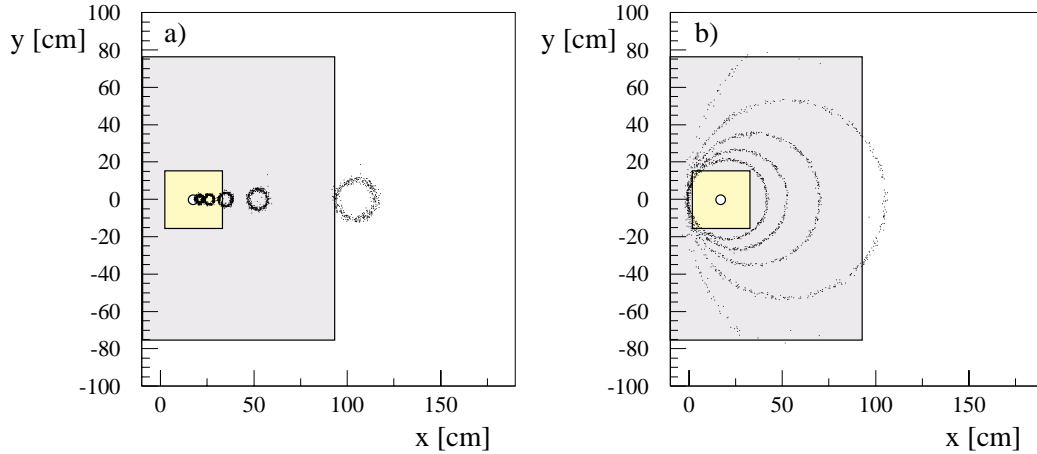


Figure 4.12: Spatial distributions at 3200 cm from the target for a) Primakoff pions and b) diffractively produced pions. The big coloured box corresponds to the MWPCA detector and the small coloured box corresponds to the GEM detector. The insensitive region of the GEM detector is also indicated in its centre, but the insensitive region of the MWPCA is not indicated since that area is covered by the GEM.

In this simulation, the event was considered lost when at least one of the gammas from the eta decay were converted before reaching the ECAL2 or passing through the hole of the ECAL2. The hole of the calorimeter is  $7.66 \text{ cm} \times 7.66 \text{ cm}$  in size. It was found that the number of events where the two gammas arrived and were converted in the ECAL2 was 1032 (2064 gammas). This means that, in principle, with 100% detection efficiency, 27% of the  $\eta$ 's can be reconstructed. Figure 4.13.a shows the spatial distribution in the x-y plane of the gammas generated from the  $\eta$  decay extrapolated to the ECAL2 surface. Figure 4.13.b shows the real hits of the gammas in the ECAL2 surface.

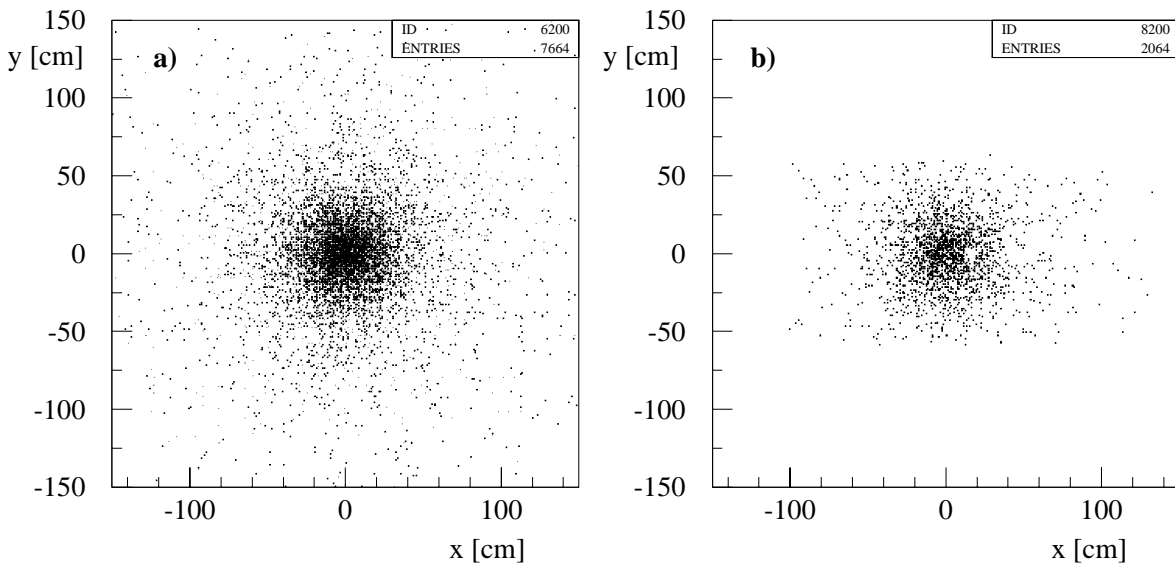


Figure 4.13: a) Spatial distribution of the gammas generated from the  $\eta$  decay extrapolated to the position of ECAL2 and b) Hits generated by the conversion of  $\eta$  decay.

### Combined acceptance

The combined geometrical acceptance for Primakoff and diffractive dissociation events was studied and the results are summarised in this section. No reconstruction was performed at this stage, only the purely geometrical acceptance is shown.

For the geometrical acceptance of the diffractive events, the event generator described in section 4.1.2 was employed. For the simulation of the detector response, COMGEANT was used. Only the physical processes multiple scattering, energy loss and pair production were permitted. The event generator provides COMGEANT with the particles involved in the event, their momentum and their vertices of production. COMGEANT simulates the detector response as well as the interactions of these particles with the material in the detectors. In the case of diffraction, four particles are passed from the event generator to COMGEANT, including the incoming beam pion, the outgoing pion (after the interaction), the proton and the  $\eta$ . The decay of the  $\eta$  is simulated in COMGEANT. The signature of an interesting event is a very slow proton, a fast pion with small scattering angle, and two gammas produced in the  $\eta$  decay. 40% of the total events generated correspond to the events where the  $\eta$  decays into two gammas.

Out of 10000 generated diffractive events containing an  $\eta$ , which decay with a branching ratio of 38% to  $\gamma\gamma$ , the number of events where both gammas convert in the ECAL2 corresponds to 876 events (1572 gammas). Figure 4.14 shows where in the COMPASS detector the gammas converted most often, between 500-900 cm in the RICH, at 1000 cm in the ECAL1 and at 3400 cm in the ECAL2, where they should convert.

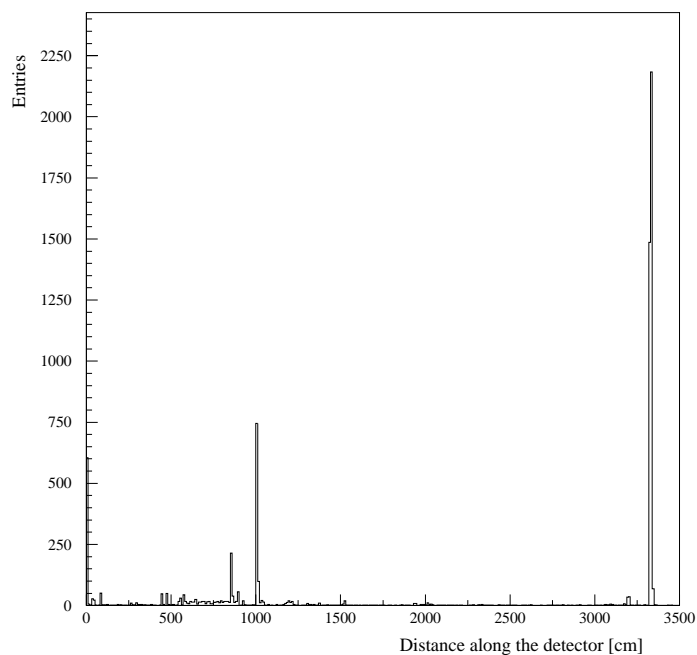


Figure 4.14: Position of the conversion of the gammas created in the  $\eta$  decay generated with the diffractive event generator.

In twenty-two percent of the events, the two gammas of the  $\eta$  convert in ECAL2. This result differs from the result obtained when calculating the acceptance only for the gammas. The reason is that the programs used in both cases generate slightly different kinematics. The general purpose event generator was developed to generate  $\eta$ 's with char-

acteristics close to the etas of a diffractive event. The  $\eta$ 's in this study were generated using an event generator specially developed for diffractive dissociation (see section 4.1.2). From the total number of events generated, only 8% of the events have the two gammas converted in ECAL2. For these events, the acceptance for the pion was also studied.

The following three different zones are considered in the COMPASS detector: between the target and the first spectrometer magnet SM1, between SM1 and the second spectrometer magnet SM2, and between SM2 and ECAL2. A first requirement to accept the pion is that it hits the two silicon detectors situated at 30 cm and 80 cm from the target, in front of SM1. From the hits in these detectors, the characteristic opening angle of the reaction can be found. The angle of the beam will be measured in the two silicon stations placed in front of the target for this purpose. At least one hit from the pion is required in any of the detectors situated in the other two zones. Figures 4.15 and 4.16 shows the hits of the pions in some of the detectors situated in the different zones along the COMPASS detector.

In figure 4.15, the dead areas of the detectors are revealed. These dead areas are covered by other smaller detectors. In this configuration, no hole is left for the geometrical acceptance of the COMPASS detector in any of the different zones. This is also shown for the detectors between SM2 and ECAL2 in figure 4.16.

Only a few events are lost after SM1. This indicates that most of the pions are quite energetic and their deflection in the SM1 field is not very large. It was found that the number of pions accepted is 97%. This does not imply that all of these pions can be reconstructed. The requirements to be accepted are not very strong compared to those of being reconstructed. For the reconstruction, at least a track segment is needed before and after one of the spectrometers. Here, a track segment is defined by at least two space points.

A diffractive event was accepted when the two gammas from the eta decay convert in the ECAL2 and the pion was detected in at least two of the three different zones along the detector. Results show that the limiting factor for the acceptance was the number of gammas converted in ECAL2. Only 22% of the selected diffractive events were accepted.

The simulation for the diffractive dissociation was performed for the case where, in the decay of the combined system of  $\eta$  and pion, the  $\eta$  moves backward in the  $\pi\eta$  centre of mass system and the pion forward. The same exercise was repeated for the case where the  $\eta$  moves forward and the pion backward. The acceptance obtained in this case was considerably smaller. An  $\eta$  moving forward in the  $\pi\eta$  centre of mass system is a very fast  $\eta$  in the laboratory system. In its decay, the production angle of the two gammas will be small enough that at least one of them will be lost through the hole of the ECAL2.

The geometrical acceptance for Primakoff events was also simulated. The event generator used for the simulations is the one described in section 4.2.3. Only the physical processes of multiple scattering, energy loss and pair production were permitted. The interaction of the generated particles with the material was simulated in COMGEANT. In the Primakoff events, only the following three particles are generated: the beam pion, the outgoing pion and the gamma. For accepting an event, two conditions must be satisfied. One refers at the acceptance of the pion. The pion should hit the two silicon stations before the SM1 and at least one of the detectors in the two other zones. With both silicon stations, the angle of the reaction can be determined, considering the measured angle of the incoming pion in the two silicon stations situated in front of the target. The second condition is the conversion of the gamma in ECAL2. Results showed that 65% of the

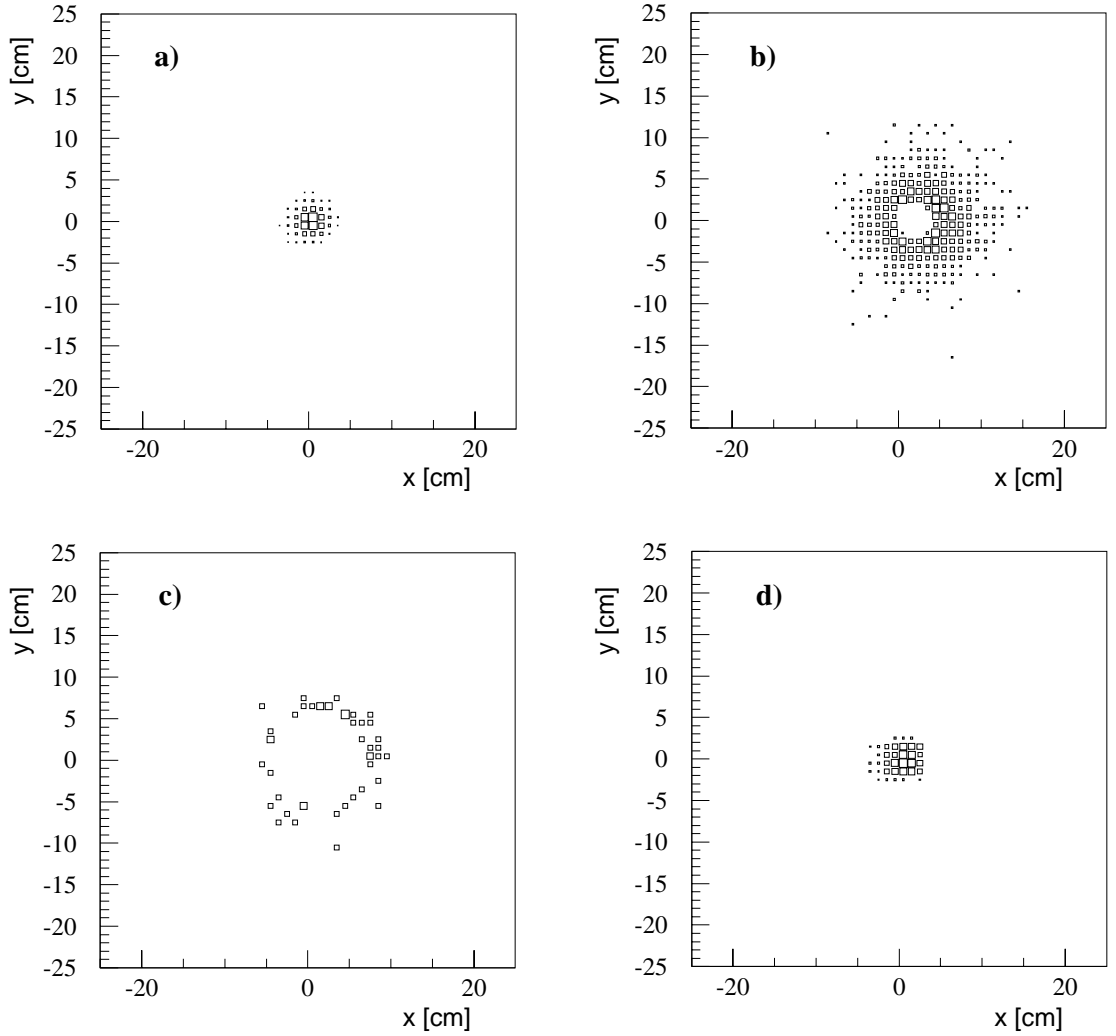


Figure 4.15: Hit positions of the pion at different places in the detector between SM1 and SM2. These pions belong to the events where the  $\eta$  decays into two gammas. a) Pions at the silicon station 4, 4.5 m away from the target b) Pions at 15.21 m from the target, (old position of the GEM station 3) c) Pions at 9.25 m from the target, at a MWPCA detector and d) Pions at 13.08 m at the scintillating fibre station 6.

events generated were accepted.

From the analysis of the Primakoff events, it could be retrieved that a large number of pions pass through the insensitive area of most of the detectors due to their high momenta. Before SM2, only the silicon stations will cover the small area tracking since the scintillating fibres will not be used as tracking detectors. After the SM2 magnet, the situation improves and most of the pions will be detected at the GEMs. The COMPASS detector presents a hole for high-energetic particles, those close to the beam energy.

## 4.4 Possible measurement of $\pi^-$ polarizability

This section describes in detail the full Monte Carlo simulations that were performed to study the possibility of measuring the  $\pi^-$  electromagnetic polarizability by Primakoff

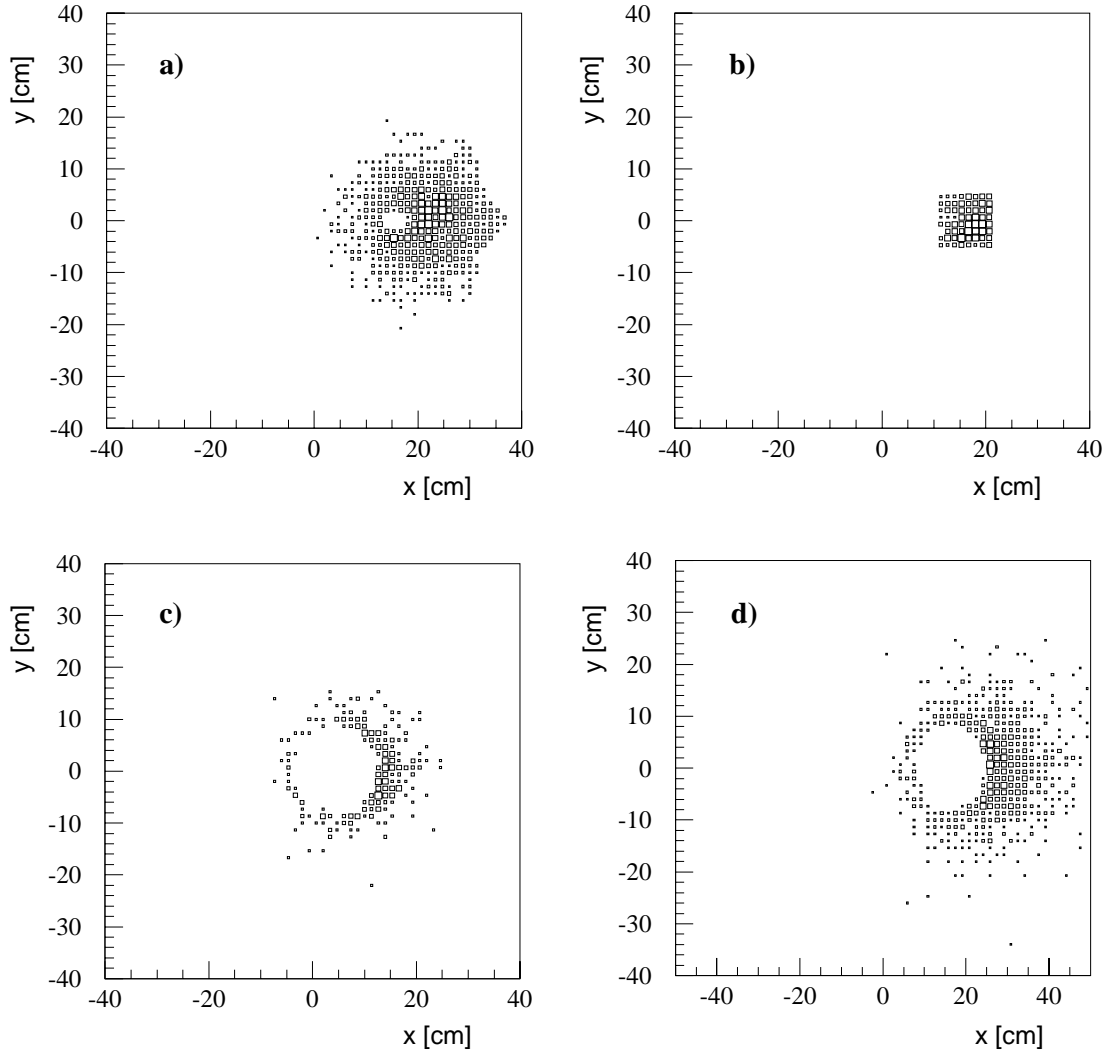


Figure 4.16: Pion hits positions at different places in the detector after SM2. These pions belong to the events where the eta decays into two gammas. a) Pion hits at the GEM 5, 31.7 m away from the target b) Pion hits at 31.5 m from the target, at the scintillating fibre station 8, c) Pion hits at 20.20 m from the target in MWPCA 5 d) Pion hits in MWPCA6 at 31.8 m.

reaction (see figure 4.5) in COMPASS.

#### 4.4.1 Steps previous to the simulation

For debugging purposes, several event generators were developed. The interaction of the events with the detectors was simulated using COMGEANT. As input, the reconstruction program CORAL (**C**OMPASS **R**econstruction and **A**nalysis program) used the output of COMGEANT. The reconstruction program was developed to simulate a realistic response of the detectors where efficiencies and resolutions are included and to define the different trajectories of all charged particles. The COMPASS detector set up used in the simulations was the one which is described in chapter 4.3.

The first event generator generated pions distributed with random momenta between 0 and 200 GeV/c (the momentum of the beam), random azimuthal angles  $\varphi$  between 0 and  $2\pi$ , and polar angles  $\theta$  between 0 and 5 mrad. The kinematic range chosen corre-

sponds to the kinematic range of the Primakoff reaction. This event generator allowed the debugging of several problems found in the chain of the reconstruction program. The main error concerned the description of the detectors, where the existence of the magnetic field was neglected in some regions. Systematic shifts were found when reconstructing the momentum since the magnetic maps in the reconstruction program were defined considering the magnetic field. After the correction of this bug, the error in the reconstructed momentum was estimated to be smaller than 1%, as shown in figure 4.17.

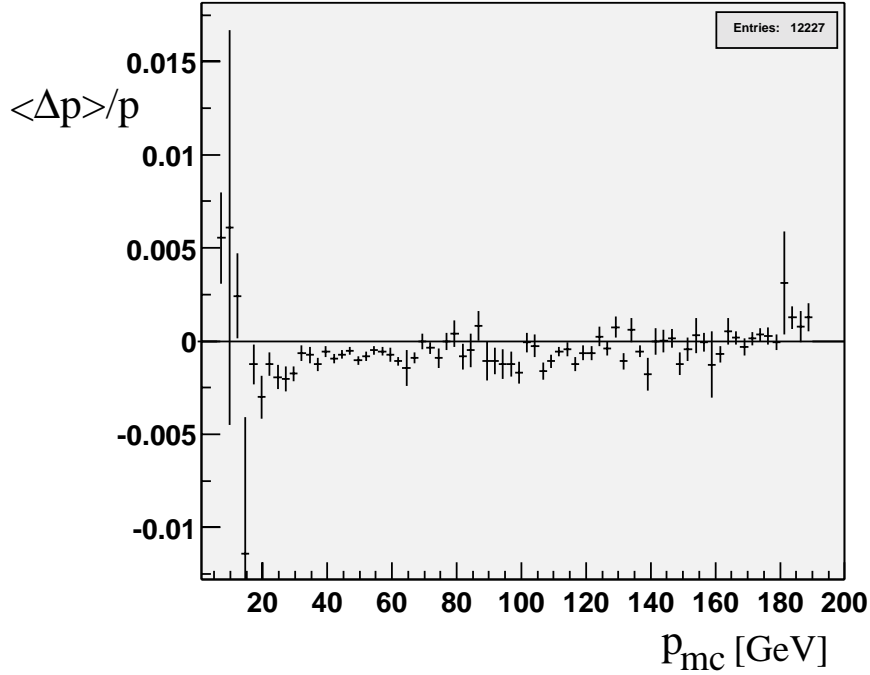


Figure 4.17: Reconstruction error for the momentum of a pion [70].

The reconstruction efficiency for this sample is shown in figure 4.18. As can be observed in the figure, the COMPASS detector has a hole in acceptance visible for small  $\theta$  angles and large longitudinal momenta and for large  $\theta$  angles and small longitudinal momenta. The existence of this hole was already predicted from the results of the acceptance studies.

A second event generator was developed to debug the reconstruction code for the gammas. The gammas were generated with momenta between 0 and 200 GeV/c, random  $\varphi$  angles between 0 and  $2\pi$ , and  $\theta$  angles between 0 and 40 mrad. The range of the  $\theta$  angle was determined to cover the acceptance of the electromagnetic calorimeter situated 32 m from the target (ECAL2) that is responsible to detect the gammas from the Primakoff reaction. The energy resolution for ECAL2, calculated as  $\sigma/E_{rec}$  where  $\sigma = \sqrt{\langle E_{reconstructed} - E_{generated} \rangle^2}$ , was originally quoted to be  $5.5\%/\sqrt{E} + 1.5\%$  (see the COMPASS proposal [1]). Results using this event generator showed that with the actual reconstruction code similar resolution can be obtained, as shown in figure 4.19.

For the spatial resolution in the ECAL2, also very good results were obtained with the reconstruction code. Spatial resolutions of the order of 1 mm were found for both  $x$  and  $y$  coordinates, as shown in figure 4.20. These results agree with the expected ones quoted in the COMPASS proposal (reference [1]).

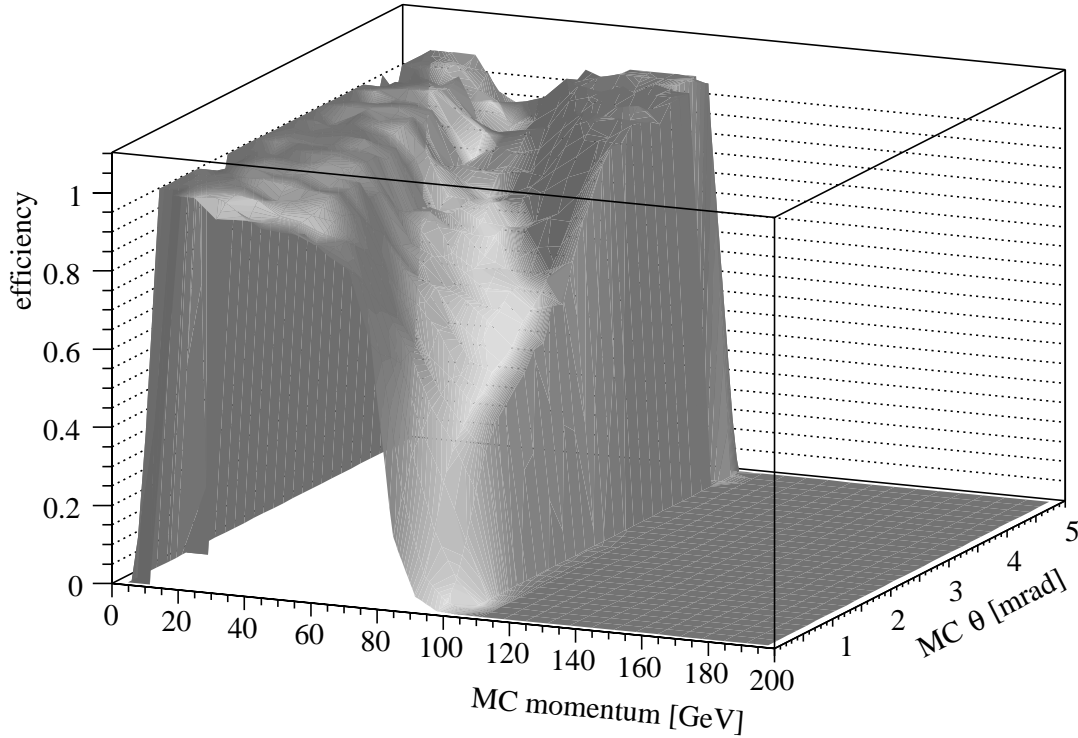


Figure 4.18: Reconstruction efficiency for the pions for different pion momenta and theta angles [70]. The efficiency is computed as the number of reconstructed pion tracks divided by the number of generated pion tracks. A hole in the acceptance of the detector is visible for small  $\theta$  angles and large longitudinal momenta and for large  $\theta$  angles and small longitudinal momenta.

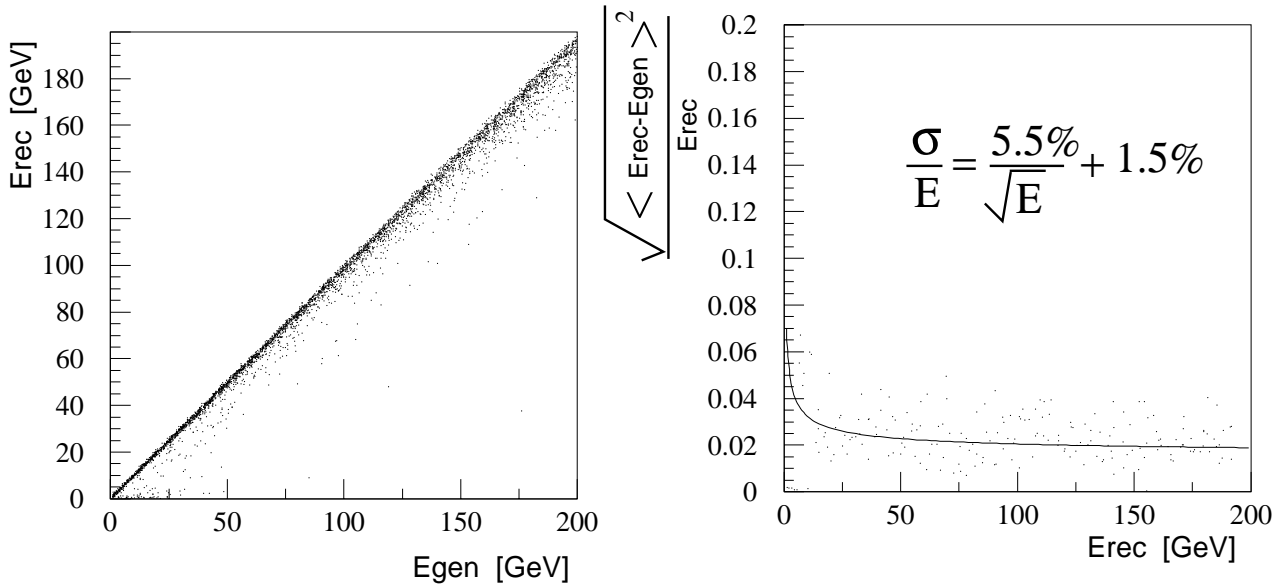


Figure 4.19: The left plot shows the energy of the reconstructed gamma versus the energy of the generated gamma. The right plot shows sigma versus the reconstructed energy. The curve running through the points indicates the predicted behaviour.

#### 4.4.2 Complete simulation

The chain of the reconstruction consisted of the event generation using the POLARIS event generator (as described in the chapter 4.2). COMGEANT was used to simulate the

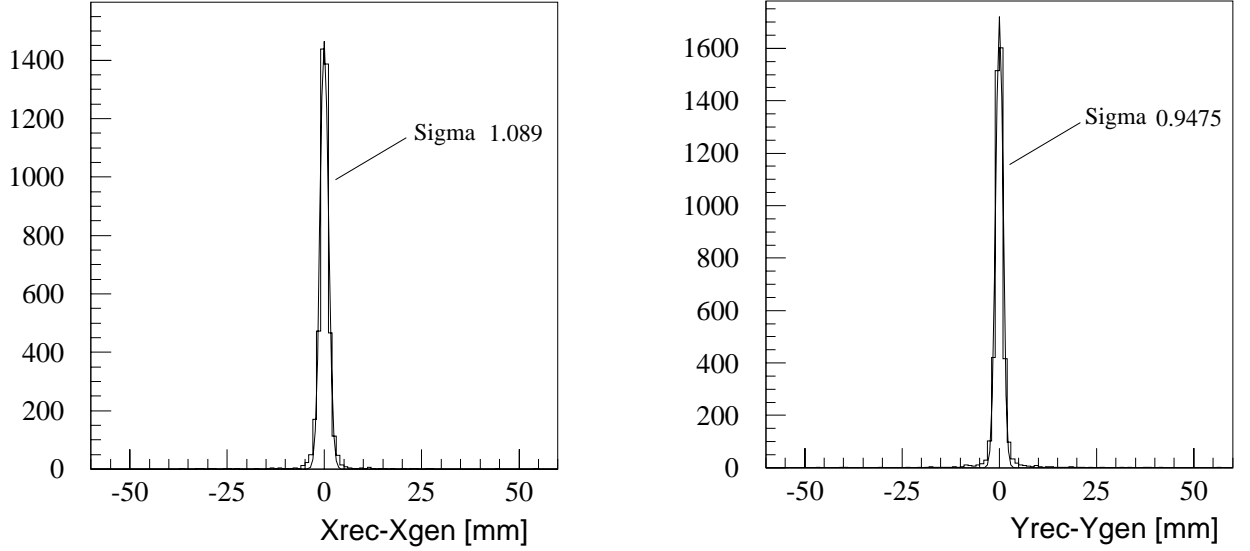


Figure 4.20: Simulated spatial resolution of ECAL2 for  $x$  and  $y$  coordinates.  $x_{gen}, y_{gen}$  and  $x_{rec}, y_{rec}$  refer to the generated (*gen*) and reconstructed (*rec*)  $x, y$  coordinates.

detector response when passing the generated particles through the COMPASS detector. The output of COMGEANT was used as input for the reconstruction program CORAL. The output of CORAL was analysed by a program developed to select the interesting events and to obtain the physics results. Not all events generated in POLARIS were used. Only those events that permitted the comparison with the results from the Serpukhov experiment were considered. The characteristics of the events selected were defined by a high energetic gamma with energy between 90 GeV and 190 GeV. This corresponds to the events where the scattered pion has an energy between 100 and 0 GeV.

#### 4.4.3 Selection of events

Primakoff reaction is defined in the following way:  $\pi^- Z \rightarrow \pi^- \gamma Z$ . A first requirement to accept an event is that the sum of the energy of the scattered pion and the energy of the produced gamma should be, within a certain resolution, equal to the beam energy (as shown in figure 4.21). For the simulations, a beam energy of 190 GeV was chosen.

A one percent resolution of the total energy (see figure 4.21) was found by the reconstruction of the  $\gamma$  energy and direction in the ECAL2 and the momentum reconstruction of the pion. For the Serpukhov experiment [59], the same plot was produced (figure 4.22). In the Serpukhov experiment, the energy of the beam was 40 GeV. Also in this case, the width of the energy distribution was consistent with the apparatus resolution.

To distinguish radiative scattering in the Coulomb field from scattering due to the strong interaction, a good resolution on the transverse momentum transfer is necessary. In order to be efficient in the separation, the resolution should be kept at the level of 10 to 20 MeV. The transverse momentum transfer can be expressed as follows:

$$q_T = \sqrt{(p_{x_{\pi^-}} + p_{x_{\gamma}})^2 + (p_{y_{\pi^-}} + p_{y_{\gamma}})^2} \quad (4.34)$$

For every component of the transverse momentum transfer, a value for the resolution of the order of 13 MeV was obtained, as can be seen in figures 4.23 and 4.24.

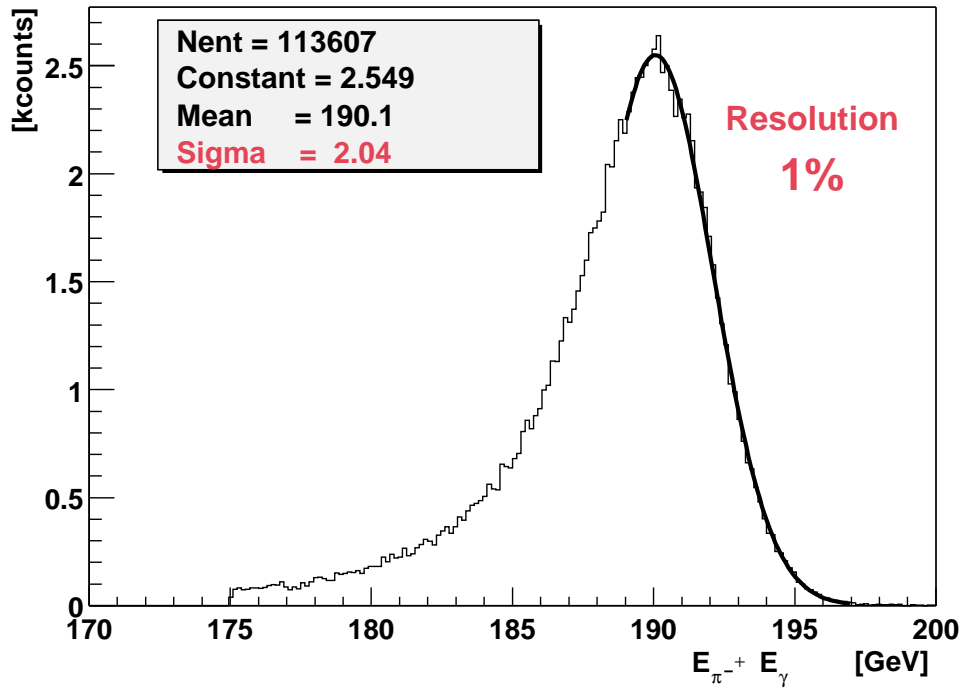


Figure 4.21: Sum of the energies of  $\pi^-$  and  $\gamma$ , corresponding to the energy of the intermediate state (Monte Carlo simulation, including reconstruction, in COMPASS) [70].

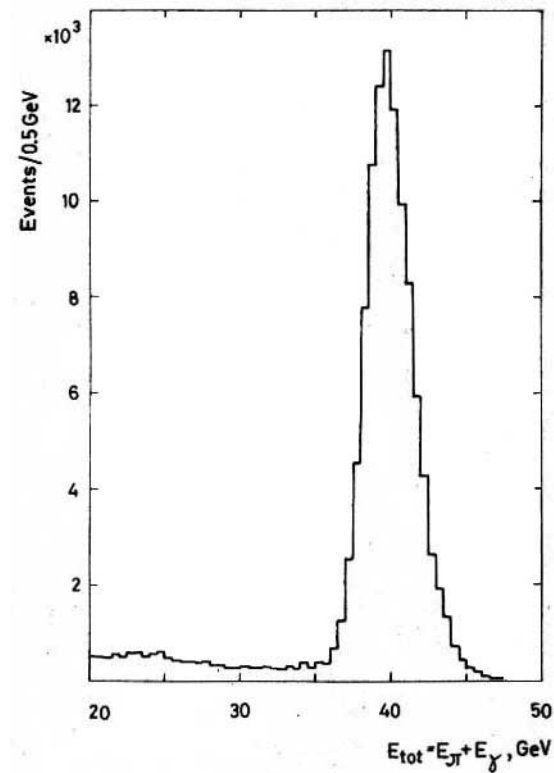


Figure 4.22:  $E_{tot}$  the sum of the energies of  $\pi^-$  and  $\gamma$ , corresponding to the energy of the intermediate state (Serpukhov data).

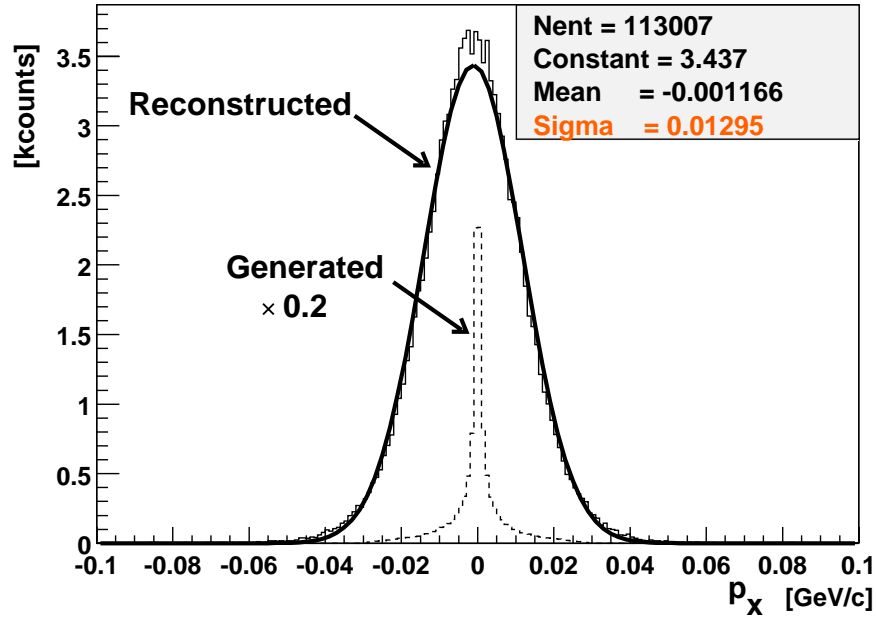


Figure 4.23:  $x$  component of the transverse transfer momentum. It is the sum of the  $x$  components of the momenta of the scattered  $\pi^-$  and  $\gamma$  [70].

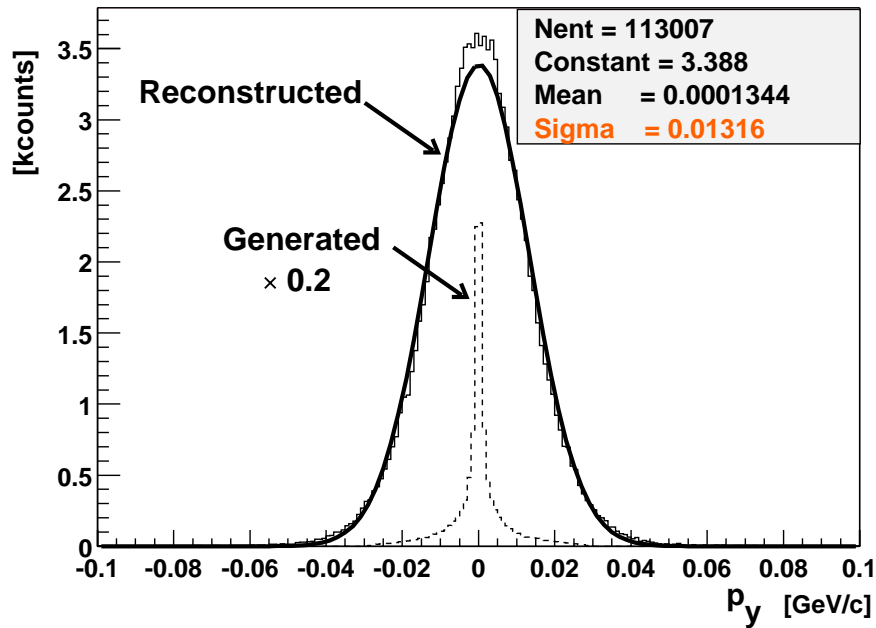


Figure 4.24:  $y$  component of the transverse transfer momentum. It is the sum of the  $y$  component of the momenta of the scattered  $\pi^-$  and  $\gamma$  [70].

The momentum of the  $\pi^-$  and the  $\gamma$  contribute to the measurement of the  $q_T$ . To obtain a good resolution in  $q_T$ , a good momentum reconstruction of the  $\pi^-$  and a good energy and spatial resolution of the  $\gamma$  are needed.

For the reconstruction of the angle of the pion, silicon stations will be used. Two silicon stations are situated in front of the target and two more stations are located after the target to measure the angle of the scattered pion with respect to the beam angle. The pitch of the silicon detectors is  $50 \mu\text{m}$ , giving a resolution for each detector

of 14  $\mu\text{m}$ . The distance between two silicon detectors is 45 cm, leading to an angular resolution of 0.043 mrad. This resolution contributes with approximately 3 MeV to the resolution of the transverse momentum measurement of the pion. For the gamma, the spatial resolution is 1 mm (see figure 4.20). This will provide an angular resolution of about 0.031 mrad, contributing with 3 MeV to the measurement of the resolution of the transverse momentum of the gamma. Based on the resolution on the momentum measurement of the pion, the resolution in the energy measurement of the gamma, and the multiple scattering due to the material in the COMPASS detector, the resolution of every component of  $q_T$  is found as shown in figures 4.23 and 4.24.

The four momentum transfer squared  $t$  can be expressed as:

$$t = (\mathbf{p}_{\text{beam}} - \mathbf{p}_{\pi^*})^2 \quad (4.35)$$

where  $\mathbf{p}_{\text{beam}}$  is the four momentum of the beam and  $\mathbf{p}_{\pi^*}$  is the four momentum of the intermediate system ( $\pi^- + \gamma$ ).

To separate between Primakoff events and the events from strong interaction, a cut in  $t$  is applied (see figure 4.26 for the  $t$  distribution). In the Serpukhov experiment (see figure 4.25) which applied a cut at 0.001  $\text{GeV}^2$ , there is a clear separation between the peak of the radiative Coulomb interaction, dominating at very small  $t$ , from the background corresponding to strong interactions. The background becomes dominant beyond some minimum value of  $t$ , weakly depending on the projectile. The same cut in  $t$  could be applied in COMPASS.

Introducing a cut on the transverse momentum transfer  $q_T$  for the selection of the events, is like cutting on  $\sqrt{t}$ . The longitudinal momentum transfer to the target should be small enough not to excite the first resonance of the hadron. The formula 4.36 [57] shows the expression for the longitudinal momentum transfer  $q_{\text{parallel}}$  in the projectile reference frame,

$$q_{\parallel} = \frac{M_{\pi^*}^2 - m_{\pi^-}^2}{2 \cdot m_{\pi^-}} \quad (4.36)$$

where  $M_{\pi^*}$  is the mass of the intermediate system and  $m_{\pi^-}$  is the mass of the  $\pi^-$ . The first resonance of the  $\pi^-$  has a mass of 1.3  $\text{GeV}/c^2$ . Thus the longitudinal momentum transfer to the target should be:

$$q_{\parallel} \ll \frac{M_{\pi(1300)}^2 - m_{\pi^-}^2}{2 \cdot m_{\pi^-}} \quad (4.37)$$

The dependence of the Primakoff cross-section on  $Z^2$  was measured in the Serpukhov experiment by using different target materials. This same study will be performed in COMPASS.

#### 4.4.4 Efficiency measurements

The efficiency is studied for the selected events with small  $t$  and where the sum of the energy of the  $\pi^-$  and the  $\gamma$  is, within some resolution, equal to the energy of the beam.

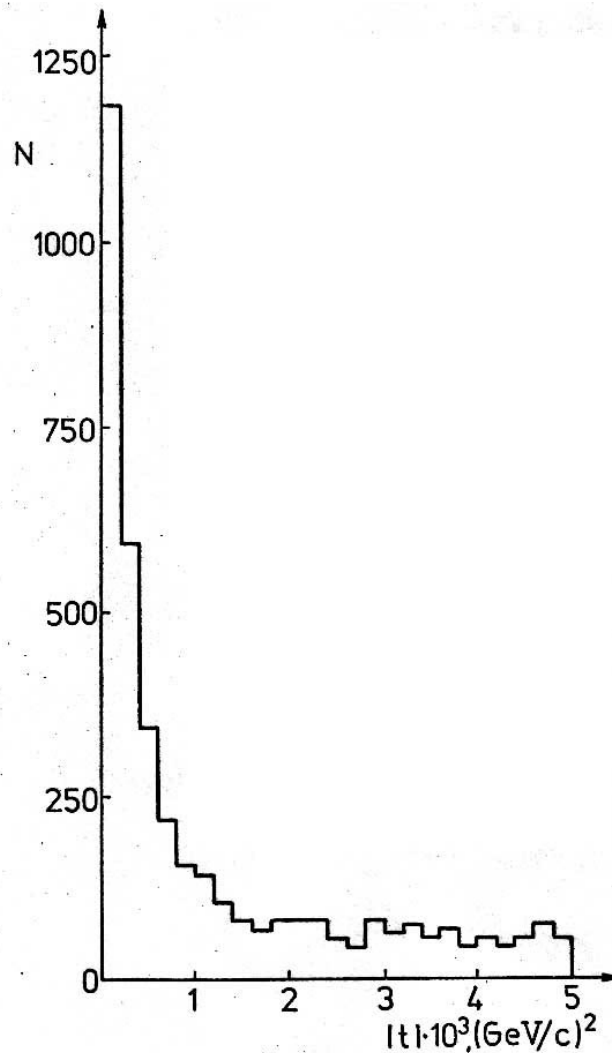


Figure 4.25:  $t$  distribution measured in the Serpukhov experiment. When making a cut at  $0.001 \text{ GeV}^2$  the peak for the Primakoff reaction can be easily separated from the background corresponding to the strong interaction.

The efficiency can be plotted as a function of three different interesting kinematic variables, including the momentum of the scattered pion, the energy of the gamma and the four momentum transfer squared  $t$ . The distribution of the gamma energy is shown in figure 4.28.

As the distribution of the pion momentum is complementary, the sum of the energy of the gamma and the energy of the scattered pion should be the energy of the beam. The efficiency versus the gamma energy is shown in figure 4.29.

The combined efficiency for higher gamma energies has large error bars because of low statistics. The detectors in the acceptance of the high energy pions are the small area trackers. As seen before, an acceptance hole is visible in the detector for high energy pions. This will reduce the detection efficiency for events with high momentum pions, where the associated  $\gamma$ 's have low energy.

Figure 4.30 shows the efficiency versus the four momentum transfer squared  $t$ . The uniformity in the efficiency implies that the distribution is not biased by the acceptance

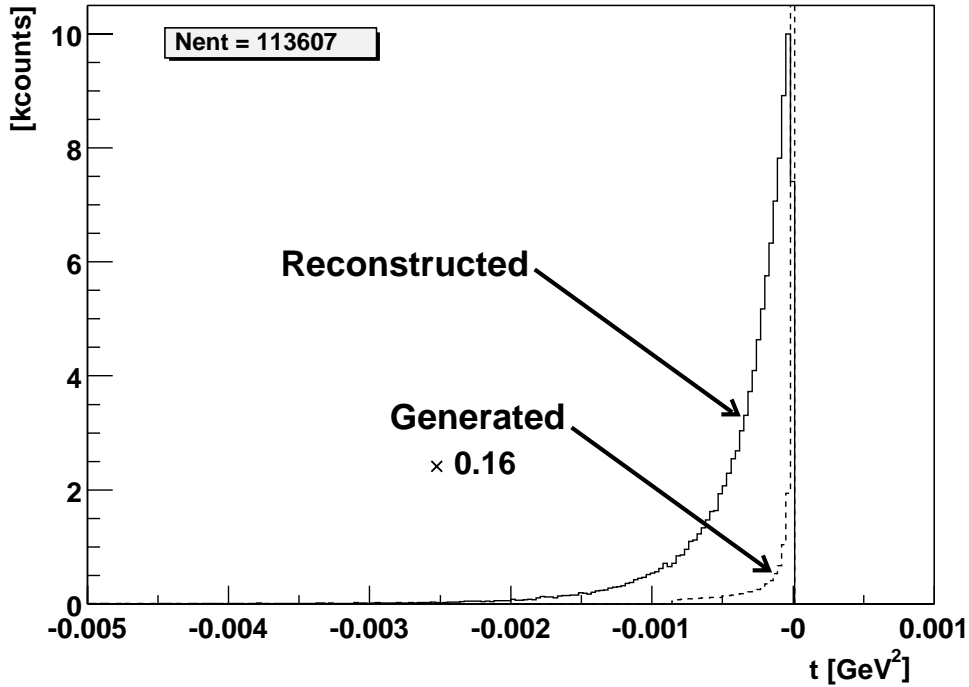


Figure 4.26:  $t$  distribution of generated events and of the reconstructed events in the COMPASS detector [70].

of the detector. Regardless of the cut in  $t$ , the efficiency is not affected.

#### 4.4.5 Trigger

Test beam studies for the trigger were performed in September 2000 [56]. The setup for the test beam was the following (see figure 4.31): a beam counter upstream of the target (S); a beam veto counter (beam killer) in front of ECAL2, covering the hole for the deflected primary beam (B); a hodoscope  $80\text{cm} \times 96\text{cm}$ , situated in front of ECAL2 (H), displaced horizontally by 20cm from the position of the deflected beam; a veto system around the target and the electromagnetic calorimeter (ECAL2).

According to the signature of the reaction, a beam particle is expected in S. Particles scattered by the target, should give a signal in H. No signal should be registered in the beam killer B but a highly energetic photon should be detected in ECAL2. The test beam demonstrated that an acceptable rate for the trigger can be achieved. The requirements to achieve this rate are the following: the coincidence between the energy deposition in the ECAL2 above a threshold of  $0.2$  to  $0.3 \times E_{beam}$  and the existence of a charged particle in the corresponding acceptance of H. The use of the beam killer B and of the veto counter does not improve much the rate reduction. The target veto could be used offline to reject background reactions with large momentum transfer to the target.

Some interesting numbers that are quoted include the following: from a beam intensity of  $6 \cdot 10^6/\text{spill}$  with a 3mm lead target, the trigger rate was found to be 250000/spill. The trigger gives a reduction factor of 24. The idea of the trigger is not to reduce too strongly the number of events since this will be done offline when analysing the events. The size of the hodoscope needed to cover the acceptance of the simulated scattered pions was calculated by plotting the simulated hit distribution of the scattered pions at the position

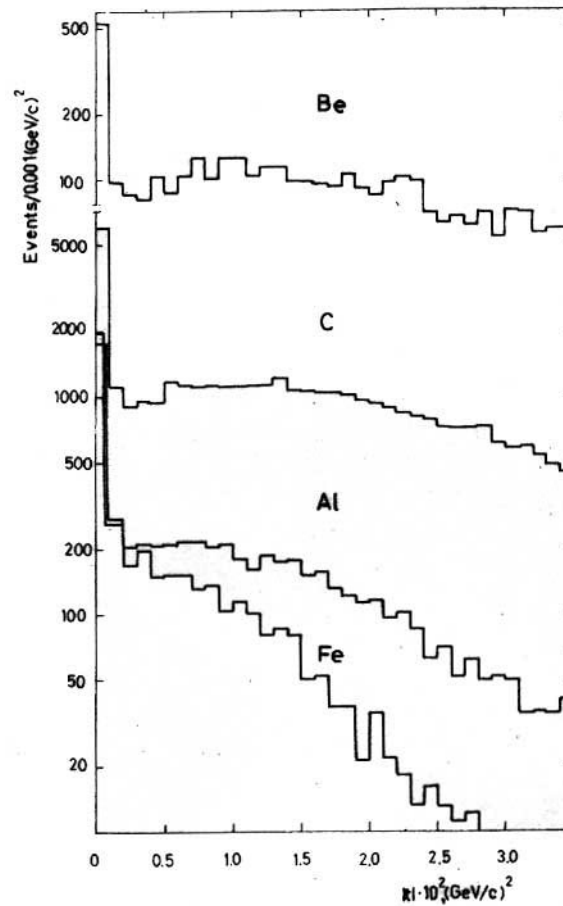


Figure 4.27: Measured  $t$  distribution of the reconstructed events for different targets, Be, C, Al and Fe (Serpukhov data). It is clearly shown that when making a cut the peak for the Primakoff reaction can be easily separated from the background corresponding to the strong interaction.

where the hodoscope will be situated. Figure 4.32 shows that the size needed for the hodoscope is 1m in horizontal direction and 40cm in vertical direction.

#### 4.4.6 Estimated statistics

In the Serpukhov experiment, the experimental results were retrieved using a lead target of a thickness of 0.25 radiation lengths. The integrated beam intensity was  $2 \cdot 10^{11}$  pions.

The planned beam intensity in COMPASS is  $10^7$  pions/spill. A value of 60% was chosen for the combined efficiencies of the accelerator and of the experiment. The running period considered is 30 days of operation. The target planned will correspond to a thickness of 0.5 radiation lengths. Considering all these factors, ten times more statistics than produced by the Serpukhov experiment can be achieved in 30 days of operation. This period of 30 days does not include the time needed to calibrate the ECAL2, to have the tracking detectors operational, and to run the DAQ in a stable mode.

Taking advantage of the different beam particles available, the electromagnetic polarizability of proton and kaon can be measured. Since the cross-section depends inversely on the square of the mass of the hadron considered, the measurement of the electromagnetic polarizability of baryons requires more beam time to accumulate high statistics samples

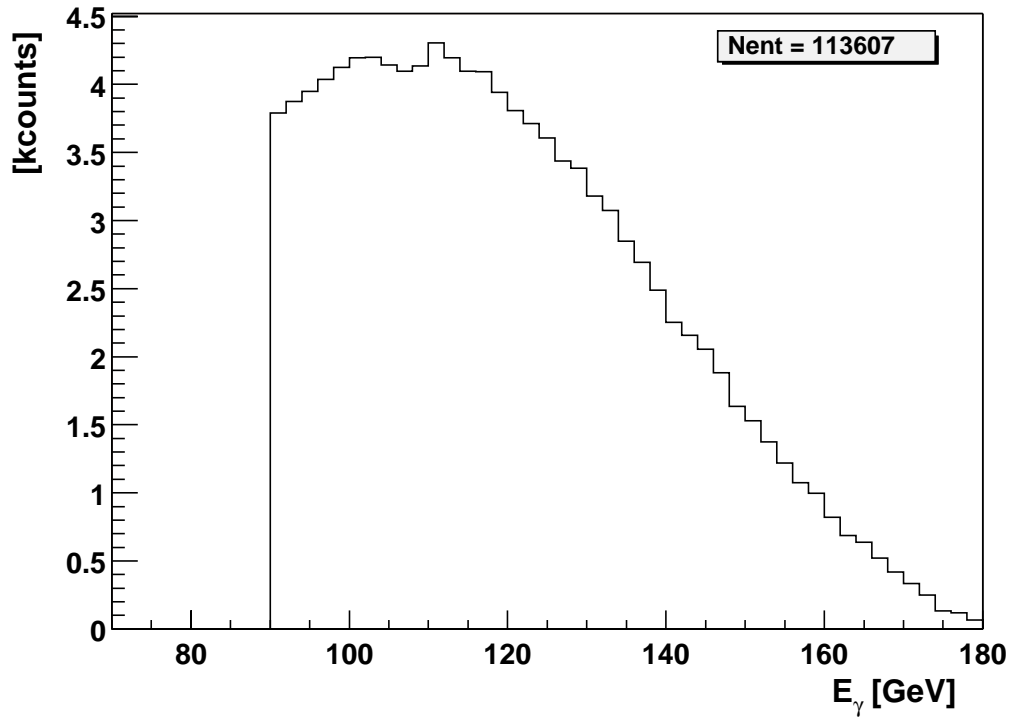


Figure 4.28: Gamma energy distribution [70].

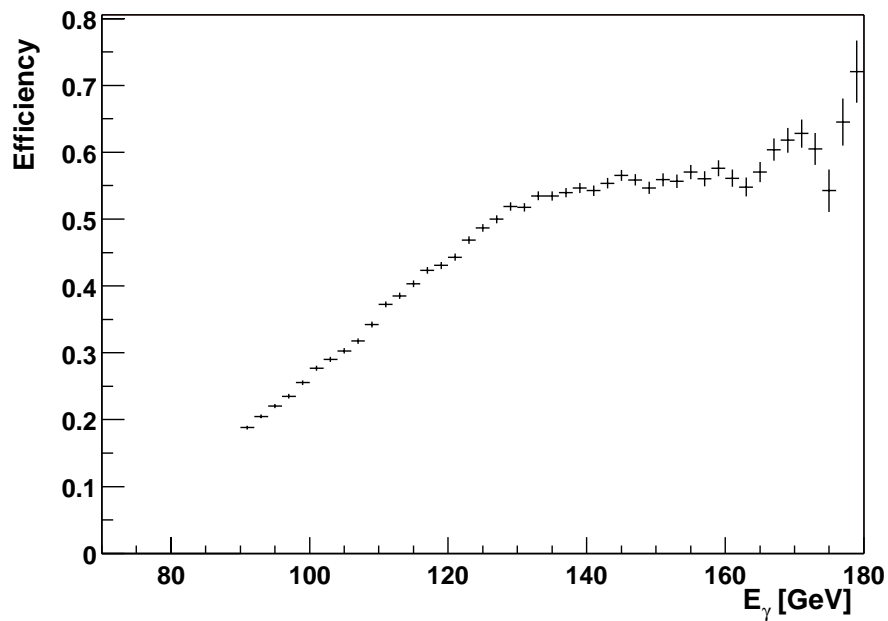


Figure 4.29: Efficiency versus pion momentum [70].

than in the case of mesons.

#### 4.4.7 Possible results in COMPASS

Since ten times more statistics than in the Serpukhov experiment can be accumulated in COMPASS, the electromagnetic polarizability of the  $\pi^-$  can be measured with 3 times

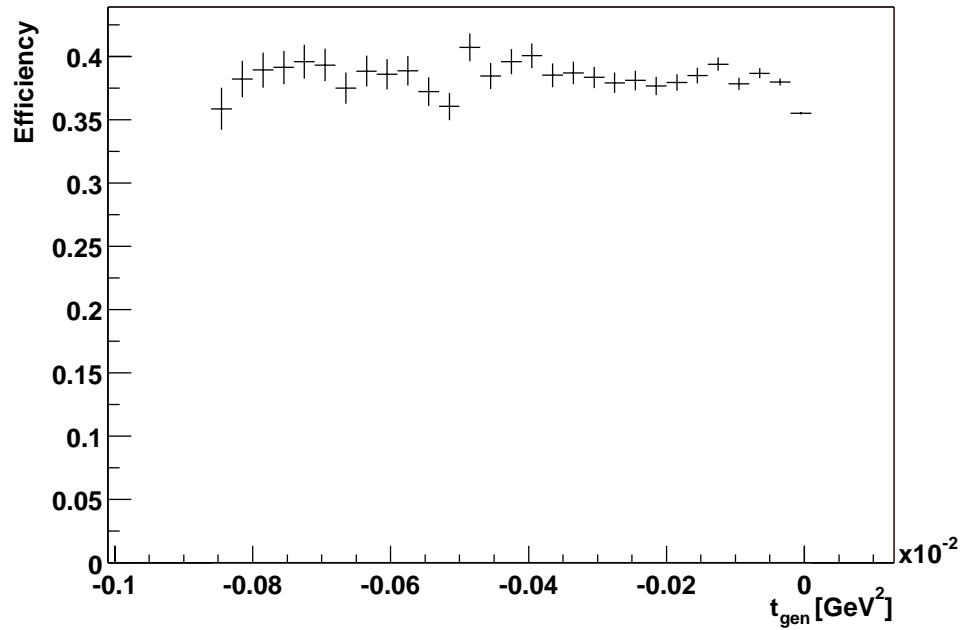


Figure 4.30: Efficiency versus the four momentum transfer squared  $t$  [70].

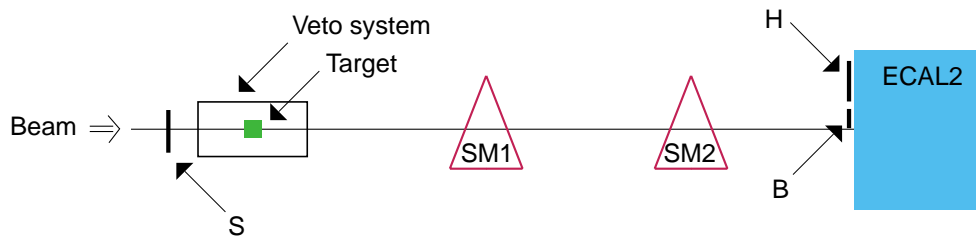


Figure 4.31: Trigger setup for the Primakoff measurement in COMPASS. It consists of a beam counter ( $S$ ), beam veto counter ( $B$ ), a hodoscope ( $H$ ), a veto system around the target and the electromagnetic calorimeter ( $ECAL2$ ).

higher precision.

Another advantage in COMPASS compared to Serpukhov is the constant efficiency for the measurement of highly energetic gammas. In the Serpukhov measurement, the efficiency decreased with the energy of the gammas (see figure 4.33).

Considering that a muon run could be performed during the COMPASS data taking period, the Primakoff cross-section for the pion can be compared to that of a point-like particle, the muon.

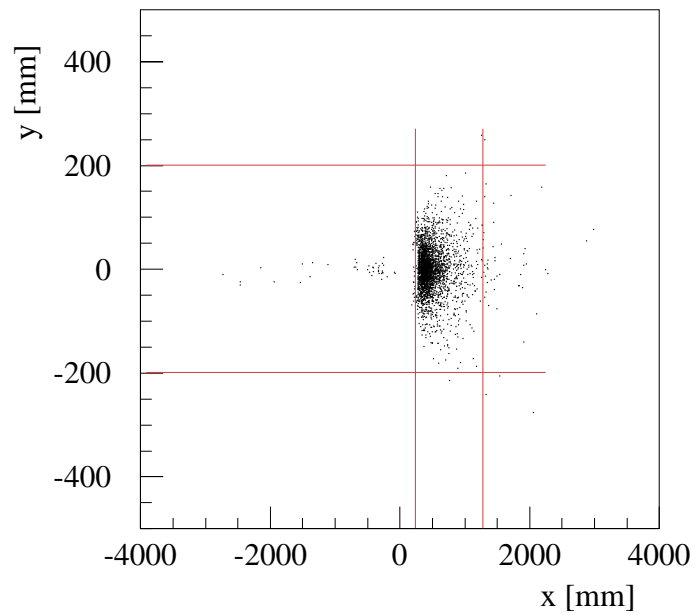


Figure 4.32: Simulated hit distribution of the scattered pion at 30 m from the target. The lines indicate the possible size of the trigger hodoscope.

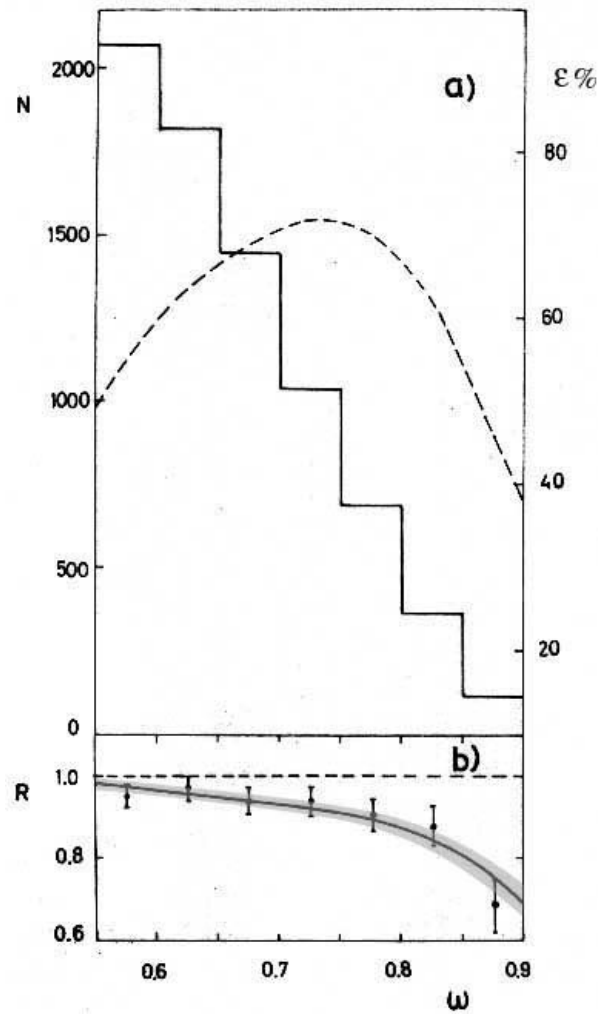


Figure 4.33: a) Distribution of the Primakoff events over the variable  $\omega = E_\gamma/E_{tot}$ . The discontinuous line is the detection efficiency; b) The  $\omega$  dependence of  $R = (d\sigma/d\omega)^{exp}/(d\sigma/d\omega)_{\alpha_\pi=0}^{theor}$ . The solid curve illustrates the results of the fit of the experimental data to the theoretical distribution with a polarizability  $\alpha_\pi = 6.1 \cdot 10^{-43} \text{ cm}^3$ . The grey shadowed region represents the width of the errors that can be obtained with the COMPASS measurement.

# Appendix A

## List of acronyms

CATCH: **C**ompass data **A**ccumulation, **T**ansfer and **C**ontrol **H**ardware  
CERN: European Organization for Nuclear Research in Geneva  
COMGEANT: **C**OMpass **G**EANT  
COMPASS: **C**OMmon **M**uon and **P**roton **A**pparatus for **S**tructure and **S**pectroscopy  
CORAL: **C**OMpass **R**econstruction and **A**nalysis program  
DAQ: **D**ata **A**cquisition  
DESY: **D**eutsches **E**lektronen-**S**ynchrotron  
ECAL: **E**lectromagnetic **C**alorimeter  
FE: **F**ront **E**nd  
GEM: **G**as **E**lectron **M**ultiplier  
HCAL: **H**adronic **C**alorimeter  
HERA: **H**adron-**E**lectron **R**ing **A**ccelerator  
HERMES: **H**ERa **M**Easurement of **S**pin  
HQET: **H**heavy **Q**uark **E**ffective **T**heory  
HV: **H**igh **V**oltage  
JINR: **J**oint **I**nstitute for **N**uclear **R**esearch  
LAS: **L**arge **A**ngle **S**pectrometer  
LEAR: **L**ow **E**nergy **A**ntiproton **R**ing  
LHC: **L**arge **H**adron **C**ollider  
MWPC: **M**ulti **W**ire **P**roportional **C**hamber  
R&D: **R**esearch and **D**evelopment  
RICH: **R**ing **I**maging **C**herenkov detector  
RHIC: **R**elativistic **H**eavy **I**on **C**ollider  
SLAC: **S**tanford **L**inear **A**ccelerator **C**alifornia  
SM: **S**pectrometer **M**agnet  
SPS: **S**uper **P**roton **S**ynchrotron  
TDC: **T**ime to **D**igital **C**onverter  
TS2: **T**racking **S**tation **2**

# Appendix B

## Kinematics for inelastic diffraction at high energies

The mass  $M_x$  of the object X can be expressed as:

$$1 - x_f = \frac{M_x^2 - m_{\pi^-}^2}{s} \quad (\text{B.1})$$

This equation can be derived from the definition of the variable  $x_f$ , "Feynman-x":

$$x_f = \left( \frac{p_z}{p_{max}} \right)_{cm} \quad (\text{B.2})$$

In the following, the process of deriving the equation B.1 from the equation B.2 will be explained. In the center of mass system of  $\pi^-$  and p,  $x_f$  can be expressed as:

$$x_f = \frac{\sqrt{[s - (M_X + m_p)^2] \cdot [s - (M_X - m_p)^2]}}{\sqrt{[s - (m_{\pi^-} + m_p)^2] \cdot [s - (m_{\pi^-} - m_p)^2]}} \quad (\text{B.3})$$

where  $s$  is the square of the center of mass energy of the  $\pi^-$  p system and  $m_{\pi^-}$ ,  $m_p$  are the masses of the  $\pi^-$  and p respectively.  $s$  can be calculated as:

$$s = m_{\pi^-}^2 + m_p^2 + 2 \cdot E_{\pi^-} \cdot m_p \quad (\text{B.4})$$

$x_f$  can be rewritten as:

$$x_f = \sqrt{\frac{\left(1 - \frac{(M_X + m_p)^2}{s}\right) \cdot \left(1 - \frac{(M_X - m_p)^2}{s}\right)}{\left(1 - \frac{(m_{\pi^-} + m_p)^2}{s}\right) \cdot \left(1 - \frac{(m_{\pi^-} - m_p)^2}{s}\right)}} \quad (\text{B.5})$$

When the fractions  $\frac{(M_X + m_p)^2}{s}$  and  $\frac{(m_{\pi^-} + m_p)^2}{s}$  are small, their product can be neglected and  $x_f$  can be approximated by:

$$x_f \sim \sqrt{\frac{1 - \frac{(M_X + m_p)^2}{s} - \frac{(M_X - m_p)^2}{s}}{1 - \frac{(m_{\pi^-} + m_p)^2}{s} - \frac{(m_{\pi^-} - m_p)^2}{s}}} \quad (\text{B.6})$$

With the same approximations the equation for  $x_f$  can be written as:

$$x_f \sim \sqrt{1 - \frac{(M_X + m_p)^2}{s} - \frac{(M_X - m_p)^2}{s} + \frac{(m_{\pi^-} + m_p)^2}{s} + \frac{(m_{\pi^-} - m_p)^2}{s}} \quad (\text{B.7})$$

When  $x$  is a small number,  $\sqrt{(1 \pm x)}$  can be expanded as:  $\sqrt{(1 \pm x)} = 1 \pm \frac{1}{2} \cdot x \mp \frac{1}{8} \cdot x^2 \pm \dots$ . Applying this to the equation for  $x_f$ , the following equation can be obtained:

$$x_f \sim 1 + \frac{1}{(2 \cdot s)} \cdot (-2 \cdot M_X^2 - 2 \cdot m_p^2 + 2 \cdot m_{\pi^-}^2 + 2 \cdot m_p^2) \quad (\text{B.8})$$

Arranging this equation we come to the final approximated equation for the mass of the object X:

$$1 - x_f \sim \frac{M_x^2 - m_{\pi^-}^2}{s} \quad (\text{B.9})$$

Nevertheless the exact expression for the mass of the object X is the equation B.3.

# Bibliography

- [1] COMPASS, A proposal for a COmmon Muon and Proton Apparatus for Structure and Spectroscopy.  
CERN/SPSLC 96-14, SPSLC/P297, **1996**.
- [2] Addendum 1 to the COMPASS proposal.  
CERN/SPSLC 96-30, SPSLC/P297 Add.1, **1996**.
- [3] F.Bradamante: The gluon contribution to the nucleon spin and the COMPASS experiment at CERN,  
Prog.Part.Nucl.Phys. 44 **1999** 339-359.
- [4] The European Muon Collaboration, J.Ashman et al.: An investigation of the spin structure of the proton in deep inelastic scattering of polarized muons on polarized protons.  
Nucl. Phys. B 328 (**1989**) 1.
- [5] U.Wiedner: The COMPASS experiment at CERN,  
7th International Symposium on Meson-nucleon Physics and the structure of the Nucleon-MENU'97 Vancouver, Canada, **1997**  
Edited by G.Smith. Published by piN Newsl. 13, TRI-97-1 (195-200) **1997**.
- [6] The Crystal Barrel collaboration, C.Amsler et al.: High statistics study of  $f_0(1500)$  decay into  $\pi^0 \pi^0$  .  
Phys. Lett. B 342 (**1989**) 433-439.
- [7] A.Bravar, D.von Harrach and A.Kotzinian: Large gluon polarization from correlated high- $p_T$  hadron pairs in polarized electro-production.  
Phys.Lett. B 421 (**1998**) 349-359.
- [8] D.Thers et al.: Micromegas as a large microstrip detector for the COMPASS experiment,  
Saclay internal note: DAPNIA-SPHN-2000-37 (EXT-2000-183), **2000**.  
Preprint submitted to Elsevier Preprint, 15th of June, **2000**.
- [9] J.Ellis, D.Kharzeev, A.Kotzinian: The proton spin puzzle and  $\Lambda$  polarization in deep-inelastic scattering,  
Z. Phys. C69 (**1996**) 467.
- [10] J.Ellis, et al.: Abundant  $\phi$ -meson production in  $\bar{p}p$  annihilation at rest and strangeness in the nucleon.  
Phys. Lett. B 353 (**1995**) 319-328.

- [11] V.Alexakhin: Investigation of the straw chambers inclination angle. COMPASS internal note 1999-10, **1999**.
- [12] A.Romaniouk: Choice of materials for the construction of the TRT. ATLAS internal note, ATL-INDET-98-211, 13 October **1998**.
- [13] J.Marzec et al.: Straw tubes electrical properties. COMPASS internal note 1998-10, **1998**.
- [14] J.Marzec et al.: Straw tubes electrical properties-part II. COMPASS internal note 1999-1, **1999**.
- [15] R.Veenhof: Simulation of gaseous detectors.  
<http://consult.cern.ch/writeup/garfield/>
- [16] J.Adler et al.: The MARK III vertex chamber. NIM A 276 (**1989**) 42-52.
- [17] W.W.Ash et al.: Design, construction, prototype tests and performance of a vertex chamber for the MAC detector. NIM A 261 (**1987**) 399-419.
- [18] L.Benussi et al.: Performance of long straw tubes using dimethyl ether. NIM A 361 (**1995**) 180-191.
- [19] L.Benussi et al.: The FINUDA straw tubes detector. NIM A 379 (**1996**) 429-431.
- [20] C.Avanzani et al.: High precision limited streamer drift tubes. NIM A 367 (**1995**) 154-158.
- [21] S.H.Oh, A.T. Goshaw and W.J. Robertson: Construction and performance of a 2.7 m long straw drift tube prototype chamber for the SSC. NIM A 309 (**1991**) 368-376.
- [22] Y.Arai et al.: A modular straw drift tube tracking system for the Solenoid Detector Collaboration experiment. Part I. Design. NIM A 381 (**1996**) 355-371.
- [23] Y.Arai et al.: A modular straw drift tube tracking system for the Solenoid Detector Collaboration experiment. Part II. Performance. NIM A 381 (**1996**) 372-384.
- [24] H.Ogren: The straw tracker for the SDC detector. NIM A 367 (**1995**) 133-137.
- [25] N.H.Hamann et al.: The JETSET barrel drift-tube ("straw") chamber. NIM A 346 (**1994**) 57-74.
- [26] G.Bonvicini et al.: Construction and testing of a precision 2  $\mu$ m long straw chamber prototype. NIM A 359 (**1995**) 492-499.

- [27] J.M.Dyring: Detailed studies of the reaction  $p p \rightarrow p p \eta$  using a straw chamber tracking device.  
PhD Thesis; Uppsala University **1997**.
- [28] W.J.Broeder et al.: Readout and trigger electronics for the TPC vertex chamber.  
IEEE Transactions on Nuclear Science, Vol.35 (February **1988**) 329-333.
- [29] V.M.Aulchenko et al.: Vertex chamber for the KEDR detector.  
NIM A 283 (**1989**) 528-531.
- [30] R.Cizeron et al.: Results from Beam Tests of a 2.4  $\mu\text{m}$  Straw Chamber.  
Internal note of the Laboratoire de l'accélérateur linéaire, Orsay, LAL 91-07, **1991**.
- [31] P.Baringer et al.: A drift chamber constructed of aluminized mylar tubes.  
NIM A 254 (**1987**) 542-548.
- [32] C.Biino et al.: Charge division in a small proportional chamber constructed with aluminized mylar tubes.  
NIM A 271 (**1988**) 417-422.
- [33] M.Frautschi et al.: The AMY inner tracking chamber.  
NIM A 307 (**1991**) 52-62.
- [34] ATLAS inner detector technical design report. Volume 2.  
ATLAS TDR 5, CERN/LHCC 91-17, 30 April **1997**.
- [35] S.Bhadra et al.: The design and construction of the CDF central drift tube array.  
NIM A 268 (**1988**) 92-104.
- [36] A.F.Sustavov et al.: Thin-wall drift tube vertex chamber for the AMPIR spectrometer.  
NIM A 367 (**1995**) 159-162.
- [37] H.Pi: An event generator for interactions between hadrons and nuclei-FRITIOF version 7.  
<http://consult.cern.ch/writeup/fritiof/>
- [38] The European Physical Journal C.  
Review of Particle Physics, Volume 3, Number 1-4, **1998**.
- [39] M.Deile, J.Dubbert, N.P.Hessey: Charge division and intrinsic Pulse Shaping in Drift Tubes.  
ATLAS Internal Note, MUON-NO-105, 1 February **1996**.
- [40] G.Braun et al.: In Vivo Time Resolution Tests of MAD-IV and ASD8b Preamplifiers.  
COMPASS Note, internal note 1999-16, **1999**.
- [41] M.Sans and U.Wiedner: Test beam results of 2 prototypes of straw tube chambers for COMPASS.  
COMPASS internal note 1999-2, **1999**.

- [42] P.A.Tipler: Física, Tipler tomo 1, segunda edición. Editorial Reverté , S.A, **1989**, Pages 479 and 498.
- [43] W.R.Leo: Techniques for nuclear and particle physics experiments. Springer Verlag, Berlin, 2nd edition, **1994**.
- [44] M.Faessler: Pomeron-nucleus interactions  
Zeitschrift für Physik C-Particles and Fields C58 (**1993**) 567-574.
- [45] K.H.Dederichs: Diffraction Dissociation of Nuclei in Collisions with 450 GeV/c Protons.  
PhD Thesis; Ludwig-Maximilians-Universität München, July **1989**.
- [46] M.Faessler: Bremsstrahlung and diffractive dissociation.  
CERN-EP/89-163 (15 December **1989**) and Physics letters B 232 (**1989**) 405-412.
- [47] L.Gatignon: Hadron beam.  
<http://sl.web.cern.ch/SL/eagroup/NewM2/main.html>
- [48] V.Alexakhine: The COMPASS GEANT.  
<http://valexakh.home.cern.ch/valexakh/wwwcomg/index.html>
- [49] A.Olchevski: Notes on the Experimental Requirements for COMPASS Initial Primakoff Physics Programme.  
(Private communication).
- [50] GEANT - Detector Description and Simulation Tool.  
<http://wwwinfo.cern.ch/asd/geant/index.html>
- [51] K.Platzer: Notes on the X-ray machine.  
(Private communication).
- [52] J.Besserer et al.: Testbeam Studies of Straw Drifttubes for the COMPASS Experiment.  
Annual report from the Accelerator lab of the LMU and TU Munich (**1998**) 88.
- [53] J.Besserer et al.: Irradiation response of Straw Drifttubes.  
Annual report from the Accelerator lab of the LMU and TU Munich (**1999**) 109.
- [54] F.Sauli: Principles of operation of multiwire proportional and drift chambers.  
CERN 77-09, Lectures given in the Academic Training Programme of CERN 1975-1976, 3 May **1977**.
- [55] K.Zaremba: Description of the mother board for the COMPASS straw tube drift chambers.  
(Private communication).
- [56] A.Sadovski: Test beam studies for a trigger for a Primakoff measurement in COMPASS.  
COMPASS collaboration meeting, October 2000, Dubna.

- [57] M.Buenerd.: Prospects for hadron electromagnetic polarizability measurement by radiative scattering on a nuclear target.  
NIM A 361 (**1995**) 111-128.
- [58] B.R.Holstein: Electromagnetic Polarizability of the Nucleon.  
Com.Nucl.Part.Phys. 20 (**1992**) 301.
- [59] Yu.M.Antipov et al.: Measurement of  $\pi^-$  -meson polarizability in pion compton effect.  
Phys.Lett. B 121 (**1983**) 445.
- [60] Yu.M.Antipov et al.: Experimental estimation of the sum of the pion electrical and magnetic polarizabilities.  
Z.Phys. C -Particles and Fields 26 (**1985**) 495-497.
- [61] G.Mallot: Accessing the gluon polarisation in deep inelastic muon scattering.  
Proceedings on the International School on Nuclear Physics: 17th course on Quarks in Hadrons and Nuclei, Erice 19-27 September **1995**.  
Edited by Faessler, Amand. Published by Oxford Pergamond **1996**.
- [62] C.Bovet et al.: The CEDAR counters for particle identification in the SPS secondary beams : a description and an operation manual.  
CERN 82-13 (**1982**) 37p.
- [63] H.Fischer et al.: CATCH-X Users Manual.  
COMPASS internal note 2000-12, **2000**.
- [64] M.Lamanna: The COMPASS Computing Farm Project.  
COMPASS internal note 2000-14, **2000**.
- [65] P.V.Landshoff and O.Nachtmann: Vacuum structure and diffraction scattering.  
Z.Phys.C- Particles and Fields 35 (**1987**) 405-416.
- [66] R.Risken: Description of the front end card.  
(Private communication).
- [67] U.Fuchs: Calibration studies for the COMPASS straws.  
(Private communication).
- [68] V.Pechekhonov et al., from JIRN, Dubna: Design of spacers and end-plugs.  
(Private communication).
- [69] K.Zaremba: distribution of electrons in a cluster.  
(Private communication).
- [70] This figure is the result of a collaboration with Maria Laura Colantoni (University of Torino, Italy) and Roland Kuhn (Technische Universität München, Germany).
- [71] V. Steiner, M. Moinester, M. Buenerd, POLARIS event generator.  
(Private communication).



## Acknowledgements

High energy physics experiments require the close collaboration of many people. Here I would like to take the opportunity to express my gratitude to those who provided me with support and help.

First I want to express my sincere thanks to Prof. Dr. Martin Faessler who gave me the opportunity to work in this kind of physics. He has been a patient supervisor and an excellent teacher.

I also would like to thank all the people from the Munich straw group working together on this challenging project. In the same content I acknowledge the help provided by the other groups in the straw project, like Freiburg University, Warsaw University of Technology, JIRN-Dubna and Moscow state University.

I received support from the offline and Monte Carlo groups allowing for the fast development of the simulation tools.

Finally I want to thank all the members of the COMPASS collaboration who supported me and took interest in my work.



25th February 2002

## Curriculum Vitae

### Personal information

*Name:* Marta Sans Merce  
*Birthday:* July 27, 1971  
*Place of birth:* Barcelona, Spain  
*Nationality:* Spanish  
*Civil state:* Single

### School

1977 - 1985 Elementary school at "Cours la Fontaine" in Barcelona.  
1985 - 1989 Secondary school at "San Ignacio" in Barcelona  
1989 Selectividad (final examination)

### Education

1989-1996 Degree in Physics at the University of Barcelona, Spain.  
July 1996-August 1996 Invited at CERN to participate in the mounting of the readout electronics for the RICH detector of the CAPRICE experiment at CERN.  
August 1996-April 1997 Participating in the ATHENA experiment at CERN in the frame work of my diploma thesis at the University of Barcelona. Thesis title:"Positron and antiproton motions in a nested Penning trap".  
May 1997-November 1997 Technical assistant at DESY-Zeuthen for the HERA-B experiment. I took part in the construction and tests of honeycomb chambers.  
December 1997 Final examination for the diploma thesis at the University of Barcelona.  
January 1998-today PhD student at the University of Munich. Thesis title:"Development of drift chambers and physics simulations for the COMPASS experiment".

**Languages** (beside Spanish and Catalan) in order of knowledge: English, French, learning German.